Title	Impacts of tides on large scale wind driven boundary currents in climate sensitive regions
Author(s)	Chou, Hung Wei
Degree Grantor	北海道大学
Degree Name	博士(環境科学)
Dissertation Number	甲第14635号
Issue Date	2021-09-24
DOI	https://doi.org/10.14943/doctoral.k14635
Doc URL	https://hdl.handle.net/2115/96835
Type	doctoral thesis
File Information	CHOU_Hung-Wei.pdf

Doctoral Dissertation

Impacts of tides on large scale wind driven boundary currents in climate sensitive regions

気候敏感海域における潮汐による

大規模風成境界流へのインパクト

Hung-Wei Shu (Hung-Wei Chou)

Graduate School of Environmental Science,
Hokkaido University

August 2021

This dissertation is adapted from:

Shu, HW., Mitsudera, H., Yamazaki, K., Nakamura, T., Kawasaki, T., Nakanowatari, T., Nishikawa, H., Sasaki, H., **Tidally modified western boundary current drives interbasin exchange between the Sea of Okhotsk and the North Pacific**. *Scientific Reports* 11, 12037 (2021). https://doi.org/10.1038/s41598-021-91412-y

Abstract

This research aims to investigate the tidal impacts on wind-driven boundary currents and their further modification to the large-scale circulation. After decades of silence, the tidal study is re-focused by oceanographers since the tidal mixing on the continental shelf is suggested to transfer the energy from wind and heat driving surface into the deep ocean. However, the impacts of tides on the wind-driven boundary current are still overlooked, although it bathed enormous tidal activities on their pathway. For instance, the Kuril Islands, an island chain located between the Sea of Okhotsk and the North Pacific, is one of the worldclass tidal activity hotspots and regulating the interbasin exchange between two basins, which governs the intermediate water ventilation and fertilization of the nutrient-rich subpolar Pacific. Previous study suggests that the East Kamchatka Current (EKC), a western boundary current (WBC) flowing along with the Kurils Islands, drives the interbasin exchange by its partial intrusion into the Sea of Okhotsk. However, the exchange mechanism is puzzling; the simulated interbasin exchange is unrealistically small in high-resolution models if only wind-driven western boundary current is considered. The WBC overshoots passing by deep straits and does not induce exchange flows. Therefore, partial intrusion cannot be solely explained by large-scale, wind-driven circulation.

Numerical simulations demonstrate that tidal forcing is the missing mechanism that drives the exchange by steering the WBC pathway. Upstream of the deep straits, tidally-generated topography trapped waves over a bank lead to cross-slope upwelling. This upwelling enhances bottom pressure, thereby steering the WBC pathway toward the deep straits. The upwelling is identified as the source of joint-effect-of-baroclinicity-and-relief (JEBAR) in the potential vorticity equation, which is caused by tidal oscillation instead of tidally-enhanced vertical mixing. The WBC then hits the island chain and induces exchange flows.

Most of ocean general circulation models obtain the tidal impacts through the

parameterization of tidally-enhanced vertical mixing. This study addresses that mixing is not a major contributor, but the topographic trapped waves. It suggests that accounting for tidal forcing in high-resolution models would facilitate the estimation of water dynamics not only between the Sea of Okhotsk and the North Pacific, but in other subpolar and polar regions where diurnal tides are dominant, such as Antarctic continental shelf. By comparison of model outputs and moorings, the tide oscillates the Antarctic Slope Current (ASC), the other wind-driven boundary current which flows along with the Antarctic continental shelf. The ASC is then strengthened and warmed by tidally-generated topographic trapped waves along with the slope. Comprehensively, in addition to the interbasin exchange problem in the North Pacific, this study implies that the inclusive of tidal forcing in high-resolution models is essential for capturing the accurate WBC's dynamics in climatically sensitive areas. The further investigation of local tidal dynamics is expected not only to be important to the regional study but also to global climate simulations.

Contents

Abstract **1**

Abbreviations **5**

1. General Introduction: Re-discover tidal dynamics in global ocean **7**

1.1 Absence of tidal forcing in large-scale ocean dynamics 8
1.2 Tide generated topography trapped waves on the continental edge 9
1.3 Climate sensitive area: Kuril Islands 11
1.4 Argument of this study 13

2. Models and Data Description **15**

2.1 Models 16
2.1.1 CCSR Ocean Component Model (COCO) 16
2.1.2 Ocean General Circulation Model For the Earth Simulator (OFES) 20
2.1.3 Massachusetts Institute of Technology General Circulation Model (MITgcm) 20
2.2 Data 22

3. Tidally modified western boundary current drives interbasin exchange between the Sea of Okhotsk and the North Pacific **29**

3.1 Introduction 30
3.2 Results 34
3.2.1 Overview of the tidal and non-tidal flow field 34
3.2.2 Transition experiment from non-tidal to tidal state 36
3.2.3 Tidal-period-mean PV budget of the EKC over the North Bank 38
3.2.4 Source of JEBAR change for the EKC's path shift 42
3.2.5 Tidally-modified EKC drives the interbasin exchange 44
3.3 Discussion: Influences of tidally enhanced vertical mixing on the interbasin exhange 46

4. Discussion: Possible tidal impacts on the Antarctic Slope Current **69**

4.1 Antarctic Slope Current modulates the heat intrusion towards the Totten Ice Shelf 70
4.2 Tide warms the mCDW upper boundary on the ASC..71
4.3 Tides oscillate the ASC...73
4.4 Hypothesis: Possible mechanism of tidally modulating cross-slope heat flux 76
5. General Conclusion 89

References 93

Acknowledgements 103

Appendix 1: Circular theorem 105
Appendix 2: Initial state for COCO model...107
Appendix 3: Seasonality 109
Appendix 4: Potential Vorticity Equation derivation 113
Supplementary Movie 1: Propagation of the tidal topography trapped wave. 115
Supplementary Movie 2: The transition experiment from non-tidal to tidal state......................117

Abbreviations

ASC:	Antarctic Slope Current
ASF:	Antarctic Slope Front
COCO:	CCSR Ocean Component Model
CDW:	Circumpolar Deep Water
EKC:	East Kamchatka Current
ECCO:	Estimating the Circulation and Climate of the Ocean
JODC:	Japan Oceanographic Data Center
JEBAR:	joint-effect-of-baroclinicity-and-relief
MITgcm:	Massachusetts Institute of Technology General Circulation Model
MIC:	Middle Island Chain
mCDW:	modified Circumpolar Deep Water
NPIW:	North Pacific Intermediate Water
OGCM:	ocean general circulation model
OFES:	Ocean General Circulation Model For the Earth Simulator
OMIP:	Ocean Model Intercomparison Project
PV:	potential vorticity
TIS:	Totten Ice Shelf
VACM:	Vector Averaging Current Meters
WBC:	western boundary current
WOA09:	World Ocean Atlas 2009

This page intentionally left blank

Chapter 1

General Introduction: Re-discover tidal dynamics in global ocean

1.1 Absence of tidal forcing in large-scale ocean dynamics

Tides, as being one of the earliest ocean motions recorded in human history (Marmer, 1922), their importance to the global ocean has been getting attention recently after decades of silence. In 2004, Wunsch and Ferrari (2004) argued that the wind and heat are insufficient for driving global thermohaline circulation by the energy budget aspect because the cross-isopycnal energy dissipation is lacking. To transfer the energy from wind and heat driving surface into the deep ocean, the small-scale mixing process induced by internal tides is pivotal (Wunsch and Ferrari, 2004). Because of the critical latitude and fragile topography required for tidal wave's propagating and breaking (Haidvogel *et al.*, 1993; Hibiya and Nagasawa, 2004; Lam, Maas and Gerkema, 2004; White and Mohn, 2004; Sansón, 2010), the tides can no longer be silenced as even-distributed ocean noises (Robertson, Dong and Hartlipp, 2017). Additionally, the ocean basin's continental boundary and seamounts are suggested as the potential channel for deep water overturning (Tanaka, Hibiya and Niwa, 2007; Robertson, Dong and Hartlipp, 2017; Robertson and Dong, 2019).

However, the continental boundary is not only the tidal activity hotspots but also dominated by the wind-driven large-scale boundary currents, such as East Kamchatka Current (EKC) flowing along with the Kuril Islands (Yasuda, Okuda and Shimizu, 1996; Katsumata and Yasuda, 2010; Kida and Qiu, 2013) and Antarctic Slope Current (ASC) flowing along with the Antarctic shelves (Thompson *et al.*, 2018), which are vital to global climate by their role in regional water exchange system. Conventionally, the tidal influences on the boundary currents are not considered since the tides are high-frequency and small-scale motions compared to basin-wide boundary currents; moreover, due to model capacity, the tidal influences in large scale ocean general circulation model (OGCM) are ignored (Robertson, Dong and Hartlipp, 2017). Therefore, the influences of tides on boundary currents and their resultant to global climate are blank in nowadays ocean dynamics, although these boundary currents experienced the regional tidal rectification flows and extended vertically to the intermediate layer, where the tidal breaking is usually detected (Gargett and Holloway, 1984; Hibiya, Nagasawa and Niwa, 2006).

1.2 Tide generated topography trapped waves on the continental edge

There are two typical tidal phenomena observed on the continental edge: vertical mixing and topographic trapped waves. Despite the vertical mixing induced by tidal wave's breaking, the topography trapped wave is also a resulting effects of tides on the continental shelves or isolated seamounts in high-latitude areas (Robinson, 1981; White and Mohn, 2004; Lavelle and Mohn, 2010; Mohn *et al.*, 2013; Robertson, Dong and Hartlipp, 2017). When the impinging tide's frequency less than the inertial frequency ($T_f = 2\pi/f$, where f is Coriolis parameter; also known as the critical latitude), which so-called sub-inertial oscillation (Brink, 1990; Lavelle and Mohn, 2010; Sansón, 2010), the tidal waves are propagating along with the potential vorticity contour as Rossby waves and amplified on the slope due to topography-beta effect. For conservating the potential vorticity in responses to waves' perturbations vicinity to flank topography, the tidally-generated amplified waves clockwise propagates around the isolated topography features and thus so-called topography trapped waves (Eriksen, 1991).

The tidally-generated topography trapped waves around the isolated seamounts (hereafter refers to seamount trapped waves) is often observed in real ocean. Eriksen (1991) found that the tidally-resonant excitation of seamount trapped wave around the Fieberling Guyot in the northeast Pacific (Eriksen, 1991). Later in 1997, Codiga and Eriksen identified the same phenomena at Cobb Seamount (Codiga and Eriksen, 1997). These two studies begin the discussion of local influences caused by the seamount trapped waves. A clockwise toroidal residual circulation is formed above the seamount caused by tidal rectification (Brink, 1990; Haidvogel *et al.*, 1993; Beckmann and Mohn, 2002; Lavelle, Lozovatsky and Smith IV, 2004; Lavelle and Mohn, 2010), which is the process associated with time-mean deviations of the non-linear wave solutions (Chapman, 1989; Brink, 1990; White and Mohn, 2004). Beckmann and Haidvogel (1997) then reproduced the tidally-rectified residual recirculation at Fieberling Guyot and revealed the physical mechanism governed (Beckmann and Haidvogel, 1997). The trapped clockwise residual vortex above the seamount is caused by diurnal tides amplification along with the flank. A time-mean density perturbation caused three-dimension overturning cell then formed associated with the rectified residual circulation, which has a downward motion over the seamount summit and an upwelling at the edge of the rectified residual circulation. The overturning cell is thus the regional hotspot of bio-productivity and nutrient circulation because it provides an exchange channel connected surface and deep layers (Beckmann and Haidvogel, 1997; White and Mohn, 2004; Lavelle and Mohn, 2010).

However, the discussion of influences of the tidally-rectified residual circulation to the boundary current system is absent in past studies, although the residual circulation is also excited in boundary current dominated regions, especially the regions higher than diurnal tide (K1 tide)'s critical latitude (30°), such as Kuril Islands (Nakamura *et al.*, 2000; Nakamura and Awaji, 2001; Shu *et al.*, 2021).

1.3 Climate sensitive area: Kuril Islands

The Kuril Islands is a world-class tidal hotspots located at the North Pacific's continental edge, and because it regulates the water exchange and associated with nutrient transport between the Sea of Okhotsk and the North Pacific (Nishioka, Mitsudera, *et al.*, 2014), the tidal influences on this area is suggests to impact on Pacific climate and overall bio-productivity (Katsumata *et al.*, 2004; Yasuda, 2009; Watanabe, Yasuda and Tsurushima, 2014; Yamashita *et al.*, 2021). Previous studies mostly focus on the tidally-enhanced vertical mixing along the Kuril Islands (Nakamura and Awaji, 2004; Nakamura *et al.*, 2006, 2014; Kawasaki and Hasumi, 2010; Tanaka *et al.*, 2010, 2014; Tanaka, Hibiya and Niwa, 2010), and has seldom mention the tidal impacts to the interbasin exchange, although the seamount trapped waves is vital along with the Kuril Islands caused by the sub-inertial diurnal tides (Kowalik and Polyakov, 1998; Nakamura *et al.*, 2000; Ono *et al.*, 2006).

Nakamura *et al*. (2000) reveals that the seamount trapped waves along the Kuril Islands contribute to the interbasin exchange by only-tides numerical simulation. Without the wind forcing, the tidally-rectified residual circulation formed around the islands on the Kuril Island Chain. The negative vorticity at the both side of wide straits is generated by time-averaging and thus a time-mean bi-direction exchange occurred (Nakamura *et al.*, 2000). However, the interbasin exchange estimated by Nakamura *et al*. (2000)'s tide-only model is not comparable to the observations. It does not imply that the interbasin exchange is irrelevant to the tides. For instance, although Kida and Qiu (2013) suggests that the western boundary current (WBC), the EKC, is the driver for interbasin exchange by circular theorem (see Appendix 1 for details) (Kida and Qiu, 2013), the simulated interbasin exchange is extreme small still in other high-resolution models unless the tidal forcing is added. Later in this thesis, we show that the high-resolution models do not usually account for tidal forcing and thus tend to estimate unrealistically low interbasin transport volumes, although they can resolve strong boundary currents and topographic features accurately. In addition to Nakamura *et al*. (2000)'s tide-only estimation, it suggests that the interbasin exchange is governed by the WBC and the tidal forcing together, and neither of them is neglectable. The modification of wind-driven boundary current by tides is thus waiting for being revealed. Therefore, this study elucidated a previously uncharacterized mechanism of interbasin exchange transport dynamics by tidal forcing using cutting edge OGCMs, suggesting that the interaction between tidal current and seamount is needed on the WBC's pathway for the precise water exchange transport between the Sea of Okhotsk and North Pacific.

The critical latitude of diurnal tides suggests that the similar phenomena is occurred not only in the north hemisphere but also the polar and sub-polar regions in south hemisphere, such as the Antarctic continental slope. The Antarctic continental slope is also dominated by a wind-driven boundary current ASC and suggested to has enormous tidal activities (Flexas *et al.*, 2015; Thompson *et al.*, 2018; Stewart, Klocker and Menemenlis, 2019). The cross-slope water exchange in the Antarctic continental shelf could cause the sea level rise by melting the ice shelves, in which the water exchange modulated by ASC's pathways (Rintoul *et al.*, 2016). Similar to the Okhotsk-Pacific interbasin exchange, the ASC is modified by the interaction between the tidal forcing and the topography features in continental shelf, has been suggested.

1.4 Argument of this study

Finally, we argue that the tidal effect is important to boundary currents and resultant to the global climate in this research. After introducing the models and data we used for this study in Chapter 2, the case study of Okhotsk-Pacific interbasin exchange problem in Chapter 3 provides a new aspect in inclusive of tidal oscillations in high-resolution models, especially when dominant boundary currents and topographic features are accurately resolved by increased resolution. Further, a discussion of possible tidal impacts on the Antarctic continental slope is followed in Chapter 4, expanding the picture of tidal impacts on the boundary current system globally. Comprehensively, our study illustrates the role of tides to boundary currents from an ocean dynamics standpoint.

This page intentionally left blank

Chapter 2

Models and Data Description

2.1 Models

We used the CCSR Ocean Component Model (COCO) and the Ocean General Circulation Model For the Earth Simulator (OFES) for investigating the Okhotsk-Pacific interbasin exchange problem, which all are high-resolution ocean general circulation models (OGCMs) obtained the whole North Pacific regions. Comparison of the OFES and COCO model suggests the generality of the wind-driven East Kamchatka Current (EKC) pathway and its resultant interbasin exchange. By obtaining the tidal forcing in the COCO model, the differences of the tidal and the non-tidal configured models identify the tidal impacts on the Okhotsk-Pacific exchange system. Our further analysis and experiments to detect the mechanism of tidal impacts on the western boundary current (WBC) are continuously based on the COCO model. Finally, regional models built by the Massachusetts Institute of Technology General Circulation Model (MITgcm) is complemented for discussing the tidal impacts on the Antarctic continental slope.

2.1.1 CCSR Ocean Component Model (COCO)

The CCSR Ocean Component Model (so-called COCO) is an OGCM developed by the Atmosphere and Ocean Research Institute of the University of Tokyo (Hasumi, 2006). The present model configurations are the same as those of Matsuda *et al*. (2015), which covers the Pacific Ocean from 10°S to 67°N meridionally and 100°E to 90°W zonally (Fig. 2.1**a**). This obtains all important marginal seas of the North Pacific, including the Sea of Okhotsk, the Bering Sea, the South Sea, the Japan Sea, and the Indonesian Straits. The Sea of Okhotsk is configured to be high resolution (finer than 3 km in the northern shelf region and 5 km around the Kuril Islands that divide the Sea of

Okhotsk from the North Pacific) by using a curvilinear coordinate grid (Fig. 2.1**b**). Vertical grids are totally 84 layers composed of 7 sigma coordinate layers shallower than 35 m, followed by 36 z-coordinates layers with 10 m thickness intervals, and 41 z-coordinate layers by thickness interval exponentially increases from 12 m to 600 m. The model's bottom topography is adapted from the Japan Oceanographic Data Center (JODC) and modified by Ono *et al*.(2006) and Matsuda *et al*.(2015). However, we eliminated the extra vertical diffusivity around the Kuril Islands added by Matsuda *et al*. (2015).

The atmospheric forcing that drives ocean and sea ice dynamics in the COCO model are the monthly-averaged climatology forcing from the Ocean Model Intercomparison Project (OMIP) (Röske, 2005, 2006) based on 15 years of daily reanalysis data from 1979 to 1993 obtained from the European Centre for Medium-Range Weather Forecasts (Röske, 2005), coupled with monthly-averaged river runoff data from Dai and Trenberth (2002). The sea ice motion dynamics are based on elastic-viscous-plastic rheology. Readers may refer to Matsuda *et al*. (2015) for further details of the model configuration.

The tidal forcing of the K1(diurnal) constituent is given by the tidal potential $\boldsymbol{\xi}$ in the barotropic momentum equations such that

$$\frac{\partial \boldsymbol{u_T}}{\partial t} + (\boldsymbol{u_T} \cdot \nabla)\boldsymbol{u_T} + f\boldsymbol{k} \times \boldsymbol{u_T} = -g\nabla(\alpha_0\eta - \beta_0\xi) + A_H\nabla^2\boldsymbol{u_T}, \tag{2.1}$$

where $\boldsymbol{u_T}$ is the barotropic velocity and A_H is the horizontal eddy diffusivity. The tidal potential is written as $\xi = K\sin2\phi\cos(\sigma t + \lambda)$ for the diurnal tide, where ϕ and λ

are the latitude and longitude, respectively, with the amplitude K= 0.14 m, frequency $\sigma = 0.72921 \times 10^{-4}$ s^{-1}, and $(\alpha_0, \beta_0) = (0.90, 0.69)$ (Schwiderski, 1980). The model configuration for the non-tidal cases does not consider ξ in the barotropic momentum equation. Please see Matsuda *et al*. (2015) for more details on the validation of simulated tidal currents.

In the first year of the model integration, the temperature and salinity were restored to the World Ocean Atlas 2009 (WOA09; see Appendix 2) (Matsuda *et al.*, 2015). We then span it up for 60 years by the climatology OMIP dataset same as Matsuda *et al*. (2015) but without tidal forcing. We used the model's final outputs as our initial conditions. We next span it up for 45 years by the same climatology OMIP forcing with the tidal and non-tidal configurations according to Matsuda *et al*. (2015) as the tidal and non-tidal cases, respectively. The last year's model output was used for analysis.

Two numerical experiments listed below are executed in Chapter 3 for investigating the impacts of tidally-generated topography trapped waves and enhanced vertical mixing on the EKC, respectively.

2.1.1.1 Numerical experiments: transition experiment

The transition experiment was conducted by activating tidal forcing (ξ) in the momentum equation (2.1) for 65 days of simulation. This experiment helps to visualize and analysis the tides' contribution in altering the EKC's pathway. The initial state of the experiment is the final day of June of the non-tidal case, and the rest of the forcing parameters, including heat flux, wind stress, and freshwater flux, remained the same as those in June. The impacts of tidal forcing with no influence from other forcing parameters were modeled by maintaining wind and heat forcing constant for 65 days from the end of June. The analyses were conducted using the model output recorded every 1.1975 (=23.95/20) hours, where 23.95 hours represents the K1-tidal-period.

2.1.1.2 Numerical experiments: Vertical mixing experiments

The vertical mixing in the COCO model is modeled by a turbulent closure scheme by Noh and Kim (1999) such that

$$A_v = Sql, \text{ and } K_v = \frac{Sql}{P_r}, \tag{2.2}$$

where A_v is the vertical viscosity, and K_v is the vertical diffusivity. l and q are turbulence length scale and root-mean-square velocity of turbulence, respectively. S is a coefficient parameterized as $S = S_0/\sqrt{1+\alpha R_{it}}$, where S_0 is given as 0.39, $\alpha = 3$ is a constant for proportionality, and R_{it} is the turbulent Richardson number, $R_{it} = (Nl/q)^2$, where N^2 is the buoyancy frequency, $-g{\rho_0}^{-1}\,\partial\rho/\partial z$. P_r is the Prandtl number, where $P_r = P_{r0} + \beta R_i$, P_{r0} and β are constants equal to 0.8 and 7, respectively, and R_i is the Richardson Number, $R_i = N^2/[(\partial u/\partial z)^2 + (\partial v/\partial z)^2]$.

Here we designed two types of vertical mixing experiments for testing the vertical diffusivity function in water exchange transport. The first experiment was the case without tide but enhanced vertical mixing (hereafter refers to non-tidal-TM case), which was executed by substituting the tidal case's vertical diffusivity value into the non-tidal model monthly for 5 years to detect the influences of tidal mixing without residual tidal currents. Second, we conducted sensitivity tests enforcing the vertical diffusivity value to be zero in the tidal model configuration, which we referred to as the tidal-NoM case. The models were spun up for 5 years under climatological forcing. The model outputs of the last year were used for analysis in both settings.

2.1.2 Ocean General Circulation Model For the Earth Simulator (OFES)

The ocean model output from the Ocean General Circulation Model for the Earth Simulator (OFES) 1/30° (Sasaki and Klein, 2012; Sasaki *et al.*, 2014) was also used for this case. The model domain ranges from 100°E to 70°W and from 20°S to 68°N with 100 vertical levels, encompassing the marginal seas in the North Pacific (Fig. 2.2). Each grid's size is 1/30° x 1/30°. The bathymetry data was obtained by merging the General bathymetric Chart of the Oceans (GEBCO) (1 minute) (*Historical GEBCO data sets*) and JTOPO30 (*MIRC JTOPO30*). Vertical mixing in the mixed layer was parameterized as the vertical diffusivity coefficients by Noh and Kim (1999). First, we conducted the climatological integration of the OFES 1/10° simulation for 15 years, which was 30 years spun up by the temperature and salinity data of WOA13 as the initial state (Sasaki and Klein, 2012). Afterward, a hindcast OFES 1/10° simulation was conducted from 1979 until 2000. Ultimately, the OFES 1/30° simulation spanned from January 1, 2000, to December 31, 2003, which was forced by the historical atmospheric reanalysis data of the JRA-25 (Onogi *et al.*, 2007). Data corresponding to the year 2003 was used in this study.

2.1.3 Massachusetts Institute of Technology General Circulation Model

(MITgcm)

The regional Massachusetts Institute of Technology General Circulation Model (MITgcm) is used for discussing the possible tidal impacts on the Antarctic Slope Current in the southern hemisphere. The present model configurations are the same as those of Nakayama *et al*. (2021), which ranges from 60°S to 70°N meridionally and 90°E to 150°E zonally (Fig. 2.3) on the East Antarctica with hydrostatic approximation, dynamic/thermodynamic sea-ice (Losch *et al.*, 2010), and thermodynamic ice shelf (Losch, 2008). It obtains the major ice shelves which are Shackleton, Tracy Tremenchus, Conger, Vincennes, Totten, Moscow University, Holmes, and Dibble ice shelves, from west to east respectively (Fig. 2.3). The horizonal resolution is approximately 3 km x 3 km. Vertical grids are totally 50 layers composed of 7 z-coordinate layers with 10 m thickness intervals, followed by 43 z-coordinate layers by thickness interval exponentially increases from 10 m to 456 m (Gwyther *et al.*, 2014). The model's bottom topography is adapted from the ETOPO1 (Amante and Eakins, 2009) and modified by Nakayama *et al.* (2021) with the updates from Aurora (Rintoul *et al.*, 2016), Japan and airborne gravity measurements by the USA.

The atmospheric forcing that drives ocean in the MITgcm are the daily-averaged climatology forcing provided by ERA-Interim (Dee *et al.*, 2011) and adjusted by ECCO (Estimating the Circulation and Climate of the Ocean) adjoint-model-based methodology (Wunsch and Heimbach, 2013). The monthly-averaged lateral ocean boundary conditions are built from ongoing ECCO LLC270 optimization (Zhang, Menemenlis and Fenty, 2018). The ice shelf draft is from Antarctic Bedrock Mapping (BEDMAP-2) (Fretwell *et al.*, 2013). Readers may refer to Nakayama *et al*. (2021) for further details of the model configuration. The tidal forcing of 10 tidal constituents is superimposed on the ocean lateral boundary condition given by the tidal currents from the CATS2008A inverse barotropic tide model (Padman *et al.*, 2002; Padman, Siegfried and Fricker, 2018; Nakayama *et al.*, 2019) .

We used the potential temperature and salinity field from WOA09 (Levitus *et al.*, 2010) January as initial state. The model then spun up for 25 years from January 1992 to December 2016 without tidal forcing. Then we drive the model's final output of December 2016 for 25 years again with same atmospheric forcing from 1992 to 2016 with/without the tidal lateral boundary conditions for discussion. For fitting the time-resolution with the moorings data, hourly-averaged atmospheric forcing are used from 2009 to 2012. The period 2009 to 2012's 30 min averaged data model outputs were used for analysis.

2.2 Data

Two dataset from Peña-Molino *et al*. (2016) were used in the discussion for comparing with the MITgcm outputs.

Five moorings were deployed along with ~113°E on the continental slope as Fig. 2.4 shown. They recorded the 30 min average horizontal velocity and pressure by Vector Averaging Current Meters (VACM) distributed on 500 m and the bottom from December 2009 to January 2012. Only the station 1 is used in this study because it located at the Antarctic Slope Current pathway. Details of mooring deployments refers to Peña-Molino *et al*.(2016). Since we purpose to detect the tidal oscillations, the mooring data we used has not been filtered.

The additional temperature and salinity measurements from a CTD (Seabird911) is also used in discussion. It was collected along the mooring line in January 2012 during the recovery of moorings with higher horizontal resolutions compared with the mooring stations. The temperature and the estimated density profile provide the ASC structure along with the Antarctic continental slope, which is valid for model data validation (Fig. 2.4).

This page intentionally left blank

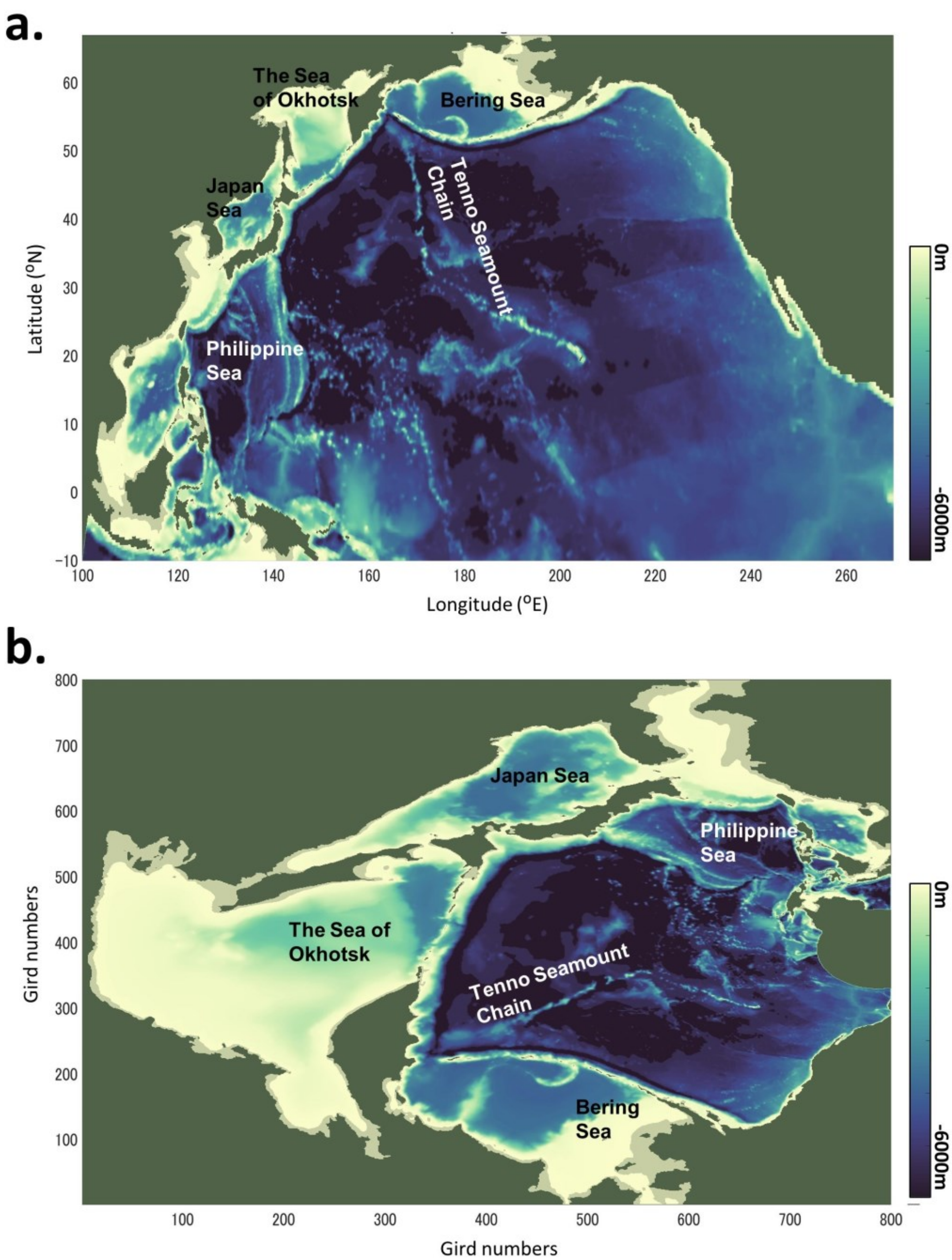

Figure 2.1 The model domain in COCO. a. Topography of the COCO model after the coordinate transfers. It covers the Pacific Ocean from 10°S to 67°N meridionally and 100°E to 90°W zonally. This includes all important marginal seas of the North Pacific, including the Sea of Okhotsk, the Bering Sea, the Japan Sea, and the Indonesian Straits. **b**. the original topography of the model. The Sea of Okhotsk is configured to be high resolution (finer than 3 km in the northern shelf region and 5 km around the Kuril Islands that divide the Sea of Okhotsk from the North Pacific) by using a curvilinear coordinate.

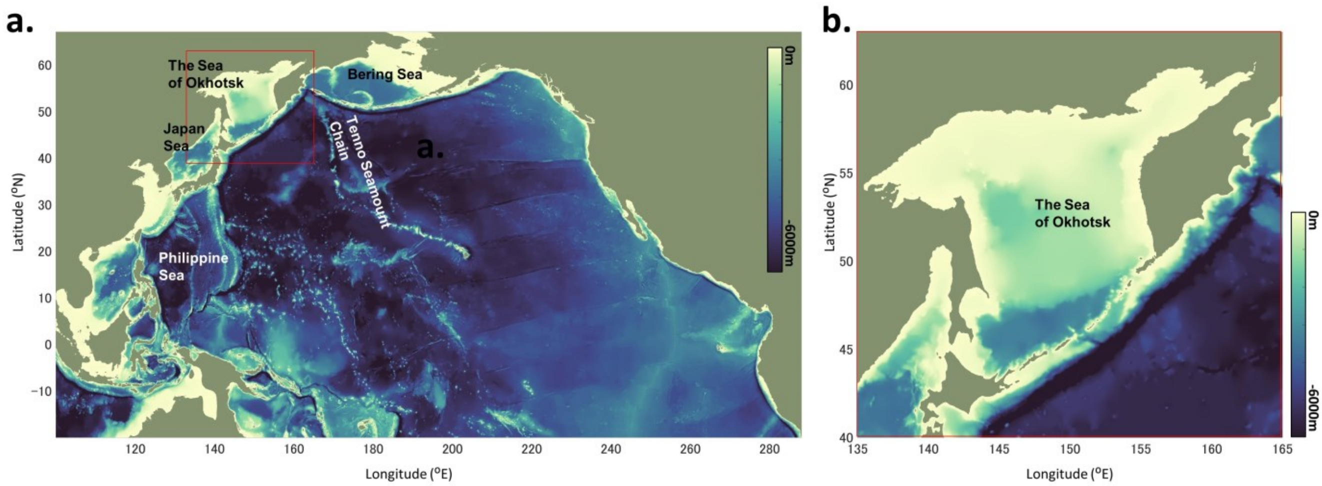

Figure 2.2 The model domain in OFES. a. Original topography of the OFES model. It covers the Pacific Ocean from 19°S to 67°N meridionally and 100°E to 72°W zonally. This also includes all important marginal seas of the North Pacific, including the Sea of Okhotsk, the Bering Sea, the Japan Sea, and the Indonesian Straits as COCO (Fig. 2.1**a**). **b**. the details of Sea of Okhotsk in the OFES. Each grid is 1/30° x 1/30°.

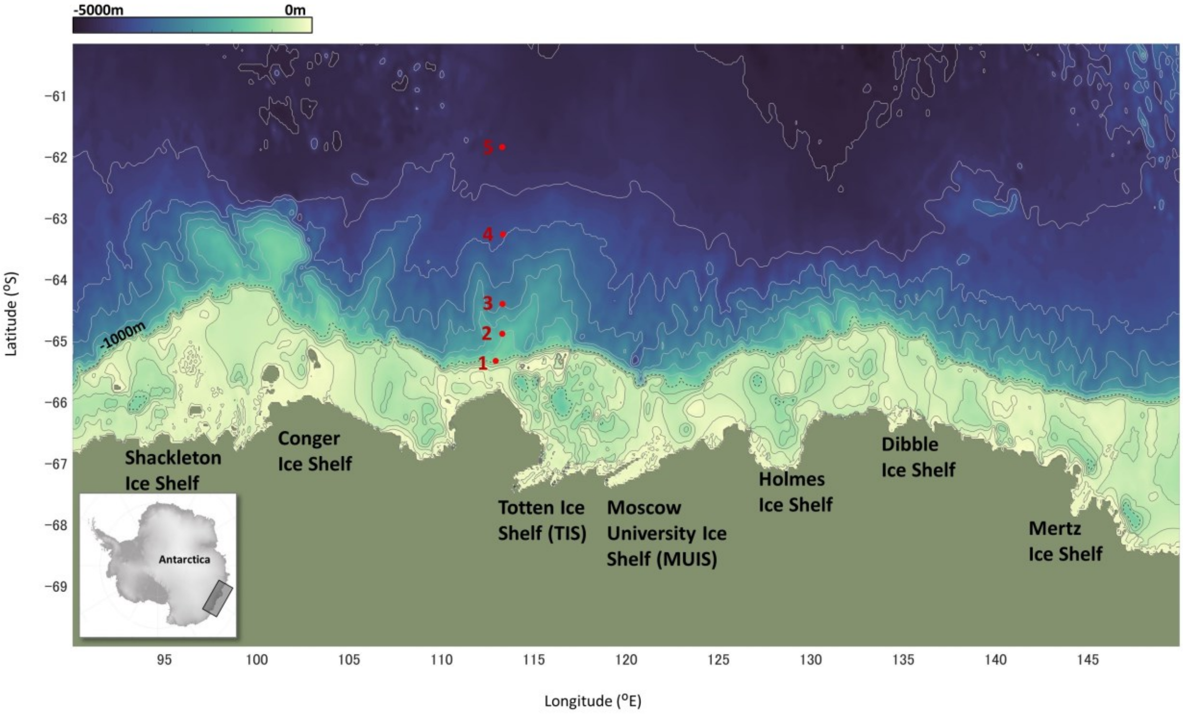

Figure 2.3 The model domain in MITgcm. Original topography of the MITgcm model. It covers the East Antarctic from 60°S to 70°S meridionally and 90°E to 150°W zonally with approximately 3 km x 3 km resolution. It obtains the major ice shelves which are Shackleton, Conger, Totten, Moscow University, Holmes, and Dibble ice shelves, from west to east, respectively. The black-dashed contour denotes the 1000 m depth. Grey contours shallower/deeper than 1000 m represent the depth contours with 200 m/1000 m intervals, respectively. The red dots denote 5 mooring stations deployed by Peña-Molino *et al*.(2016).

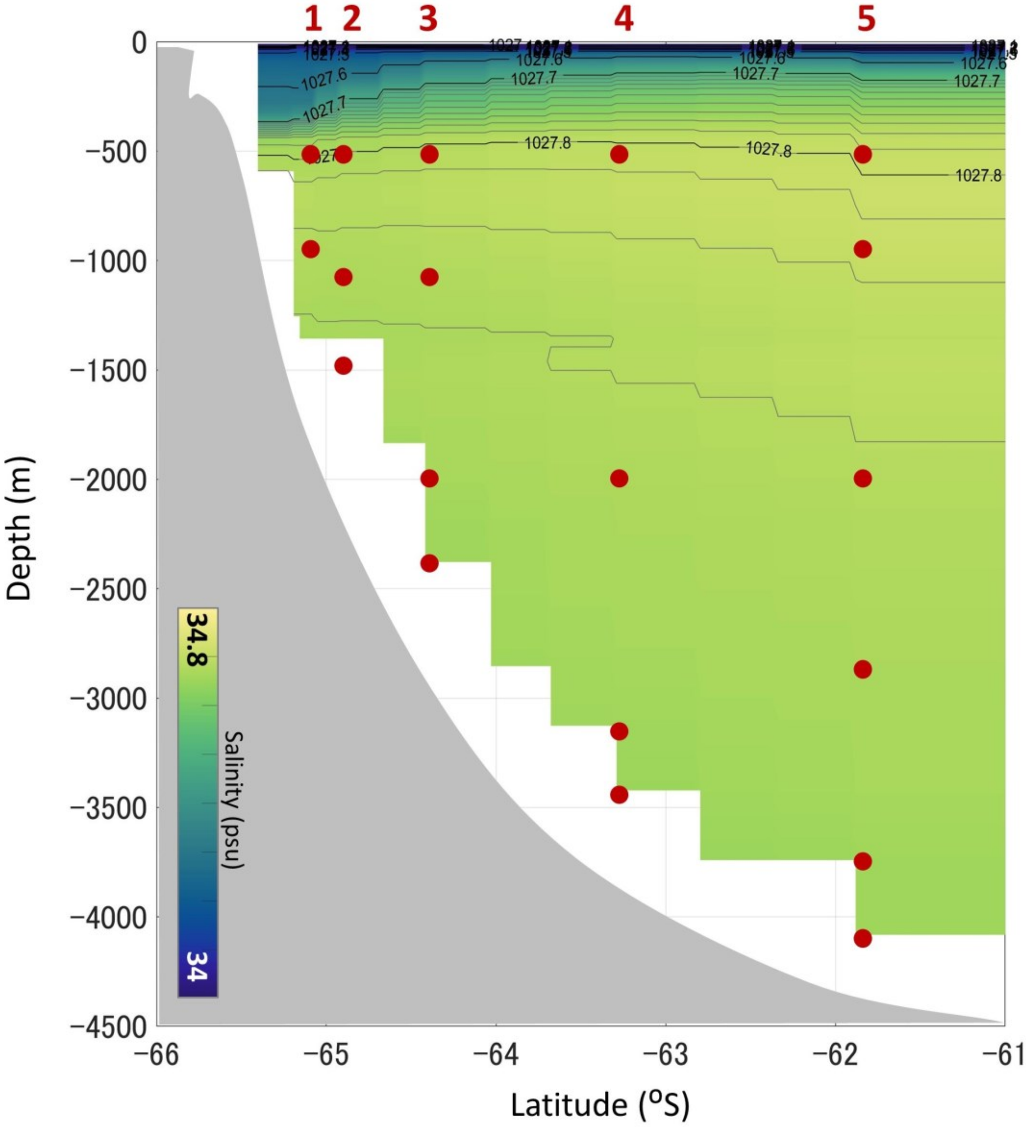

Figure 2.4 The mooring stations and the salinity profile from CTD. Red dots denote the depth of 5 moorings stations (Peña-Molino *et al.*,2016) shown in Fig. 2.3. Only the velocity data from station 1, 500 m depth one is used for this study. Shade is the salinity detected by CTD in January 2012. Black contours denote the isopycnal layers from 1027.0 to 1027.8 kg m^{-3} with 0.1 kg m^{-3} intervals. The dark-grey contours are 0.01 kg m^{-3} intervals between 1027.7 and 1027.8 kg m^{-3}, as well as the ones below 1027.8 kg m^{-3}.

Chapter 3

Tidally modified western boundary current drives interbasin exchange between the Sea of Okhotsk and the North Pacific

3.1 Introduction

We focus on the East Kamchatka Current (EKC), the western boundary current (WBC) flows between the Sea of Okhotsk and the North Pacific, as our main study case. The water exchange between the Sea of Okhotsk and the North Pacific is an essential component of the overturning circulation that ventilates the intermediate layer of the North Pacific (Talley, 1993). Surface water originating in the subarctic gyre enters the Sea of Okhotsk through the Kuril straits (Talley, 1993; Yasuda, 1997). It then subducts to the intermediate layer (300–500 m, within the 1026.8–1027.0 kg m^{-3} isopycnals) due to active sea ice formation over the northern continental shelves (Talley, 1993; Yasuda, 1997), and finally outflows to the North Pacific across the Kuril straits, resulting in the North Pacific Intermediate Water (NPIW) (Talley, 1993; Yasuda, 1997) that circulates in the subtropical gyre. Further, the outflow from the Sea of Okhotsk entrains abundant nutrient materials such as iron, which support high primary production contributing not only to abundant fisheries resources but also to a vast amount of CO_2 uptake in the western North Pacific (Nishioka, Mitsudera, *et al.*, 2014; Nishioka, Nakatsuka, *et al.*, 2014; Lembke-Jene *et al.*, 2017).

Despite this significance, the mechanisms that drive the Okhotsk-Pacific exchange remain largely uncharacterized, as the EKC (see Fig. 3.1**a**), a WBC of the subarctic North Pacific, intrudes only partially into the Sea of Okhotsk through straits along the Kuril Islands. Current studies have not yet elucidated what determines the EKC's partial intrusion. Most of the interbasin exchange occurs through the two deepest straits along the Kuril Islands (Katsumata *et al.*, 2004; Katsumata and Yasuda, 2010; Ohshima *et al.*, 2010), which are the Kruzensterna Strait to the north (hereinafter referred to as ‘the northern strait’; No. 4 in Fig. 3.1**a** with a depth of 1900 m (Ohshima *et al.*, 2010)) and the Bussol’ Strait to the south (hereinafter referred to as ‘the southern strait’; No. 9 in Fig. 3.1**a** with a depth of 2200 m (Nakamura *et al.*, 2000; Katsumata *et al.*, 2004)), separated by the Middle Island Chain (MIC). Based on hydrographic data, Katsumata and Yasuda (2010) published a concise summary of previous throughflow estimates, in addition to their estimate of -5.6 Sv (1 Sv $\equiv 10^6$ m^3 s^{-1}) and +6.6 Sv (annual average) through the northern and southern straits, respectively, where the negative (positive) symbol denotes the Okhotsk-ward (Pacific-ward) throughflow. Further, based on lowered acoustic Doppler current profiler measurements, Katsumata *et al.* (2004) estimated an outflow of approximately +8.2 to +8.8 Sv via the southern strait during summer. Although transport estimates are rare, the exchange likely occurs with an Okhotsk-ward inflow through the northern strait and a Pacific-ward outflow through the southern strait (Katsumata and Yasuda, 2010). Kida and Qiu (2013) reported that the intrusion of the EKC (Fig. 3.1**b**) would occur when the EKC collided with the MIC after passing the North Bank upstream (Fig. 3.1**a**; 86 m depth at the top (Rogachev and Shlyk, 2018a)) by creating a bifurcation (red dot in Fig. 3.1**b**) on a streamfunction contour ψ_1 that coincides with the contour surrounding the MIC. A part of the EKC branches northward at the bifurcation and forms a partial intrusion with a transport of $\psi_2 - \psi_1$ (Fig. 3.1**b**), where ψ_2 is the streamfunction contour along the land on the other side of the MIC. Therefore, the partial exchange occurs due to the presence of the EKC’s bifurcation on the MIC. In other words, the subtle change of EKC’s pathway potentially determines the large-scale flow pattern.

A question has arisen regarding the processes that control the bifurcation that leads to the partial intrusion. Kida and Qiu (2013) evaluated ψ_1 around an island with a vertical wall on a flat bottom (Fig. 3.1**b**) by applying a circulation theorem (see Appendix 1). However, their configuration is not directly applicable to reality, as the MIC is composed of a chain of islands over a sloping submarine ridge rather than a single island. Further, it is not even evident whether a streamfunction contour can be identified along the EKC that hits the MIC and forms a bifurcation point. For example, a recent simulation of the Ocean General Circulation Model for the Earth Simulator (OFES) with a 1/30° grid resolution (Sasaki and Klein, 2012; Sasaki *et al.*, 2014) demonstrated a reversed +1.1 Sv Pacific-ward transport through the northern strait, coupled with a -0.8 Sv Okhotsk-ward current via the southern strait (Fig. 3.2**a**). By observing the streamfunction, we found that the EKC overshoots bypassing the two deepest straits without forming a bifurcation on the MIC (Fig. 3.2**b-c**), resulting in spurious results. This was apparently a hidden problem that was uncovered through the optimized physics of cutting-edge ocean general circulation model (OGCM) approaches, considering that the OFES with a coarser resolution (1/10°) reproduced exchange transport dynamics that were consistent with the observed estimates (Katsumata and Yasuda, 2010) (Fig. 3.2).

In this study, we demonstrate that tidal forcing is the missing mechanism that drives interbasin exchange caused by the partial intrusion of the EKC. By adopting an ocean model (CCSR Ocean Component model, hereinafter referred to as the COCO (Hasumi, 2006); see Chapter 2 Models and Data Description, and Matsuda *et al.* (2015)) with a curvilinear coordinate system, a resolution of approximately 5 km (1/20°) around Kuril Islands, and accounting for diurnal tides in the simulation (referred to as the tidal case), the model estimated a throughflow transport of -4.0 Sv through the northern strait and +8.7 Sv via the southern strait (Fig. 3.1**c**), thus realistically reproducing the observed estimates (Katsumata and Yasuda, 2010). However, once the tidal forcing was turned off (referred to as the non-tidal case), the throughflow transport almost vanished, as illustrated in Fig. 3.1**c**, which represented a spurious result similar to the OFES at a 1/30° resolution mentioned above. This indicates that tidal forcing is an indispensable driver of interbasin exchange. The Kuril Islands region features vigorous tidal oscillations and currents (Kowalik and Polyakov, 1998) dominated by the diurnal tides (Nakamura *et al.*, 2000), of which the tidal current's amplitude sometimes exceeds 1.5 m s^{-1}. In a previous study, by implementing a numerical model that only accounted for tides in which the EKC is absent, Nakamura *et al*. (2000) estimated the net exchange transport to be +0.4 Sv and +0.9 Sv through the northern and southern straits, respectively, both of which were Pacific-ward. That is, the tide-only model did not accurately represent the proper exchange transport dynamics either. This implies that the interaction between diurnal tides and the EKC is an essential driver of interbasin exchange. Here, we present a new mechanism for tidal control on the EKC's pathway that leads to the partial intrusion to the Sea of Okhotsk from a potential vorticity (PV) dynamics standpoint.

3.2 Results

3.2.1 Overview of the tidal and non-tidal flow field

In this section, we analyzed the EKC path difference between the tidal and non-tidal cases and explored the roles of the tides on the exchange processes. The tidal case of the COCO, which was spun up by climatological forcing (see Chapter 2 Models and Data Description), estimates that the seasonal variation of the throughflow transport ranges from -5.4 to -1.9 Sv through the northern strait, and from +7.6 to +9.8 Sv via the southern strait (Fig. 3.3**a**), which is consistent with the observed estimates (Katsumata and Yasuda, 2010). Given that the exchange transport difference between the two cases is sufficient in both straits regardless of the season, we will focus on the generality of this difference induced by tides rather than seasonality. The June flow field was used in the following analysis, when the local wind stress curl around the MIC is weak, as well as the flow pattern is most typical compared to other months, where the EKC's streamfunction contour encompasses most of the MIC, as illustrated in Fig. 3.1**b** (see Appendix 1 circulation theorem and Appendix 2 for seasonality discussion).

The depth-averaged velocity $[\boldsymbol{u}]$ of the tidal case in June indicates an Okhotsk-ward flow through the northern strait and a Pacific-ward flow via the southern strait (Fig. 3.4**a**). Here, we define $[\blacksquare] = \frac{1}{H}\int_{-h}^{\eta} \blacksquare \, dz$ as a depth-averaged value, where $\blacksquare$ represents arbitrary variables, z denotes the vertical coordinate, and $H = \eta + h$ represents the local water thickness, which equals the sum of the bottom depth h and the sea surface height η. The EKC deflects westward immediately after it passes the North Bank and approaches the MIC. Figure 3.4**b** depicts the flow field by a streamfunction ψ, defined by vertically-integrated velocity:

$$\frac{\partial \psi}{\partial x} = H[v], \qquad -\frac{\partial \psi}{\partial y} = H[u], \tag{3.1}$$

where u and v denote the zonal and meridional velocity, and x and y are the zonal and meridional coordinates, respectively. The streamfunction contour $\psi = -1.5 \times 10^6$ m^3 s^{-1} extends from the North Bank toward the northern strait along with the EKC (red contour in Fig. 3.4**b**). At the same time, $\psi = -1.5 \times 10^6$ m^3 s^{-1} surrounds the MIC. The two contours encounter approximately at 47.8°N, 153.6°E (indicated by a yellow arrow in Fig. 3.4**b**), forming a bifurcation point. This indicates that the transport of the EKC represented by $-1.5 \times 10^6 < \psi \lesssim 0$ m^3 s^{-1} is forced to flow through the northern strait. The geometrical features of the streamfunction in the tidal case agrees with those of Fig. 3.1**b,** in which the partial intrusion of the EKC occurs.

In contrast, the EKC in the non-tidal case bypasses most of the MIC (Figs. 3.4**d** and **e**). As a result, interbasin exchange is almost abolished, with weak Pacific-ward throughflows via both the northern and southern straits (Fig. 3.4**d**). The streamfunction depicts a clockwise flow pattern encompassing the MIC that blocks the interbasin exchange, and no bifurcation point forms in this case (Fig. 3.4**e**). We observed that the 1/30° resolution OFES (which does not incorporate tidal forcing) also displays a similar clockwise circulation surrounding the MIC, which makes the EKC bypass the deep straits (Fig. 3.2**b**) in a manner resembling the non-tidal case. These non-tidal results markedly contrast with those of the tidal case, implying that tidal forcing plays an essential role in the partial intrusion of the EKC.

One of the main differences between the tidal and non-tidal cases is the presence of seamount trapped waves in the former that propagate in the clockwise direction around topographic features such as the MIC and the North Bank (Nakamura *et al.*, 2000; Tanaka *et al.*, 2014) (see Fig. 3.5 and Supplementary Movie 1). Further, a tidal-period-mean velocity indicates that tidally-rectified, clockwise circulations are generated around the islands and seamounts (Nakamura *et al.*, 2000). The tidally rectified circulation is prominent over the North Bank of the tidal case (compare Fig. 3.4**a**, blue arrows point, and 3.4**d**), which has been evidenced in the study site by the trajectories of Argo floats and surface drifters (Rogachev and Shlyk, 2018b).

To discuss the deflection of the EKC by interaction with these tidal motions, we focused on the bottom velocity around the North Bank. By comparing Figs. 3.4**c** and 3.4**f**, we found that the bottom velocity is much stronger in the tidal case, whereas in the non-tidal case, the along-slope bottom velocity is very weak or even reversed downstream of the North Bank (Fig. 3.4**f**; indicated by red arrows). Therefore, the EKC is hardly constrained by the topography in the downstream region in the non-tidal case, and thus the EKC overshoots passing by the deep straits at both ends of the MIC. In other words, bottom steering occurs due to tides, which forces the EKC to bend toward the northern strait after passing the North Bank, leading to the intrusion of the EKC water into the Sea of Okhotsk. The question now is why and how such a bottom steering of the EKC occurs in the tidal case. Is the bottom steering of the EKC a result of the trapped waves and/or the tidally-rectified circulation?

3.2.2 Transition experiment from non-tidal to tidal state

To clarify the mechanisms of tidally-induced interbasin exchange, a transition experiment from the non-tidal state to the tidal state was conducted. Particularly, we focused on the processes that lead to the bottom steering of the EKC around the North Bank. The conditions on the last day of June of the non-tidal case were taken as the initial conditions for the transition experiment. Then, the tidal forcing was activated, and the model was executed for another 65 days (see Chapter 2 Models and Data Description). Wind and heat fluxes were kept constant as those of June during the experiment. By doing this, the transition experiment would reveal the mechanisms by which tidal forcing produces the EKC's bottom steering and shifts its pathway.

Transport through the two straits is both Pacific-ward initially with approximately +3 Sv according to the June state of the non-tidal case. After accounting for tidal forcing on Day 0, the transport through the northern and southern straits varied until Day 30 and reached an almost steady state thereafter (Fig. 3.6**a**). We may divide the period of the transition into two stages on Day 14. The period between Day 0 and Day 14 represents an initial impact by imposing the tidal forcing. In the northern strait, the Okhotsk-ward inflow (with a negative sign) increases up to Day 8 but decreases afterward until Day 14, when the transport via the northern strait exhibits 0 Sv. From Day 14 to Day 26, transport through the northern strait increases again and finally achieves a steady-state with -2.8 Sv. The transport through the southern strait behaves similarly, displaying a two-stage development. These periods will hereinafter be referred to as "transition stage 1" and "transition stage 2", respectively.

Transition stage 1 is characterized by the generation of seamount trapped waves (Supplementary Movie 1) and tidally rectified circulation around islands and seamounts (Figs. 3.6**b-e** and Supplementary Movie 2). For example, a bi-directional flow occurs in both the northern and southern straits (Fig. 3.6**b**). However, ψ displays a large positive value encompassing the MIC which still forces the EKC to bypass these straits. This suggests that during stage 1, the tidal rectification due to seamount trapped waves is the main factor that drives the development of transport through straits, as discussed in Nakamura *et al*. (2000) (see Supplementary Movie 2). In the upstream surrounding the North Bank, an anticyclonic circulation due to tidal rectification forms on Day 4. However, it does not yet alter the EKC path. During transition stage 2, the EKC starts bending on Day 14 immediately downstream of the North Bank (Fig. 3.6**c** and Supplementary Movie 2). As the EKC bends and collides with the northern part of the MIC, the Okhotsk-ward throughflow becomes predominant in the northern strait. By Day 26, the EKC approaches the MIC steered by relatively shallow bathymetric contours (Fig. 3.6**d**). The EKC then bifurcates (indicated by the red dots in Figs. 3.6**d-e**) when it encounters approximately the 1500 m isobath surrounding the MIC, where the value of ψ decreases significantly compared with the initial value. Because of the formation of the bifurcation point, the Okhotsk-ward throughflow occurs via the northern strait similarly to that illustrated in Fig. 3.1**b**. Interbasin transport tends to become steady after Day 26. The flow pattern of the Okhotsk-Pacific exchange on Day 65 is almost the same as that of the tidal case. This experiment demonstrates that the interaction between tidally-induced circulation and the EKC over the North Bank drives the interbasin exchange in the tidal case.

3.2.3 Tidal-period-mean PV budget of the EKC over the North Bank

To investigate the dynamic effects of tides on the EKC pathway, we diagnosed the EKC via the barotropic PV:

$$q = \frac{f + [\zeta]}{H}, \tag{3.2}$$

where f is the Coriolis parameter, and $[\zeta] = \boldsymbol{k} \cdot \nabla \times [\boldsymbol{u}]$ is the depth-averaged relative vorticity where $\boldsymbol{k}$ and ∇ denote unit vectors in the vertical direction and the horizontal gradient operator $\nabla = (\partial/\partial x, \partial/\partial y)$, respectively. A tidal period mean of the PV equation (derivation please see Appendix 4) yields the following equation (Mertz and Wright, 1992):

$$\underbrace{\frac{\partial \bar{q}}{\partial t}}_{\substack{tendency\ of \\ PV}} + \underbrace{\overline{[\boldsymbol{u}]} \cdot \nabla \bar{q}}_{\substack{tidal\ period \\ mean\ PV\ advection \\ (mean\ PV\ advection)}}$$

$$= -\underbrace{\frac{\overline{J(\chi, H^{-1})}}{H}}_{JEBAR} + \underbrace{\frac{\nabla \times \dfrac{\boldsymbol{\tau}}{\rho_0 H}}{H}}_{\substack{wind\ strss \\ curl}} - \underbrace{\frac{\overline{\nabla \times \dfrac{C_d\,|\boldsymbol{u}|\boldsymbol{u}}{\rho_0 H}}}{H}}_{\substack{bottom \\ stress\ curl}} \tag{3.3}$$

$$- \underbrace{\overline{[\boldsymbol{u}]^t \cdot \nabla q^t}}_{\substack{tidal- \\ rectification}},$$

where $\boldsymbol{\tau}$ is wind stress, ρ_0 is the referential density, C_d is the bottom drag coefficient, and χ is defined by:

$$\chi = \frac{g}{\rho_0} \int_{-h}^{\eta} \rho z \, dz,$$

where ρ is density and g is gravity acceleration. $\bar{\blacksquare}$ and $\blacksquare^t$ represent the mean and tidal component as a function of the diurnal tide period, and J denotes the Jacobian of given variables. The first term on the right-hand-side of equation (3.3) is the joint-effect-of-baroclinicity-and-relief (JEBAR). This represents the effects of baroclinicity on bottom pressure across the topography, which causes torque on the water column (Mertz and Wright, 1992; Yeager, 2015). Further, in equation (3.3), the original PV advection term $\overline{[\boldsymbol{u}] \cdot \nabla q}$ is decomposed as follows:

$$\overline{[\boldsymbol{u}] \cdot \nabla q} \approx \overline{[\boldsymbol{u}]} \cdot \nabla \bar{q} + \overline{[\boldsymbol{u}]^t \cdot \nabla q^t}, \tag{3.4}$$

where $-\overline{[\boldsymbol{u}]^t \cdot \nabla q^t}$ on the right-hand-side of equation (3.3) represents PV production due to tidal rectification. Note that two baroclinicity terms in equation (3.4) are neglected, which are $\overline{\boldsymbol{u}_c} \cdot \nabla \bar{q}_c + \overline{{\boldsymbol{u}_c}^t \cdot \nabla {q_c}^t}$, where $\blacksquare_c$ denotes the baroclinicity component that for instance, $\boldsymbol{u} = [\boldsymbol{u}] + \boldsymbol{u}_c$. The baroclinicity PV advections are one order smaller than barotropic ones. Given that the wind stress in the transition experiment is constant as a function of time, the tidal effects on the EKC's PV budget can be evaluated by the three other terms in the right-hand-side of equation (3.3).

The tidal-period-mean PV advection $\overline{[\boldsymbol{u}]} \cdot \nabla \bar{q}$ (hereinafter referred to as 'mean PV advection') balances well with the sum of the PV production terms (Fig. 3.7**a)** along Section A to the south of the North Bank, where the EKC starts deflecting westward. The mean PV advection $\overline{[\boldsymbol{u}]} \cdot \nabla \bar{q}$ exhibits almost a constant value ≈-4.2 $\times 10^{-13}$ m^{-1} s^{-2} during transition stage 1, except for a negative peak between Day 2 and Day 6, when the difference with the sum of the PV production terms reaches a maximum. The difference corresponds to the local vorticity production $\partial \bar{q}/\partial t$, which represents the generation of clockwise, tidally-rectified circulation around the North Bank by $-\overline{[\boldsymbol{u}]^t \cdot \nabla q^t}$ and exhibits a conspicuous peak during the same period.

In transition stage 2, the mean PV advection increases from -4.2 $\times 10^{-13}$ m^{-1} s^{-2} to -2.6$\times 10^{-13}$ m^{-1} s^{-2} when the EKC shifts. The tidal rectification and bottom friction terms remain almost constant in the PV budget during transition stage 2. The wind stress term is constant throughout the experiment despite having a high value (2.5$\times 10^{-12}$ m^{-1} s^{-2}). Therefore, the only term that changes with time is the JEBAR, which can balance with changes in mean PV advection.

Maps of the PV budget difference between Day 30 and Day 1, defined by $(PV)_{Day30} - (PV)_{Day1}$, are illustrated in Figs. 3.7**b-e**. Since $\bar{q} \approx f_0/H$, where f_0 is the Coriolis parameter around the North Bank, the difference of the mean PV advection in terms of time is approximated as follows:

$$\Delta_T\left(\overline{[\boldsymbol{u}]} \cdot \nabla\bar{q}\right) \approx \Delta_T\overline{[\boldsymbol{u}]} \cdot \nabla\frac{f_0}{H} , \tag{3.5}$$

where Δ_T is an operator representing the difference between Day 30 and Day 1. According to equation (3.5), the difference in the mean PV advection corresponds to the velocity difference between Day 30 and Day 1, $\Delta_T\overline{[\boldsymbol{u}]}$, across PV (or bathymetric) contours. Since $\Delta_T\left(\overline{[\boldsymbol{u}]} \cdot \nabla\bar{q}\right) > 0$ in Section A, $\Delta_T\overline{[\boldsymbol{u}]}$ takes place in the upslope direction ($\nabla\frac{f_0}{H} > 0$), as seen in the vectors in Fig. 3.7**b**. That is, the positive difference in the mean PV advection around Section A corresponds to an upslope transition of the EKC pathway.

The difference of the mean PV advection around the North Bank balances well with the sum of the change of the tidal rectification and JEBAR terms in the right-hand-side of equation (3.3) (Figs. 3.7**b** and 3.7**c**). Particularly, the JEBAR's contribution (Fig.

3.7**e**) is dominant around Section A, which can be expressed as follows:

$$\Delta_T\left(\overline{[\boldsymbol{u}]}\right)_A \cdot \nabla\frac{f_0}{H} \approx -\left(\frac{\overline{J(\Delta_T\chi, H^{-1})}}{H}\right)_A, \tag{3.6}$$

where the subscript A denotes the region around Section A, and

$$\Delta_T\chi = \frac{g}{\rho_0}\int_{-h}^{\eta}\Delta_T\rho z\, dz. \tag{3.7}$$

This result indicates that the JEBAR change due to $\Delta_T\chi$, associated with the density change, $\Delta_T\rho$, in a given water column drives the EKC's upslope transition over the North Bank across PV contours. However, the source of the JEBAR change remained to be determined.

3.2.4 Source of JEBAR change for the EKC's path shift

The JEBAR term is incorporated into PV equation (3.3) like a wind stress curl that generates flows across PV contours once a density field is specified (Mertz and Wright, 1992). In the tidal case, JEBAR forces the EKC upslope to relocate and bend it toward the MIC, resulting in interbasin exchange. Here, we identified the impact of tidal forcing that alters the density field, leading to JEBAR changes over the North Bank.

To examine the mechanism of JEBAR increase, we inspected the density structure in Section A1 (Fig. 3.8, right panels), which is 15 km upstream of Section A, and identified an overturning cell on the slope depicted by the vertical velocity. The formation of the overturning cell associated with the tidally-rectified circulation has been widely discussed in previous studies (Haidvogel *et al.*, 1993; Beckmann and Mohn, 2002; White and Mohn, 2004). The overturning cell in Fig. 3.8 is composed of a downwelling on the slope of a seamount and upwelling around the outer rim of the tidally-rectified circulation. Since the overturning redistributes the density field vertically and horizontally, the JEBAR change due to $\Delta_T\chi$ should occur through the density change $\Delta_T\rho$ according to equation (3.7).

Further, we introduced the bottom pressure torque $J(p_b/\rho_0, H)$ to explore the effect of bottom steering on the EKC (Fig. 3.8, left panels), where p_b denotes bottom pressure. p_b is related to χ through $p_b = [p] - \frac{\rho_0\chi}{H}$, where $[p]$ represents depth-averaged pressure (Mertz and Wright, 1992; Yeager, 2015). The relationship between the bottom pressure torque and the overturning cell is illustrated in Fig. 3.8. The overturning cell is generated on the slope along Section A1 as soon as the tidally-rectified circulation forms by Day 4 (Figs. 3.8**a-b**). The bottom pressure torque exhibits a supply of negative vorticity at 1000-2000 m depths around A1, which likely turns the bottom velocity clockwise. This strongly indicates the cross-slope upwelling reinforces the bottom pressure torque by shoaling isopycnals up to ~700 m (Figs. 3.8**c-d**). Concurrently, an along-isobath bottom flow occurs downstream of Section A1 around the North Bank at depths of 1000-1500 m, where the positive bottom pressure torque (on Day 0) is canceled by the negative torque supply until the end of transition stage 2. The bottom steering drives the EKC in an upslope direction and reaches a similar state to that of the tidal case (Fig. 3.4**a**). Since the density change associated with the overturning cell, which is generated by the tidal rectification, produces the JEBAR's change for the transition of the EKC, we refer to this process as a "tidally driven JEBAR mechanism."

3.2.5 Tidally-modified EKC drives the interbasin exchange

Finally, Figure 3.9 summarizes our overarching findings. In the absence of tidal forcing, the EKC tends to bypass the deep straits and does not induce interbasin exchange. Once the tidal forcing is incorporated, however, the EKC is forced to bend westward after passing the North Bank, and approaches the MIC along with the streamfunction contour ψ_1 as depicted in Fig. 3.9**a**. Afterward, the bifurcation point on ψ_1 occurs around the MIC and the EKC branches northward and southward (Fig. 3.9**a**). The northern branch of the EKC passes through the northern strait Okhotsk-ward and drives the interbasin transport. Upstream of the MIC, the westward deflection of the EKC occurs as a result of steering by the topography of the North Bank when the tidal forcing is imposed (Fig. 3.9**b**). The cross-slope overturning cell in response to the tidally-rectified circulation raises the bottom pressure torque via shoaling of the isopycnals at depth. Increases in the bottom pressure intensified the bottom velocity along isobaths and relocated the EKC pathway across the PV contours by the JEBAR term.

High-resolution simulations typically improve the representation of the flow through straits of WBCs, as described by Metzger and Hurlburt (2001). Concretely, the authors found that the existence of an underwater bank in the Luzon Strait blocks the intrusion of the Kuroshio as the model resolution increased, which is consistent with the observations. This phenomenon was defined as the “blocking effect” (Metzger and Hurlburt, 2001) and resembles our non-tidal case. However, as discussed in this study, improving the model resolution does not necessarily reproduce the interbasin exchange accurately as shown in the non-tidal case because of the non-linearity. Sheremet (2001) evaluated whether a WBC leaps across a strait caused by the current's inertia, overcoming the westward bending due to planetary Rossby waves. In linear models, planetary Rossby waves enforce the EKC deflecting to the MIC and drive the interbasin exchange (Kida and Qiu, 2013). In high-resolution models, however, inertia of WBCs tends to dominate over the Rossby wave dynamics and thus the interbasin exchange is blocked as shown in the non-tidal case. Clearly, a better understanding of the physical processes that drive the WBCs is necessary as the model resolution increases.

Our study proposes a novel mechanism for the interaction between tidally-rectified circulation and the boundary current through JEBAR. We also demonstrated that the interaction between boundary currents and tides, which is usually lacking in modeling studies, is key to improve high-resolution OGCM performance.

3.3 Discussion: Influences of tidally enhanced vertical mixing on the interbasin exhange

Our study elucidated the impact of tidal forcing on the relocation of the EKC pathway due to the changes in JEBAR, which consequently leads to the partial intrusion of the EKC into the Sea of Okhotsk. However, the diurnal tides not only generate rectified circulation but also cause strong vertical mixing along the Kuril Islands by breaking of internal tides (Nakamura *et al.*, 2000; Tanaka *et al.*, 2014). Although the impact of tidally-induced vertical mixing along the Kuril Islands on the North Pacific's thermohaline circulation was suggested (Kawasaki and Hasumi, 2010; Yagi *et al.*, 2014), its influence on the Okhotsk-Pacific exchange system was seldom mentioned.

Vertical mixing observed along the Kuril Islands is as high as 25 $cm^2\ s^{-1}$ (Tanaka, Hibiya and Niwa, 2007), which is two orders of magnitude stronger than that in the ocean interior (Tanaka, Hibiya and Niwa, 2007). In the COCO, vertical mixing was parameterized as the vertical diffusivity coefficients evaluated by the turbulent closure scheme (Noh and Jin Kim, 1999). The vertical diffusivity coefficients around the islands were approximately 23.9 $cm^2\ s^{-1}$ and 13.6 $cm^2\ s^{-1}$ in the tidal and non-tidal cases, respectively (see Fig. 3.10**a-b**). To evaluate the impacts of vertical mixing with no tidal oscillations on the Okhotsk-Pacific exchange system, we conducted an experiment in which the vertical diffusivity coefficients extracted from the tidal case were substituted with those of the non-tidal case (Fig. 3.10**c**; see Chapter 2 Models and Data Description). This case is henceforth referred to as the "non-tidal-TM case," where TM denotes Tidal Mixing.

We found that the interbasin exchange in the non-tidal-TM case exhibited the most unrealistic throughflow transport estimates of +0.9 Sv and +0.8 Sv at the northern and southern straits, respectively (Figs. 3.11**a-b**). This scenario exhibited an intense clockwise circulation surrounding the MIC (Fig. 3.12), which was similar to the results of the non-tidal case (Fig. 3.4**e**). Therefore, enhanced vertical mixing does not drive the intrusion of the EKC into the Sea of Okhotsk. That is, vertical mixing is not a factor that causes interbasin exchange in the Tidal case.

For further sensitivity testing, an experiment in which the vertical diffusivity coefficient was set to zero was conducted with the tidal-case configuration (henceforth referred to as the "tidal-NoM" case, where "NoM" means no-mixing; see section 4.3 Methods). The interbasin exchange in the tidal-NoM case was the largest among all cases (Figs. 3.11**a**-**b**). The EKC exhibits a sharp deflection around the North Bank and bifurcates at the MIC's northern corner by following the streamfunction contour $\psi = -5.81 \times 10^6$ m^3 s^{-1}, resulting in a strong Okhotsk-ward throughflow transport (Fig. 3.11**c**).

According to the tidally driven JEBAR mechanism, the northward relocation of the EKC toward the MIC is expressed by the PV supply via JEBAR on the North Bank's eastern slope. The tidal-NoM case shows a larger JEBAR value around Section A than that of the tidal case (Fig. 3.11**d**). The vertical profiles of density and along-slope velocity on Section A indicate that the EKC in the tidal-NoM case locates further upslope compared with that of the tidal case (Fig. 3.10**d**). The effects of the tidally-rectified circulation on the EKC are enhanced in the tidal-NoM case compared with the tidal case by strengthening the tidally driven JEBAR mechanism. Considering the results of the sensitivity experiments, we concluded that tidally-induced vertical mixing tends to reduce the interbasin transport between the Sea of Okhotsk and the North Pacific.

Vertical mixing is often incorporated in OGCMs through parameterizations over rough topography to estimate the global distribution of tidal energy available for turbulent mixing (Jayne and Laurent, 2001; Laurent, Simmons and Jayne, 2002). In contrast, the dynamic effects of tides such as the interaction between western boundary currents and tidal motions are often overlooked in basin-wide or global-scale modeling. However, as discussed in the introduction, high-resolution OGCMs are uncovering inconspicuous problems inherent to relatively low-resolution models due to improvements in physics modeling. For example, recent study point out that the 18.6 years lunar cycle highly-correlated with the NPIW formation by observations and suggests it is due to the interbasin exchange governed by tidally driven JEBAR mechanism (Mensah and Ohshima, 2021). It implies that the inclusive of tidal oscillation in future high-resolutions OGCMs is vital for even the large time and spatial phenomena.

Comprehensively, our results suggest that the tidal forcing and the resulting tidally driven JEBAR mechanism are a missing piece for high-resolution OGCMs in which strong boundary currents and topographic features are accurately characterized in high-latitude areas. The tidally driven JEBAR mechanism may also apply to various regions where both boundary currents and intensive diurnal tides coexist. For example, the Aleutian Arc and the Antarctic continental shelves are candidates; in the former, the Alaskan Stream controls the interbasin exchange between the Bering Sea and the North Pacific (Maslowski *et al.*, 2014; Prants *et al.*, 2018), whereas in the latter case, the Antarctic Slope Current regulates the heat transport to the ice shelf (Flexas *et al.*, 2015;

Thompson *et al.*, 2018).

This page intentionally left blank

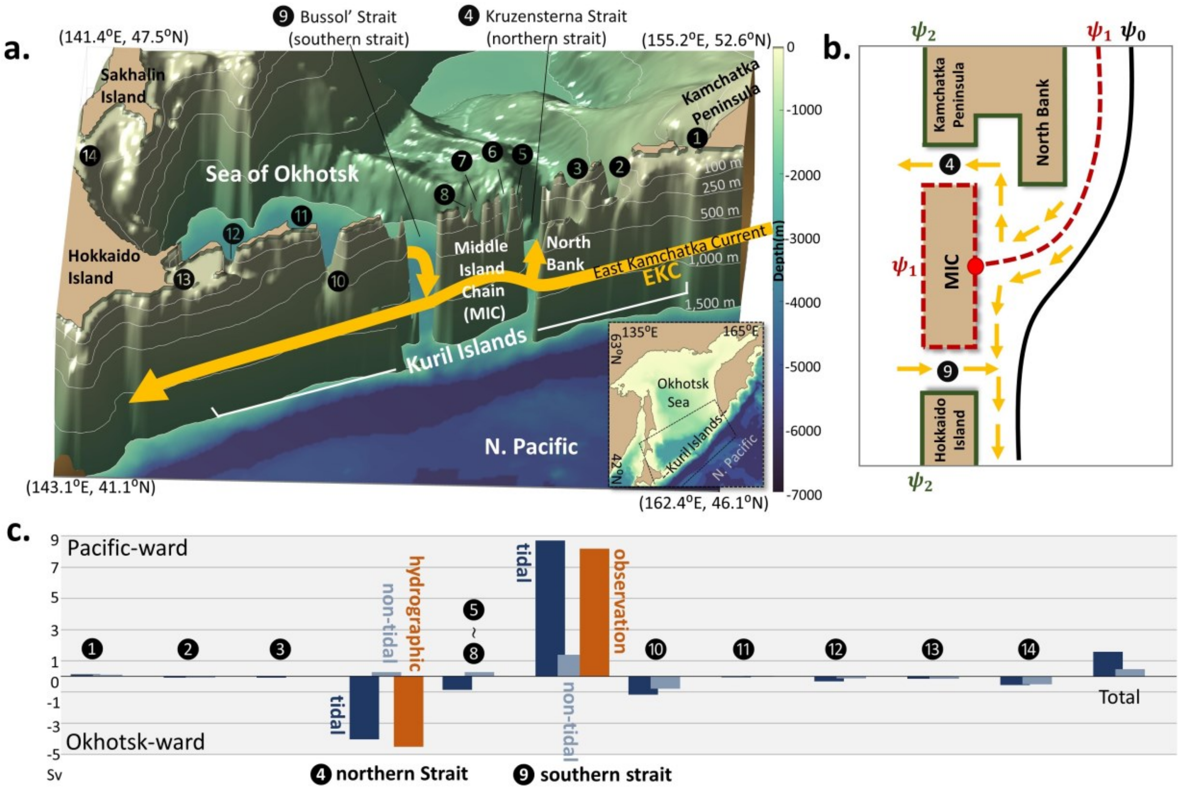

Figure 3.1 Okhotsk-Pacific Exchange System through different straits. a Topographic features of the Kuril Islands in the COCO model, which is adapted from the Japan Oceanographic Data Center (JODC) and modified by Ono *et al*. (2006) and Matsuda *et al*. (2015) (see Chapter 2 Models and Data Description). The shaded areas represent the depth of the ocean and contours denote the iso-depths of 100, 250, 500, 1000, and 1500 m. To illustrate the details of the strait topographic features, the bird's-eye view plot extends only to a depth of 1500 m, whereas the rest of the study area is represented as shades on the floor. The arrows represent the East Kamchatka Current (EKC), the western boundary current, and the major exchange currents through the Kruzensterna and Bussol' Straits. The circled numbers above straits denote the straits from north to south as follows: 1. 1st Kuril Strait, 2. Onekotan Strait, 3. Shiashikotan Strait, 4. Kruzensterna Strait (northern strait), 5. Matua Strait, 6. Rasshua Strait, 7. Ketoy Strait, 8. Simushir Strait, 9. Bussol' Strait (southern strait), 10. Urup Strait, 11. Etrof Strait, 12. Kunashiri Strait, 13. Nemuro Strait and 14. Soya Strait. The abbreviation "N. Pacific" stands for North Pacific. All these strait numbers are used in figures throughout this study. **b** Schematic view of the Okhotsk-Pacific exchange system by streamfunction. The black and army green solid line denotes the streamfunction ψ_0 as the offshore boundary of the EKC and the streamfunction ψ_2 as the boundary around the Kamchatka Peninsula, as well as Hokkaido Island, respectively. The red dashed line represents the streamfunction

ψ_1 as the core axes of the EKC and the streamfunction around the MIC. The red circle indicates the bifurcation point of the EKC on the MIC. The EKC flows from the North Bank to the MIC by following the streamfunction contour ψ_1 as the main axes with ψ_0 as the offshore boundary of the EKC. When the EKC approaches the MIC, it collides on the streamfunction contour surrounding the MIC and forms the bifurcation point. The transport at the northern and southern straits are thus $\psi_2 - \psi_1$ and $\psi_1 - \psi_2$, respectively. **c** Annual-averaged volume transport through each strait, where the numbers in the horizontal axis correspond to the numbers in panel **a**. Positive values denote a Pacific-ward flow, whereas negative values are Okhotsk-ward. The tidal case, the non-tidal case, and observation data (Katsumata *et al.*, 2004; Katsumata and Yasuda, 2010; Ohshima *et al.*, 2010) are indicated in navy-blue, grey-blue, and dark-orange bars, respectively.

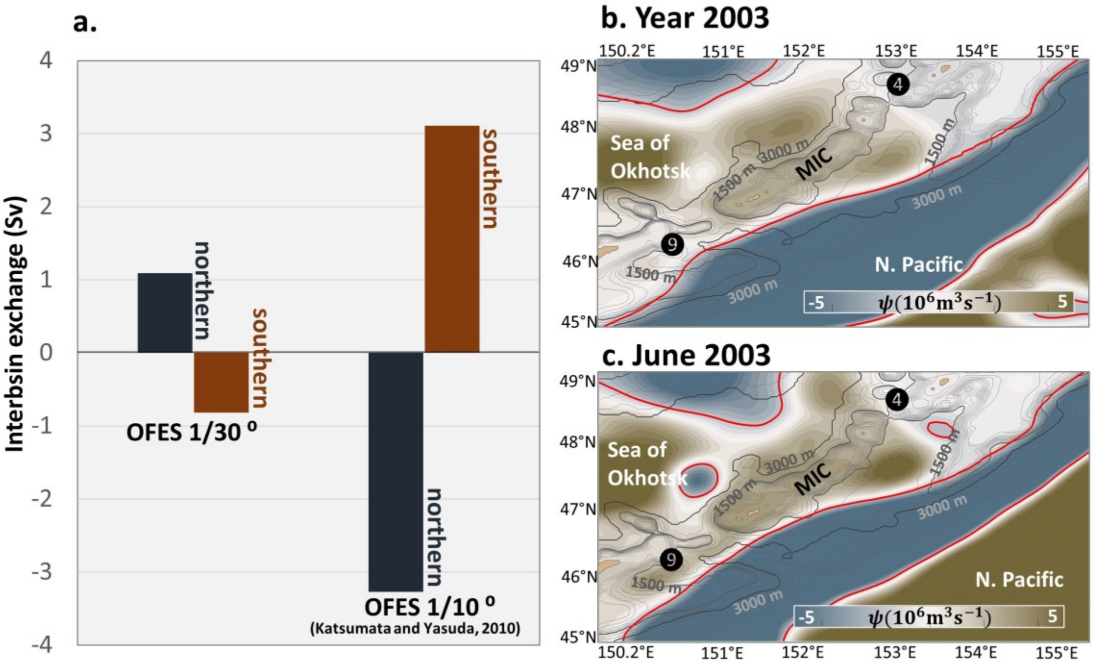

Figure 3.2 Results of the OFES 1/30° model. a. Annually-averaged volume transport in 2003 through two straits of the OFES 1/30° model (Sasaki and Klein, 2012; Sasaki *et al.*, 2014) and OFES 1/10° model (Katsumata and Yasuda, 2010). The deep-blue and brown boxes denote the annual-averaged transport through the Kruzensterna (northern) and Bussol' (southern) Straits, respectively. The difference in exchange transport through both straits in the OFES 1/30° model is approximately three times smaller than that of the OFES 1/10° model. **b** Plan view of the annually-averaged streamfunction of the year 2003. **c** Plan view of the monthly-averaged streamfunction of June 2003. The grey contours denote the topography, where the contour interval is 150 m till 1500 m and continuously with 500 m intervals till 6000 m. The thick grey contours denote the 1500 m and 3000 m depth, respectively. The EKC in the OFES 1/30° model overleaps the MIC both in annually averaged and monthly-averaged instances as in the non-tidal case (Fig. 3.4**f**). The red contour is the streamfunction contour where $\psi = -1.5 \times 10^6$ m^3 s^{-1}. The streamfunction indicates that the transport crosses the MIC through its straits. The topography data is obtained from the OFES 1/30° model (Sasaki and Klein, 2012; Sasaki *et al.*, 2014) (see Chapter 2 Models and Data Description).

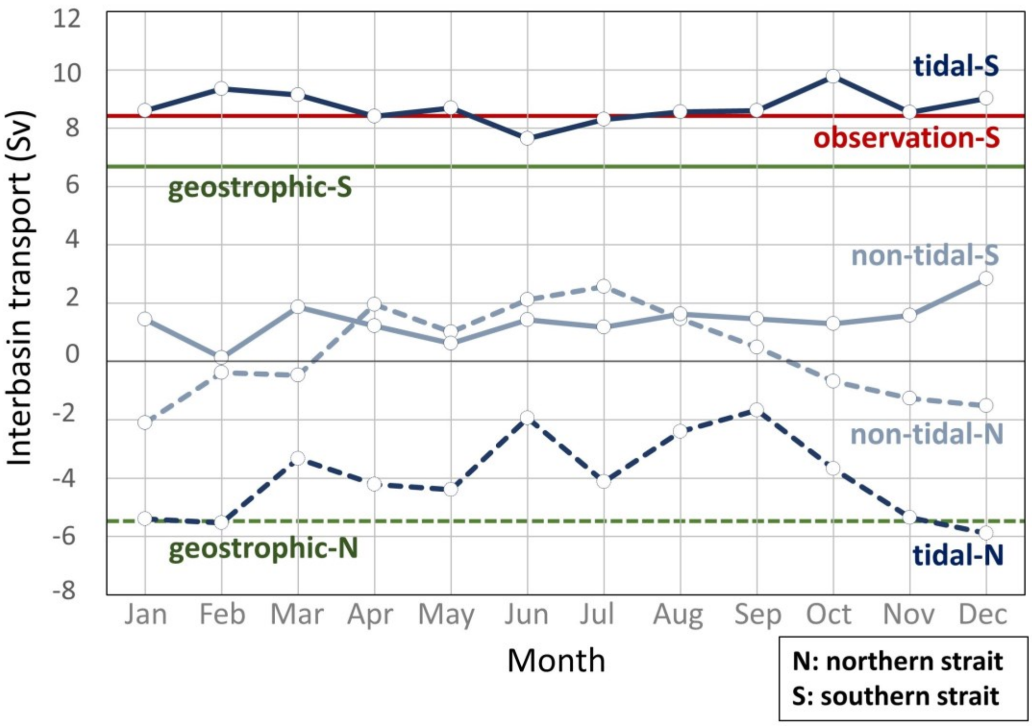

Figure 3.3 Transport through the northern and southern straits in the tidal and non-tidal cases. Seasonal volume transport through the northern strait (dashed-line, 153°E~154°E) and the southern strait (solid-line, 150.4°E~151.8°E) of the non-tidal case (grey-blue line) and the tidal case (navy-blue line). Positive values flow in a Pacific-ward direction. The red line denotes the observed transport of the southern strait (Katsumata *et al.*, 2004) in the summer and the green lines are the annually-averaged hydrographic transport value of the northern strait (dashed line) and southern strait (solid line) (Katsumata and Yasuda, 2010). The abbreviations "N" and "S" correspond to the northern and the southern straits, respectively.

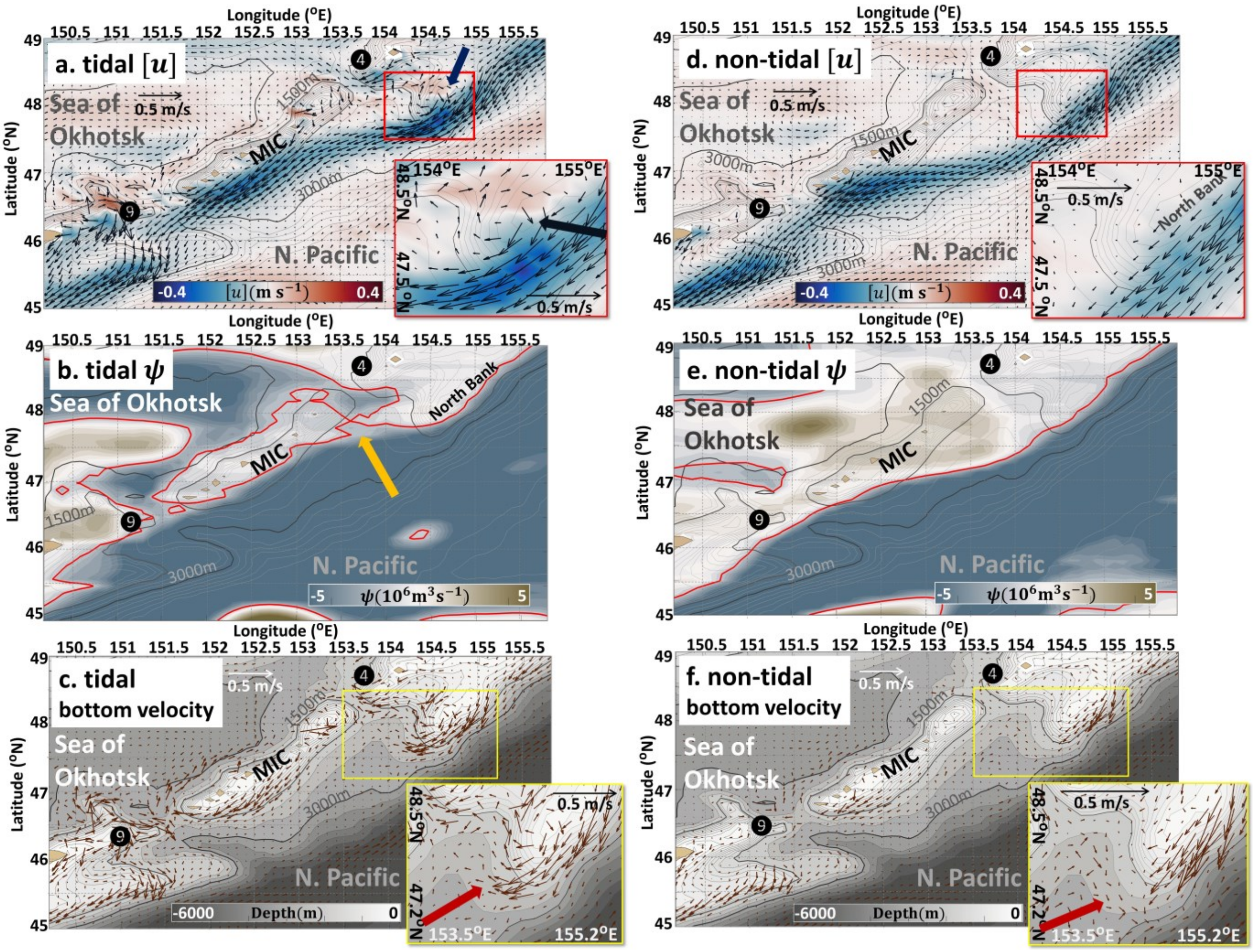

Figure 3.4 Non-tidal and tidal cases in June. Monthly-mean depth-averaged velocity [$\boldsymbol{u}$], the streamfunction, and the bottom velocity of the bottom friction layer of the tidal and the non-tidal cases in June. **a** Flow pattern [$\boldsymbol{u}$] of the tidal case. The grey contours denote the topography, where the contour interval is 150 m till 1500 m and continuously with 500 m intervals till 6000 m. The thick black contours denote the 1500 m and 3000 m depth, respectively. The circled numbers 4 and 9 indicate the northern (Kruzensterna) and southern (Bussol') straits, respectively. The abbreviation MIC stands for Middle Island Chain. The topographic contour and circled numbers described herein will be used in the following figures of this study. The shade denotes the velocity of the zonal component of [$\boldsymbol{u}$], in which red shade represents eastward and blue shade represents westward flow. The blue arrows indicate the tidally-rectified circulation. **b** The streamfunction ψ of the tidal case. The red contour is the streamfunction contour where $\psi = -1.5 \times 10^6$ m^3 s^{-1}. The streamfunction contour here represents ψ_1 in Fig. 3.1**b**. The yellow arrow indicates the bifurcation point. **c** Bottom velocity of the tidal case. The shade represents the bathymetry. **d** Same as **a** but for the non-tidal case. **e** Same as **b** but

for the non-tidal case. **f** Same as **c** but for the non-tidal case. Note that the arrow scale of small window in panel **f** is slightly larger than that in panel **c** for vector clearness. The red arrows indicate the area in which the bottom velocity is reversed.

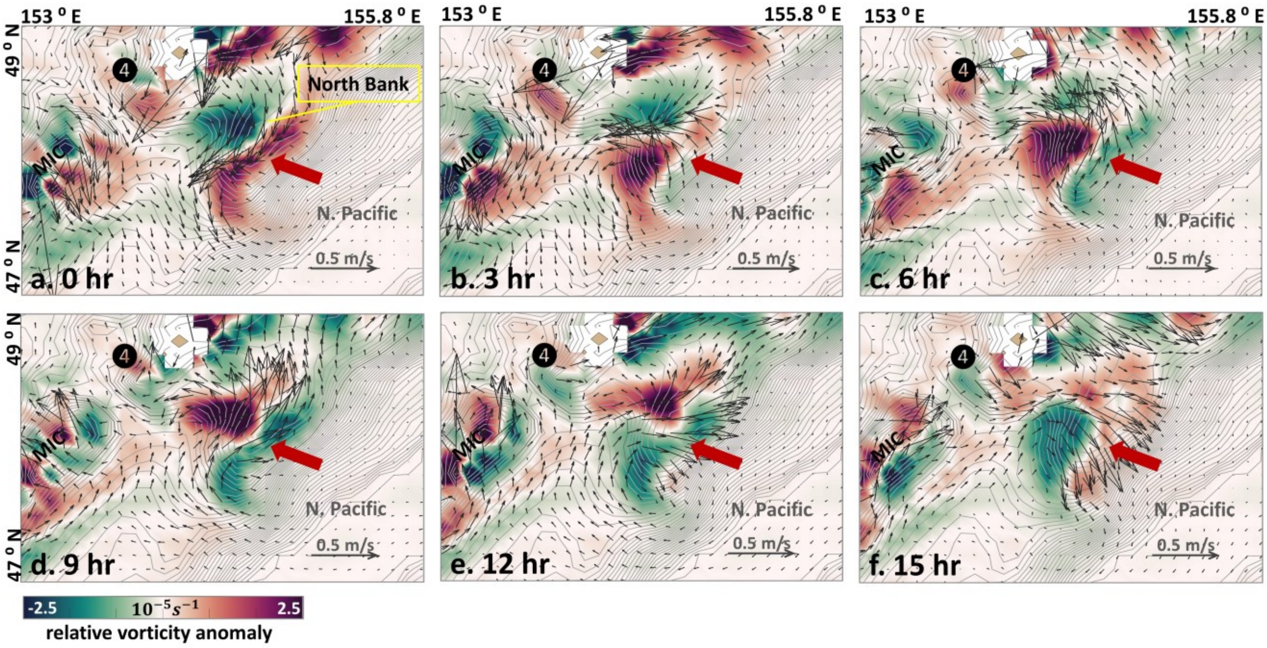

Figure 3.5 Propagation of seamount trapped waves. Snapshot of the plan view of the vertical averaged velocity anomaly (vector) and relative vorticity ($[\zeta] = \boldsymbol{k} \cdot \nabla \times [\boldsymbol{u}]$) anomaly (shade) of the tidal case in June at 3-hour time steps. The red arrows denote the propagation of the seamount trapped wave, which covers the entire range of the EKC. **a**. 0 hr. **b**. 3 hr. **c**. 6 hr. **d**. 9 hr. **e**. 12 hr. **f**. 15 hr. The seamount trapped wave propagates clockwise around the North Bank.

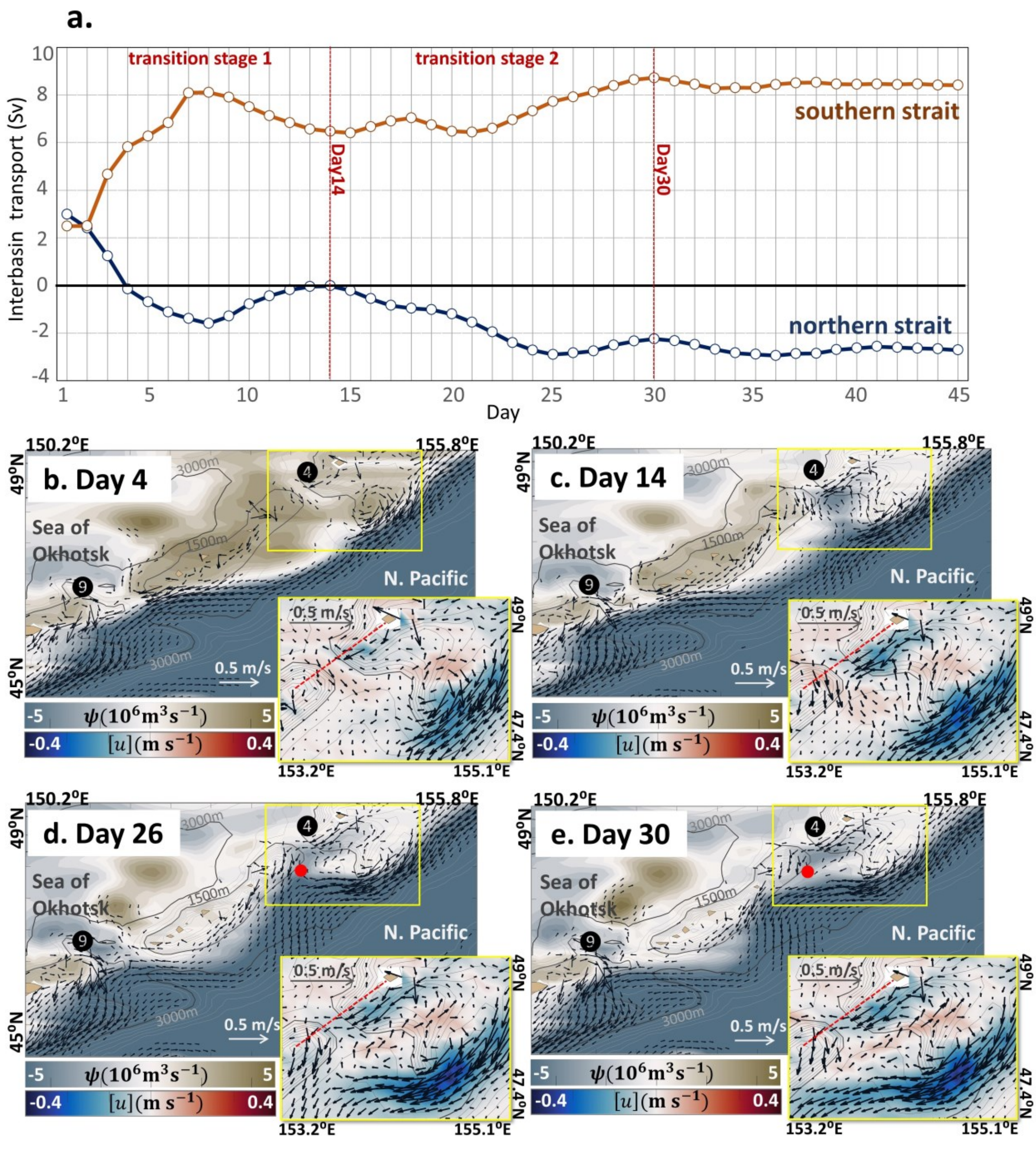

Figure 3.6 Exchange transport and evolution of the EKC during the transition experiment. **a** Evolution of volume transport through the northern strait (blue line) and the southern strait (orange line) from Day 1 to Day 45 during the experimental period. Positive values indicate Pacific-ward flows and negative values are Okhotsk-ward. The transition stage 1 is the period between Day 1 and Day 14, followed by stage 2 before Day 30. **b-e** The flow pattern during the transition experiment. **b** Day 4 state, which

illustrates a bi-directional transport at the northern and southern straits. Vectors denote the depth-averaged velocity field $[\boldsymbol{u}]$, and only the one with speed ($\sqrt{[u]^2 + [v]^2}$) over 0.05 m s^{-1} is shown. The shade denotes the streamfunction ψ. Tidally-rectified flow is also observed over the North Bank. The small panel represents an enlarged view of the $[\boldsymbol{u}]$ field as vectors around the northern strait and the North Bank with the shade as zonal velocity, all vectors are shown. The red dashed line denotes the section where transport was estimated in this study. The grey contours denote the topography, where the contour interval is 150 m till 1500 m and continuously with 500 m intervals till 6000 m. The thick black contours denote the 1500 m and 3000 m depth, respectively. **c** Same as **b** but for Day 14, **d** Day 26, and **e** Day 30. The shifting of the EKC pathway is illustrated in the panels **d** and **e**. The red dots in **d** and **e** denote the bifurcation points.

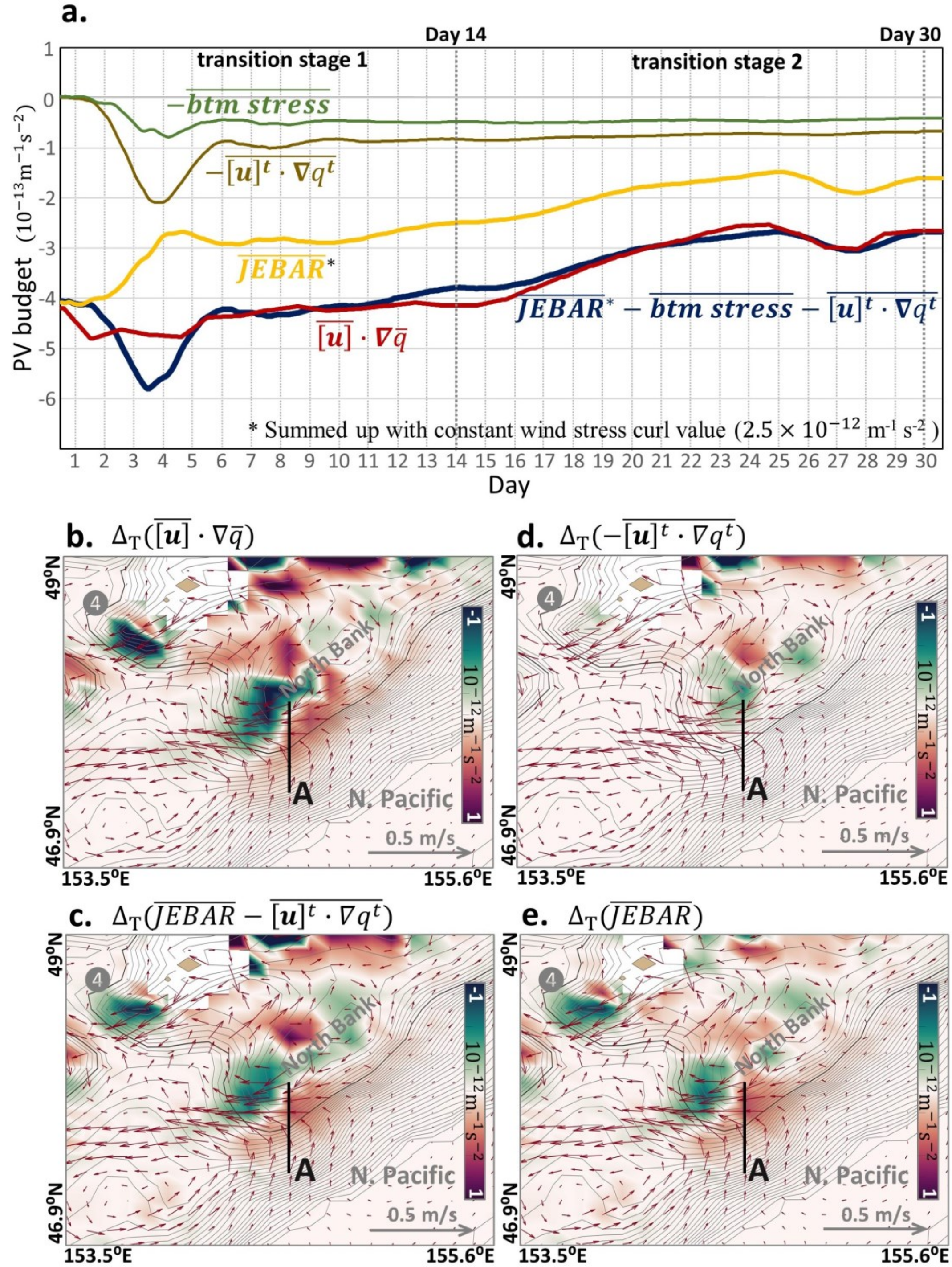

Figure 3.7 Evolution of PV budgets during the transition experiment. a Each term in the PV equation (3) from Day 1 to Day 30 in Section A in the transition experiment, where the EKC alters the pathway during the transition from the non-tidal case to the tidal case. The grass-green line, solid earth-yellow line, yellow line, and navy-blue line denote the

bottom stress curl, tidal-rectification term, JEBAR term (including the constant wind stress curl), and the total of the right-hand side of the equation (3.3) including the constant wind stress curl, respectively. The red line represents the mean PV advection on the left-hand side of the equation (3.3). Vertical thick grey dashed lines indicate the date on Day 14 and Day 30, which are the beginning and end of transition period stage 2. **b-e** Distribution of terms in the PV equation based on the difference between Day 30 and Day 1 (Day 30 – Day 1). The vectors also indicate the differences in depth-averaged velocity between Day 30 and Day 1. The black line denotes Section A. The grey contours denote the topography, where the contour interval is 150 m till 6000 m. The thick dark-grey contours denote the 1500 m depth. **b** Mean PV advection term. **c** Sum of JEBAR and tidal-rectification term. **d** Tidal-rectification term. **e** JEBAR term.

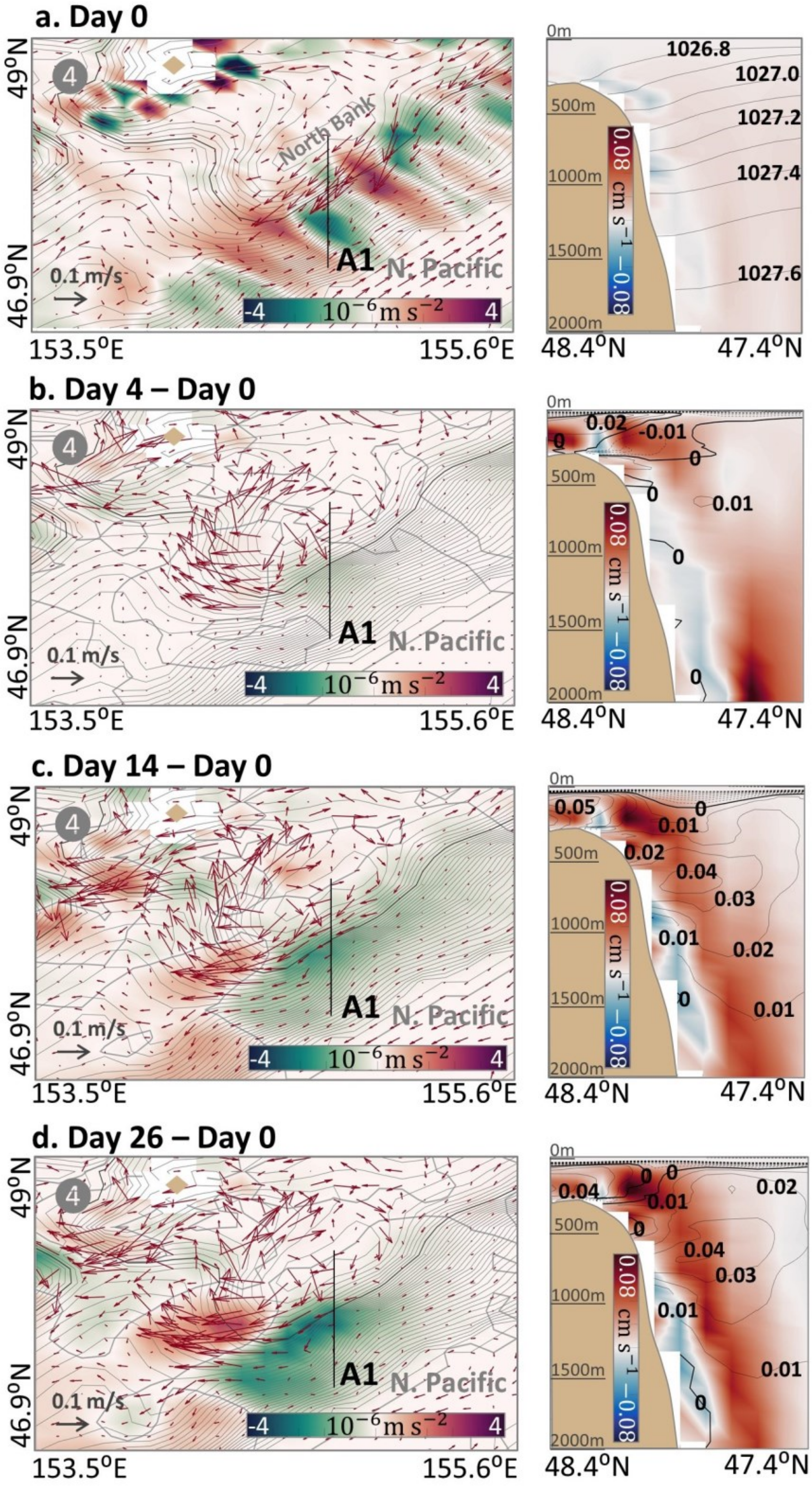

Figure 3.8 Pressure torque generation. Bottom pressure torque (left panel) and the formation of the overturning cell on the North Bank (right panel) during the transition

experiment. **a** Day 0 state. Left panel: Bottom pressure torque (shade) and bottom velocity (vectors). Right panel: Vertical velocity (shade) and density (kg m^{-3}, contours). **b** Difference between Day 4 and Day 0 (Day 4 – Day 0). Left panel: bottom pressure torque differences (shade) and bottom velocity differences (vectors). The thick grey contour represents the division of positive and negative values of the bottom torque differences. Topography contours are as same as Fig. 3.7. Right panel: difference in vertical velocity (shade) and density (kg m^{-3}, contours) in Section A1, shown as a black line in the left panel. Solid (dashed) contours denote the positive (negative) values of density differences from Day 0. **c** Same as **b** but for the difference between Day 14 and Day 0 (Day 14 – Day 0). **d** Same as **b** but for the difference between Day 26 and Day 0 (Day 26 – Day 0).

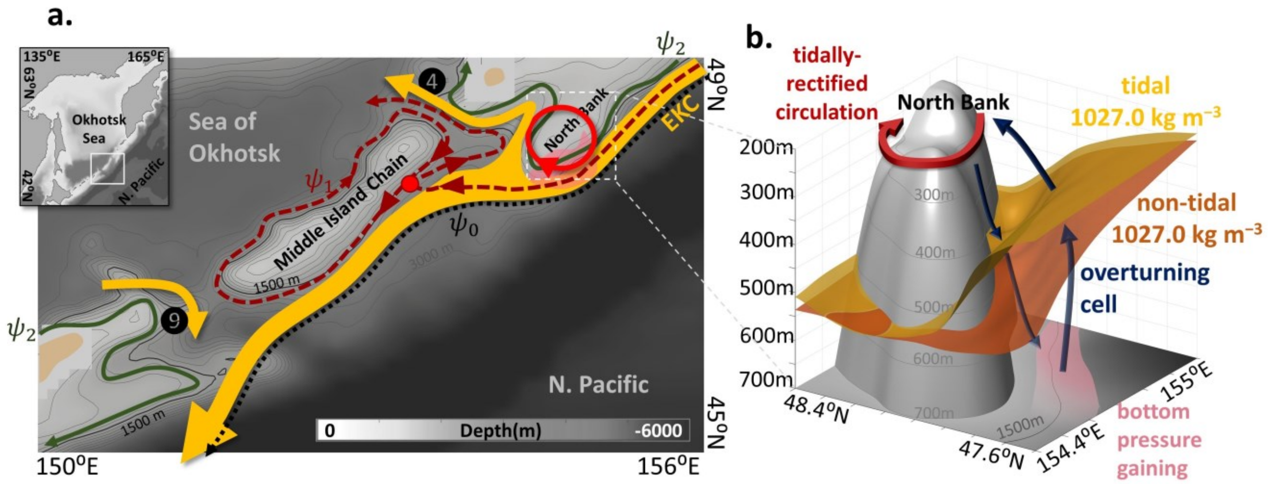

Figure 3.9 Schematic view of the Okhotsk-Pacific exchange system. a Sketch of the Okhotsk-Pacific exchange system incorporating tidal forcing. The underground area represents the topography focused on the MIC area, which is represented by the grey contours (250 m depth intervals reaching 3000 m). The dark-grey contour indicates the 1500 m depth. The dashed black line, dashed red line, and solid army-green line denote the streamfunction contour offshore boundary of the EKC (ψ_0), surrounding the MIC (ψ_1), and surrounding the islands northern/southern than the MIC (ψ_2), respectively. The yellow arrow denotes the EKC pathway with the exchange transport in the tidal case, which follows the streamfunction contour ψ_1 as the core axes. The red dot on the MIC denotes the bifurcation point. The red arrowed circle above the North Bank represents the tidally-rectified circulation caused by the propagation of seamount trapped waves. The transparent pink area is the region where the PV is supplied by the JEBAR along with the formation of tidally-rectified circulation. **b** Generation of the overturning cell and the isopycnal elevation formed through the generation of the tidally-rectified circulation over the North Bank area. The yellow and dark-orange surfaces indicate the 1027.0 kg m^{-3} isopycnal surfaces of the tidal and the non-tidal cases, respectively. The red circle represents the tidally-rectified circulation and the blue arrows denote the overturning cell which is caused by the tidally-rectified circulation.

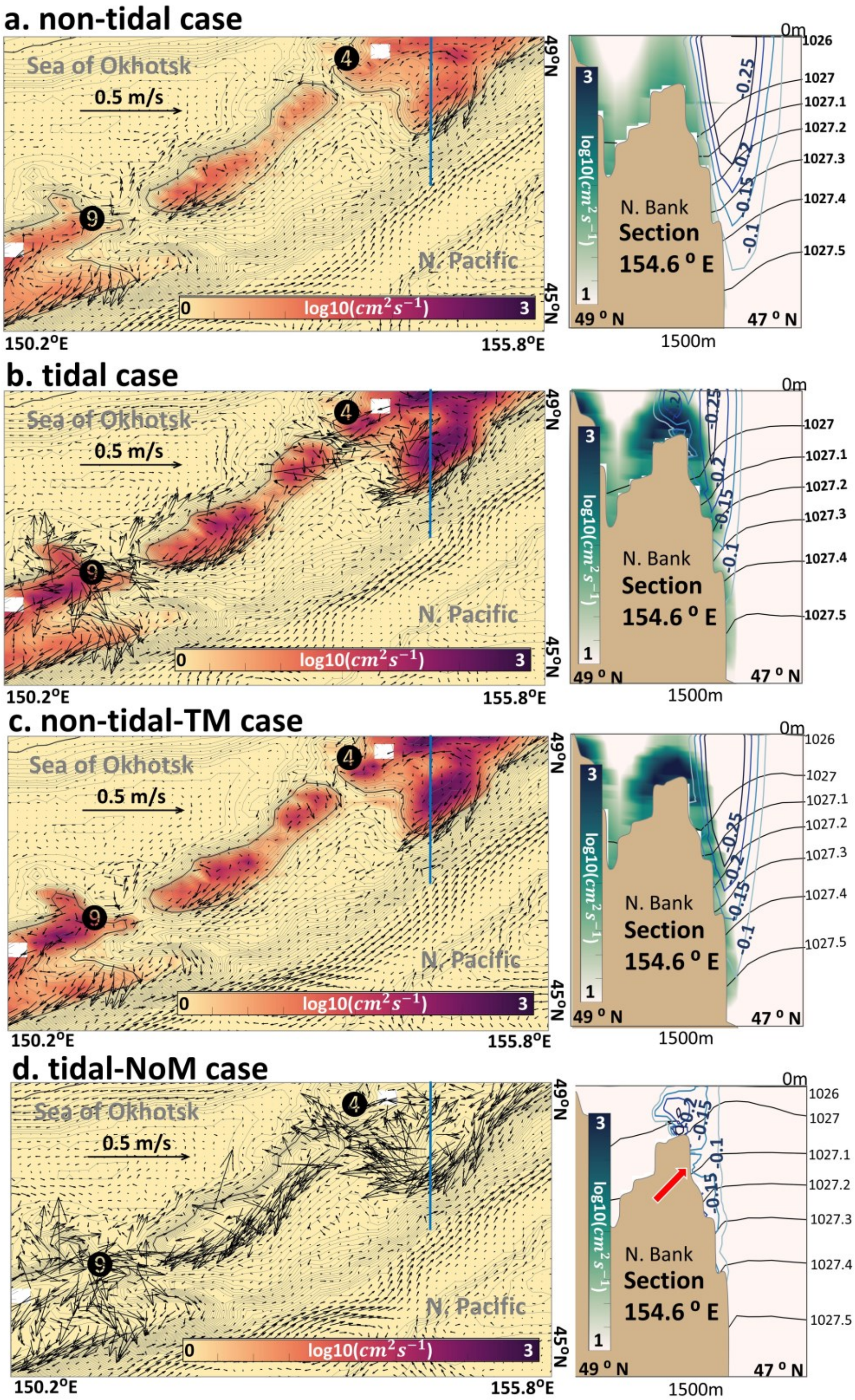

Figure 3.10 Bottom velocity and vertical diffusivity distribution in each case. Left panels: plan view of vertical diffusivity coefficient (shade, log 10 scale) and the bottom velocity of the bottom friction layer (vector) in each case. Right panels: density structure

(black contour), EKC core (blue contour), and the distribution of vertical diffusivity (shade) on the meridional section which extended northward from original Section A (blue line in left panels). **a**. non-tidal case. **b**. tidal case. **c**. non-tidal-TM case. **d**. tidal-NoM case. The red arrow indicates the area where the EKC sticks on the bottom surface without the vertical mixed layer.

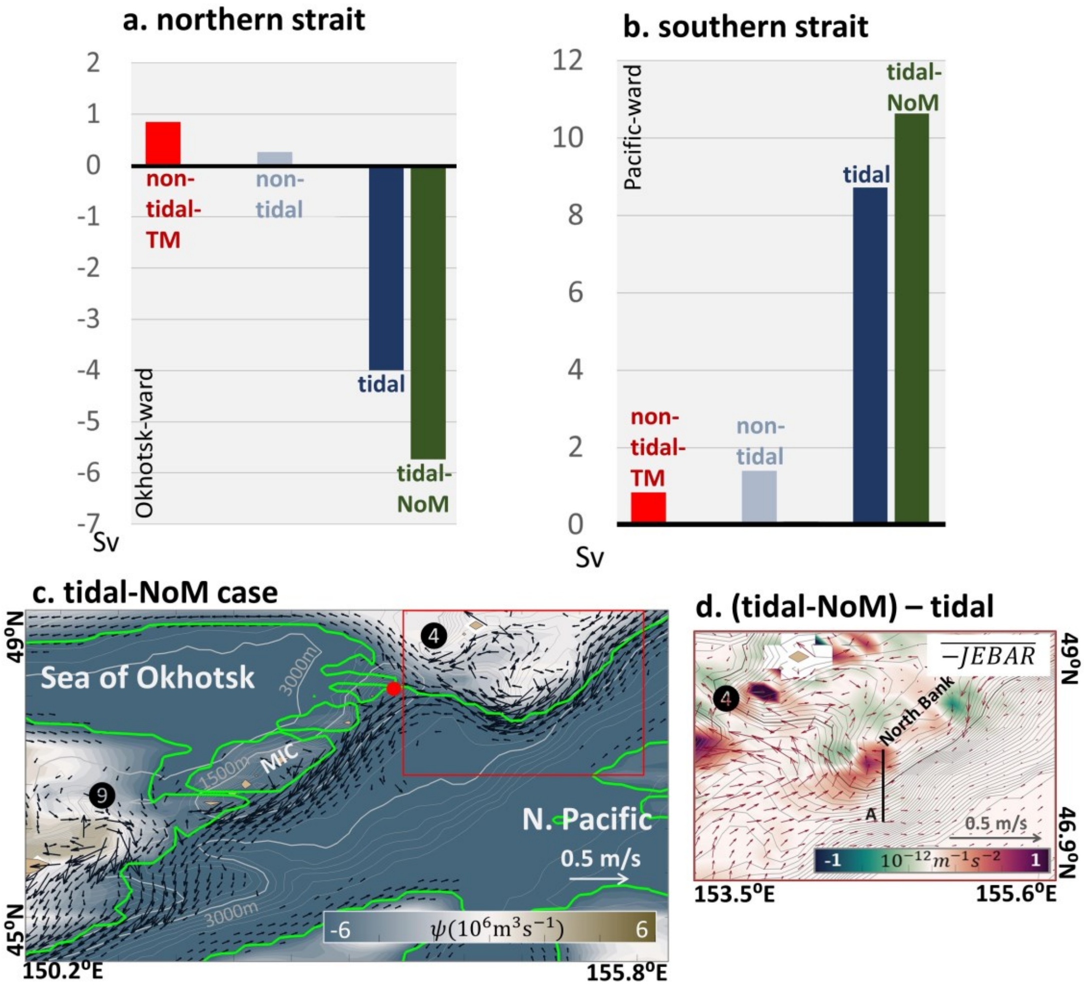

Figure 3.11 TM case and NoM case experiments. a-**b**, Annual volume transport rate of the non-tidal-TM, the non-tidal, the tidal, and the tidal-NoM cases. Panels **a** and **b** are the volume transport via the northern and the southern straits, respectively. Positive values indicate Pacific-ward transport. Red, grey-blue, navy-blue, and army-green bars denote the non-tidal-TM, the non-tidal, the tidal, and the tidal-NoM cases, respectively. **c** Plan view of the depth-averaged velocity (vector), in which only the one with speed ($\sqrt{[u]^2 + [v]^2}$) over 0.05 m s^{-1} is shown, and the streamfunction (shade) of the tidal-NoM case. The green contour denotes the streamfunction contour $\psi = -5.81 \times 10^6$ m^3 s^{-1}. The red dot represents the bifurcation point. Topography contours are as same as Fig. 3.4 but note that the scale of shading is different from Figs. 3.4 and 3.6. **d** Differences in JEBAR (shade) and depth-averaged velocity (vector) between the tidal-NoM and the tidal cases. The black line denotes Section A. The JEBAR is higher in the tidal-NoM case, which corresponds with the EKC pathway adjustment. The EKC shifts to the relatively shallower contour of the location where the positive value occurred.

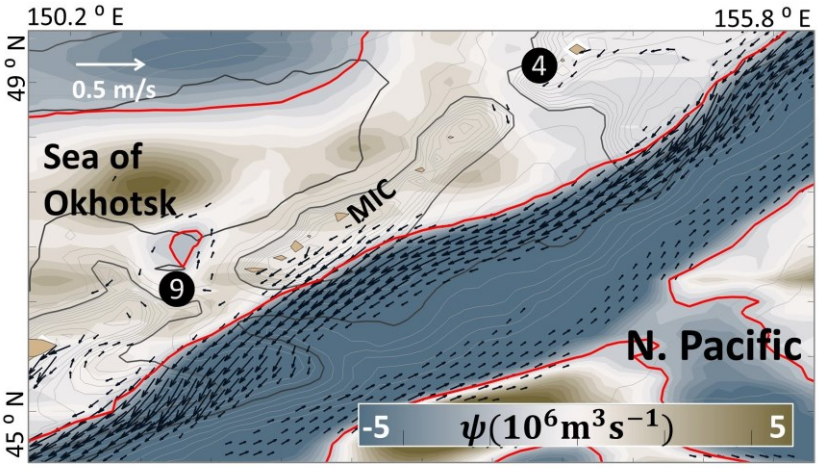

Figure 3.12 Non-tidal-TM case. Depth-averaged velocity (vectors in background figure) and streamfunction (shade in background figure) of the non-tidal-TM case. Only the vector which its' speed ($\sqrt{[u]^2 + [v]^2}$) over 0.05 m s^{-1} is shown. The grey contours denote the topography, where the contour interval is 150 m till 1500 m and continuously with 500 m intervals till 6000 m. The thick grey contours denote the 1500 m and 3000 m depth, respectively. The red contour is the streamfunction contour $\psi = -1.5 \times 10^6$ m^3 s^{-1}. The streamfunction shows that the non-tidal-TM case has a similar structure to the non-tidal case.

Chapter 4

Discussion: Possible tidal impacts on the Antarctic Slope Current

In the previous chapter, we identified the tidally-driven JEBAR mechanism, which enhances the Okhotsk-Pacific interbasin exchange by modifying the western boundary current (WBC) on the subarctic Pacific. We further investigate Antarctic Slope Current (ASC) off the Totten Ice Shelf (TIS) in the southern hemisphere to discuss whether tide affects the shelf-slope exchange.

4.1 Antarctic Slope Current modulates the heat intrusion towards the Totten Ice Shelf

The TIS (Fig. 4.1**a**), the main ice shelf on East Antarctica, suffers rapid basal melting in recent years caused by the modified Circumpolar Deep Water (mCDW) intrusion across the shelf break (Greene *et al.*, 2017; Mohajerani, Velicogna and Rignot, 2018; Silvano *et al.*, 2019). The strong Easterlies circulate around the Antarctic coast and drive a narrow westward boundary current, ASC, ringing the Antarctic continental shelf. The on-shore Ekman transport and the off-shore one, which are caused by the Easterlies along the continental shelf and the Westerlies in the Southern Ocean, respectively, upwell the underneath warm Circumpolar Deep Water (CDW) into the intermediate layer (Thompson *et al.*, 2018). The upwelled CDW then transforms into the mCDW and forms Antarctic Slope Front (ASF) (Kida, 2011; Whitworth *et al.*, 2013; Flexas *et al.*, 2015; Martin *et al.*, 2017). The mCDW is thus the heat source that drives basal melting of ice shelves across the shelf break (Fig. 4.1**b**) (Pritchard *et al.*, 2012; Rintoul *et al.*, 2016; Nakayama *et al.*, 2019; Silvano *et al.*, 2019). Previous studies suggest that the ASC regulates the mCDW intrusion toward the ice shelves (Nakayama *et al.*, 2021; Thompson and Heywood, 2008; Thompson *et al.*, 2018). For instance, Nakayama *et al.* (2021)

pointed out that the on-shore intrusion is enhanced when the ASC weakens off the TIS by high-resolution regional model simulation. However, the mechanism modulating mCDW intrusion by the ASC is still unclear.

Although sufficient observation is lacking, there is one record of long-term observation mooring on the Antarctic Slope off the TIS that captured the tidal activities on the ASC. Peña-Molino, McCartney and Rintoul (2016) collected the velocity and hydrographic data from the mooring station (Fig. 4.1**a**) located on the Antarctic continental shelf from December 2009 to January 2012 for the ASC transport estimation (Peña-Molino *et al.*, 2016). Significant tidal oscillations are then recorded along with the continental shelf. It confirms that the ASC pathway off the TIS, which flows along with the potential vorticity (PV) contours on the continental edge, is bathed with strong tidal waves propagation (Peña-Molino *et al.*, 2016). Previous studies suggest that eddy activities and tidal rectification are the potential contributors to cross-slope heat transport (Stewart, Klocker and Menemenlis, 2018, 2019). Since the tidal oscillation was not incorporated in the Nakayama *et al*. (2021)'s study, we thus further add the tidal boundary on the model to investigate the tidal impacts on the ASC.

4.2 Tide warms the mCDW upper boundary on the ASC

For a better representation of high-frequency eddy activities as shown by mooring data provided by Peña-Molino *et al*. (2016), we increased the time-resolution of the Nakayama *et al*. (2021)'s model by adding 1 day averaged open boundary condition and 1-hour intervals atmospheric forcing from January 2009 to January 2012 (hereafter refers to nontidal-TIS case; see Chapter 2 Methods and Data Description). The tidal forcing is obtained by adding the tidal oscillation boundary and hereafter refers to the tidal-TIS case.

According to the meridional section of ship-board temperature investigation along with the section P on longitude 112.9°E shown in Fig. 4.1**a**, where the mooring stations were located, Peña-Molino *et al*. (2016)'s study provides a typical temperature structure. The diverging Ekman transport (green dash arrows) upwells the underneath CDW, edged with 1027.7 kg m^{-3} and 1027.8 kg m^{-3} isopycnal layers as upper and lower boundaries, respectively. The tidal-TIS (Fig. 4.2**a**) and nontidal-TIS (Fig.4.2**b**) cases both capture the overall monthly-averaged temperature structure of section P, corresponding to Peña-Molino *et al*. (2016)'s investigation (Fig. 2.4 for salinity profile and Fig. 4.1**b** for temperature profile). Difference between the tidal-TIS and nontidal-TIS cases (Fig. 4.2**c**) shows the warming signal along with the 1027.7 kg m^{-3} isopycnal layer (red arrows in Fig. 4.2**a** and 4.2**c**). The monthly-averaged salinity profiles exhibit a similar structure. The saltier water upwells along with the shelf surface in the tidal-TIS case than the nontidal-TIS case (Fig. 4.2**d-f**), and the saltier signal is found along with 1027.7 kg m^{-3} isopycnal layer (Fig. 4.2**f**). According to the monthly-averaged isopycnal layer 1027.7 kg m^{-3}, the upper boundary of mCDW, over the whole model domain of January 2012, the ASC is 1°C warmer (Fig. 4.3**a**) and ~0.08 psu saltier (Fig. 4.3**b**) along with the 1000 m contour off the TIS in the tidal-TIS case, especially at the east side of TIS. It suggests that tidally-caused warming and saltier signal occurs along with the Antarctic Slope off the TIS.

Despite the significant difference of the two cases' hydrographic profiles, the monthly-averaged velocity structure has no significant difference between the tidal-TIS and the nontidal-TIS cases on section P. The monthly-averaged velocity of January 2012 shown in figure 4.4 capture both the ASC and ASF in the two cases (red arrows in Fig. 4.4**a-b**), however, the differences along with 1027.7 kg m^{-3} isopycnal layer is subtle (Fig. 4.4**c** and **f**). Comparing with the horizontal distribution of monthly-averaged speed difference ($\sqrt{u^2 + v^2}$) shown in Fig. 4.3**c**, it suggests that the ASC becomes stronger and narrower off the TIS but not exactly on the section P, corresponding to the warmer and saltier signal occurred at east of TIS (Fig. 4.3**a-b**). The different topography feature on the section P and the east off TIS suggests that the tidal reaction in speed is sensitive to the bathymetry.

The significant difference of temperature and salinity but not in speed of the ASC in the tidal-TIS case suggests that the tide enhances the vertical mixing along with the continental slope. However, the difference of monthly-averaged vertical diffusivity value shows that the enhanced vertical mixing is not the cause of the saltier and warmer signal on the ASC in the tidal-TIS case (Fig. 4.5). The current mixing layer configuration is not extended to the isopycnal layers 1027.7 kg m^{-3}, although the vertical diffusivity value is increased in the tidal-TIS case (Fig. 4.5**c**). We thus hypothesized the tidally-induced topographic trapped waves as a cause.

4.3 Tides oscillate the ASC

The power spectrum of two velocity components of the tidal and non-tidal cases at station 1 (yellow point in Fig. 4.1**a**) from January 2010 to April 2010, where is the ASC pathway located, exhibits various ocean activities depending on frequency (Fig. 4.6). Although the monthly-averaged velocity profile has no significant discrepancy between the tidal-TIS and nontidal-TIS cases near the continental slope, the semi-diurnal tide, diurnal tide, and inertial frequency are recorded in the tidal-TIS case and fits the mooring data. In contrast, the nontidal-TIS case has none of these signals (Fig. 4.6**a-b**). The frequency in the tidal-TIS case, with respect to the zonal (u) component, is closer to the mooring data than the nontidal-TIS case (Fig. 4.6**a**). It implies that the tidal forcing is not negatable, and it enhances the various eddy activities of ASC off the TIS. We also noticed that the meridional component's power spectrum (Fig. 4.6**b**) has a significant gap between the moorings and two model outputs at frequencies between 1 to 7 days cycle, although the frequency of diurnal tide in the tidal-TIS case fits the mooring data; the power spectrum of meridional oscillation at periods between 1 day to 7 days is the same order in the two model outputs. It further suggests that the propagation of tidally induced topographic trapped waves, represented by along-shelf component, was captured in the model. Mesoscale eddy activities in the model, which occur irrespective of tide or non-tidal cases, may be too weak to represent sub-inertial motions.

Snapshots of each 6 hourly outputs of zonal component velocity along the section P (Fig. 4.7) shows that the whole water column has oscillated in the tidal-TIS case, while the nontidal-TIS case kept a steady structure without high-frequency changes. Although both two cases show a counter-current structure (blue arrows) around latitude 65°S, the one in the tidal-TIS case was oscillated by tides, but the one in the nontidal-TIS case was not (blue arrows in Fig. 4.7). The oscillation is also amplified near the bottom surface (red arrows in Fig. 4.7). It suggests that the tide oscillates the ASC, and it is a possible cause of warmer and saltier signals along with the 1027.7 kg m^{-3} isopycnal layer through horizontal mixing. By the snapshots of each 3 hourly outputs of horizonal velocity on the 1027.7 kg m^{-3} isopycnal layer shown in Fig. 4.8, the topography trapped waves are recorded along with the continental slope (1000 m contour) off the TIS in the tidal-TIS case. According to the temperature and salinity profile exhibited in Fig. 4.2, the tilting of 1027.7 kg m^{-3} isopycanl layer near the shelve (red arrows in Fig. 4.2) separates the warmer and saltier mCDW. By the horizontal mixing due to the tidally-generated topography trapped waves, the near-shelf water is horizontally mixed with off-shelf mCDW. The ASC thus becomes warmer and saltier.

Previously, Flexas *et al*. (2015) found out that the ASF could be formed by tidal forcing alone on the Weddell-Scotia Confluence because of the enhanced diapycnal mixing by reginal model simulation. Meanwhile, Steward *et al*. (2019) found out that the tidal kinetic energy and the eddy kinetic energy are dominated on the ASC core instead of the wind stress caused eddy kinetic energy in their model which covers the whole coast of Antarctica. Compared with the tidal wave propagation off the TIS observed by Peña-Molino *et al*. (2016) and tidal-TIS case above, although the tidally-enhanced vertical mixing is not well reproduced in our model, the tidal influences on the ASC is suggested not only caused by vertical mixing but also by the horizontal oscillation associated with the propagation of topographic trapped waves. It then modifies the water property along the shelf, and we will hypothesize its possible effects on the TIS in the next section.

4.4 Hypothesis: Possible mechanism of tidally modulating cross-slope heat flux

The ASC/tides interaction study will continue after further model vertical mixing configuration is adjusted. Preliminary, the ASC is significantly warmer, saltier and stronger in the tidal case off the TIS by comparing with two model outputs. Figure 4.12 exhibits the temperature and speed difference of tidal-TIS and the nontidal-TIS cases on the 1027.7 kg m^{-3} isopyncal layer over 2 decades (see Chapter 2 Models and Data Description). The warming signal is not only occurred along with the ASC but also intruded into the TIS. The ASC's speed in the tidal-TIS is strengthen along with the slope and the ice shelf. Here we hypothesize a possible mechanism of modulating the cross-slope heat flux by tides.

In 1985, Bower, Rossby and Lillibridge (1985) raised a question that, the Gulf stream, a western boundary current on the subtropic Atlantic Ocean, is a barrier or blender to the water mass. Because the transition between the water masses in the open ocean and continental slope is sharp and coincides with the Gulf Stream. They found that the water mass exchange is limited by the Gulf Stream above the 1027.1 kg m^{-s} isopycnal layer. Below this layer, there is no clear boundary between water masses since the PV across the Gulf Stream is homogenized by mesoscale exchange (Bower, Rossby and Lillibridge, 1985). Qiu (1995) later reveals that the potential vorticity gradient across boundary current is being a dynamical boundary for North Pacific Intermediate Water in the North Pacific.

In the ASC's case, PV ($q = \frac{-fN^2}{g}$, where f, g, and N^2 is Coriolis force, gravity acceleration and buoyancy frequency, respectively) is increased substantially shown in Fig. 4.3**d**, since the ASC's hydrographic property is modified as well (Fig. 4.3**a-b**). The increased PV thus becomes a potential barrier on the isopycnal layers for water exchange, which includes the heat transport, and thus regulates the across-slope heat flux.

However, based on Bower, Rossby and Lillibridge (1985)'s study, the barrier effect of Gulf Stream is till 1027.0 kg m^{-3} isopycnal layer. It suggests that the ASC's PV barrier could only be valid in specific layers and cannot extend to the shelve bottom surface since the across-slope PV is homogenized caused by amplified tidal oscillation.

We finally hypothesize that a two-layers tidally modified ASC depends on the isopycnal layers. In addition to the PV barrier hypothesis, the PV barrier enhanced by topographic trapped waves propagating along with the slope could modulate the cross-slope heat transport in the layer where the ASC dominated. The ASC thus becomes a barrier in the upper layer. Therefore, the evaluation of heat flux across the slope by each isopycnal layers is necessary to identify the reaction of tidal forcing in details. We will then design and schedule the experiments to investigate the hypothesis for on-shore heat transport on different ASC isopycnal layers after the vertical mixing layer adjusted.

This page intentionally left blank

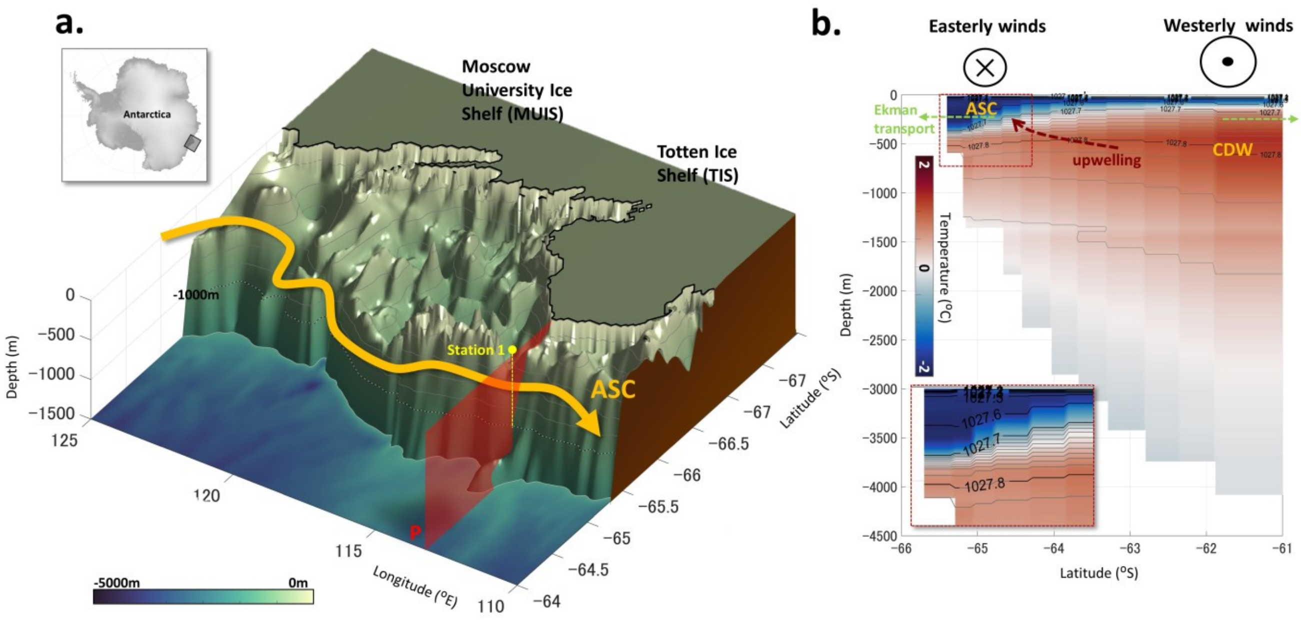

Figure 4.1 Antarctic Slope Current (ASC) and temperature structure off the Totten Ice Shelf (TIS). **a**. Model topographic features of the Antarctic Slope off the TIS, where the location shown in the upper-left window. The shade areas represent the depth of the ocean. The black dashed and grey contours denote the 1000 m iso-depth and 200 m depths intervals. To illustrate the details of the TIS and Antarctic Slope, the bird's-eye view plot extends only to a depth of 1500 m, whereas the rest of the study area is represented as shades on the floor. The arrow represents the Antarctic Slope Current (ASC). The transparent red section denotes the section P where Peña-Molino *et al*. (2016)'s study investigated. The yellow dashed line indicates Peña-Molino *et al*. (2016)'s mooring station. **b**. In-situ observation of temperature (shade) on the section P on January 2012. Black and grey contours represent the isopycnal layers with intervals 0.1 kg m^{-3} and 0.01 kg m^{-3}, respectively. Abbreviation CDW stands for Circumpolar Deep Water. The dashed green arrows and red arrows denote the direction of Ekman transport and upwelling, respectively. The circles above show the direction of winds.

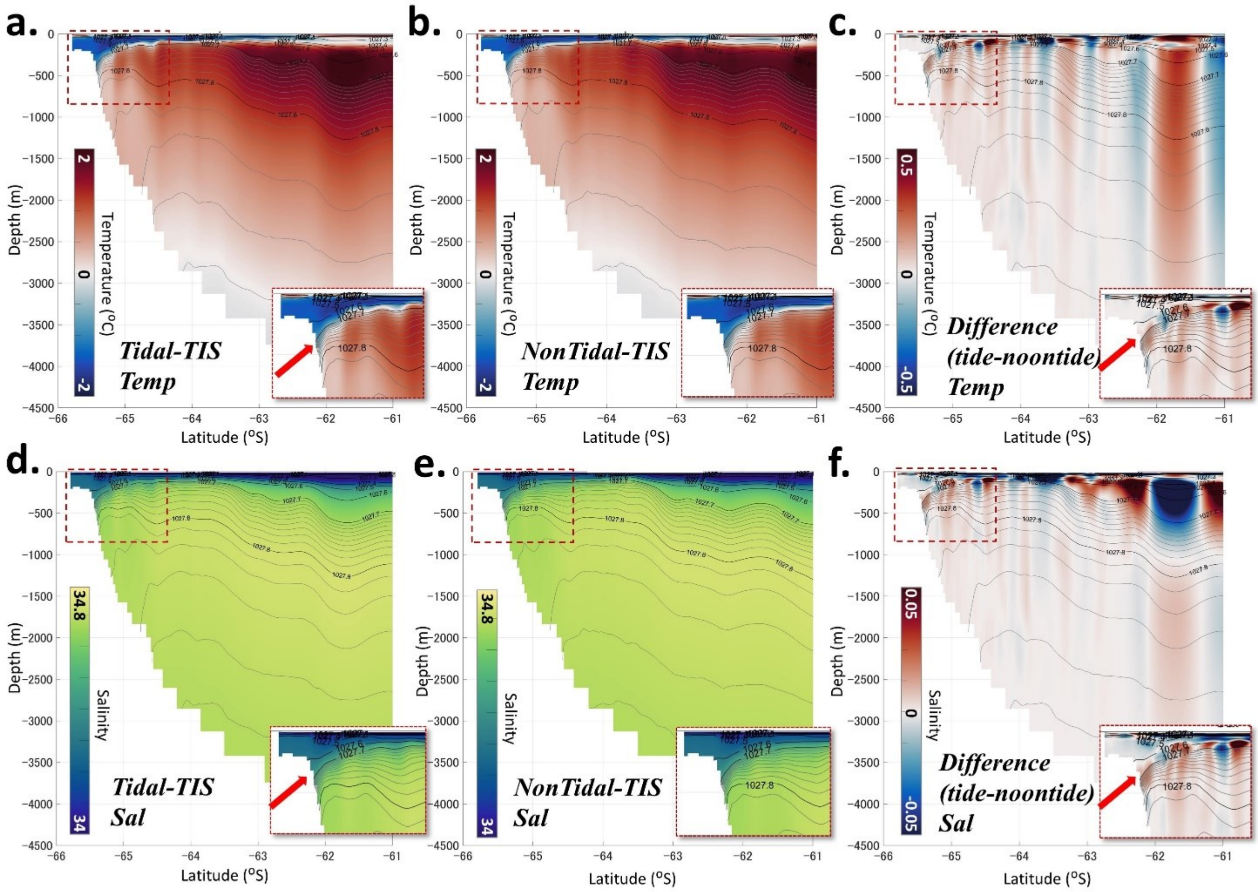

Figure 4.2 Monthly-averaged model temperature and salinity outputs on the section P. **a**. the tidal-TIS case's January 2012 monthly-averaged temperature (shade) on the section P. Black and grey contours represent the isopycnal layers with intervals 0.1 kg m^{-3} and 0.01 kg m^{-3}, respectively. Small window zooms the details of slope area. Red arrow points the interface between the slope and the isopycnal contours. **b**. same as panel **a** but for nontidal-TIS case. **c**. same as panel **a** but for difference (tidal-TIS case minus nontidal-TIS case). The isopycnal contours are as same as the tidal-TIS cases. **d-f**. same as panels **a-c** but for salinity.

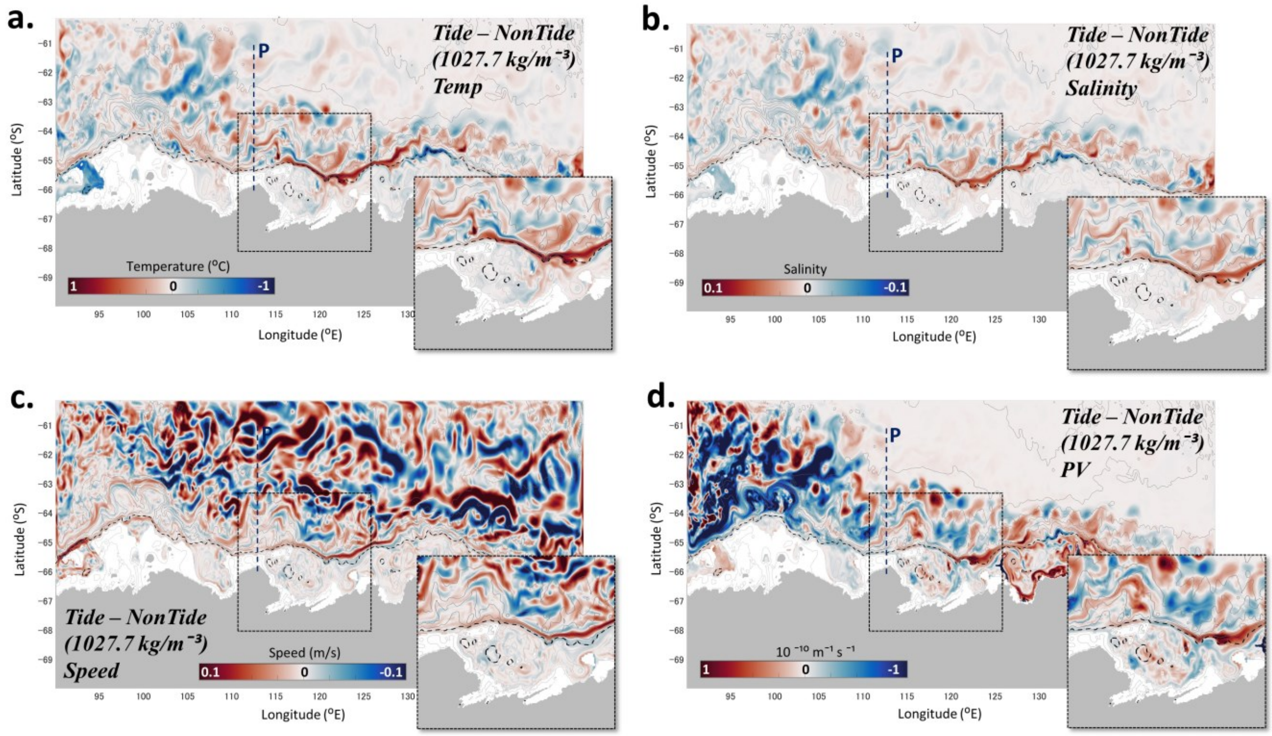

Figure 4.3 Hydrographic differences between the tidal-TIS and the nontidal-TIS case on the 1027.7 kg m^{-3} isopycnal layer. **a**. Temperature difference between the tidal-TIS and the nontidal-TIS cases (tide-TIS minus nontidal-TIS) on the 1027.7 kg m^{-3} isopycnal layer. The black dashed and grey contours denote the 1000 m iso-depth and 500 m depths intervals. Dashed blue line represents the section P. Lower-right window zooms the details of the TIS. **b**. same as panel **a** but for salinity. **c**. same as panel **a** but for flow speed ($\sqrt{u^2+v^2}$). **d**. same as panel **a** but for potential vorticity ($q = -fN^2/g$).

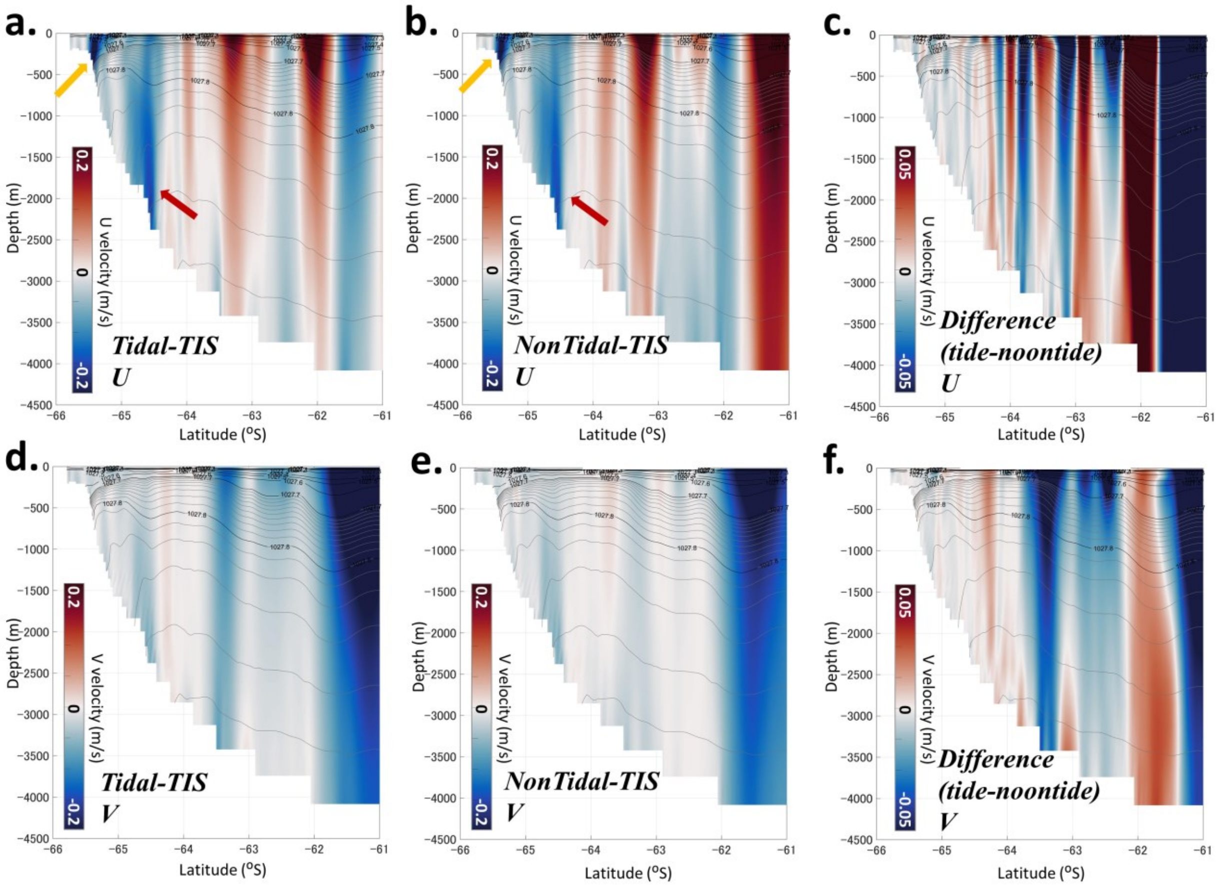

Figure 4.4 Monthly-averaged model velocity outputs on the section P. **a**. the tidal-TIS case's January 2012 monthly-averaged zonal velocity (u, shown in shade) on the section P. Black and grey contours represent the isopycnal layers with intervals 0.1 kg m^{-3} and 0.01 kg m^{-3}, respectively. Yellow and red arrows point the ASC and ASF, respectively. **b**. same as panel **a** but for nontidal-TIS case. **c**. same as panel **a** but for difference (tidal-TIS case minus nontidal-TIS case). The isopycnal contours are as same as the tidal-TIS cases. **d-f**. same as panels **a-c** but for meridional velocity (v, shown in shade).

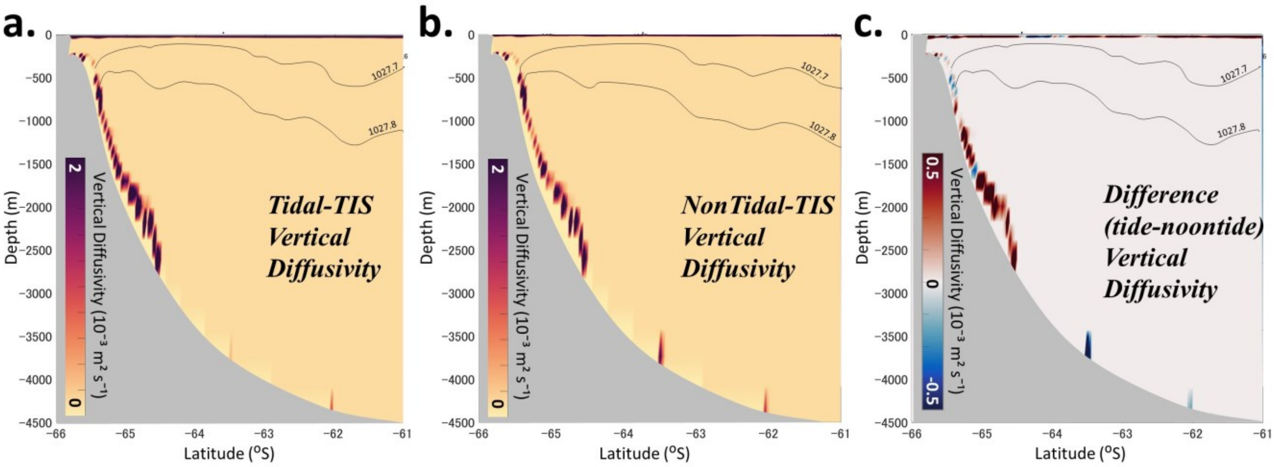

Figure 4.5 Monthly-averaged model vertical diffusivity outputs on the section P. **a**. the tidal-TIS case's January 2012 monthly-averaged vertical diffusivity (shade) on the section P. Black contours represent 1027.7 kg m^{-3} and 1027.8 kg m^{-3} isopycnal layers, respectively. **b**. same as panel **a** but for nontidal-TIS case. **c**. same as panel **a** but for difference (tidal-TIS case minus nontidal-TIS case). The isopycnal contours are as same as the tidal-TIS cases.

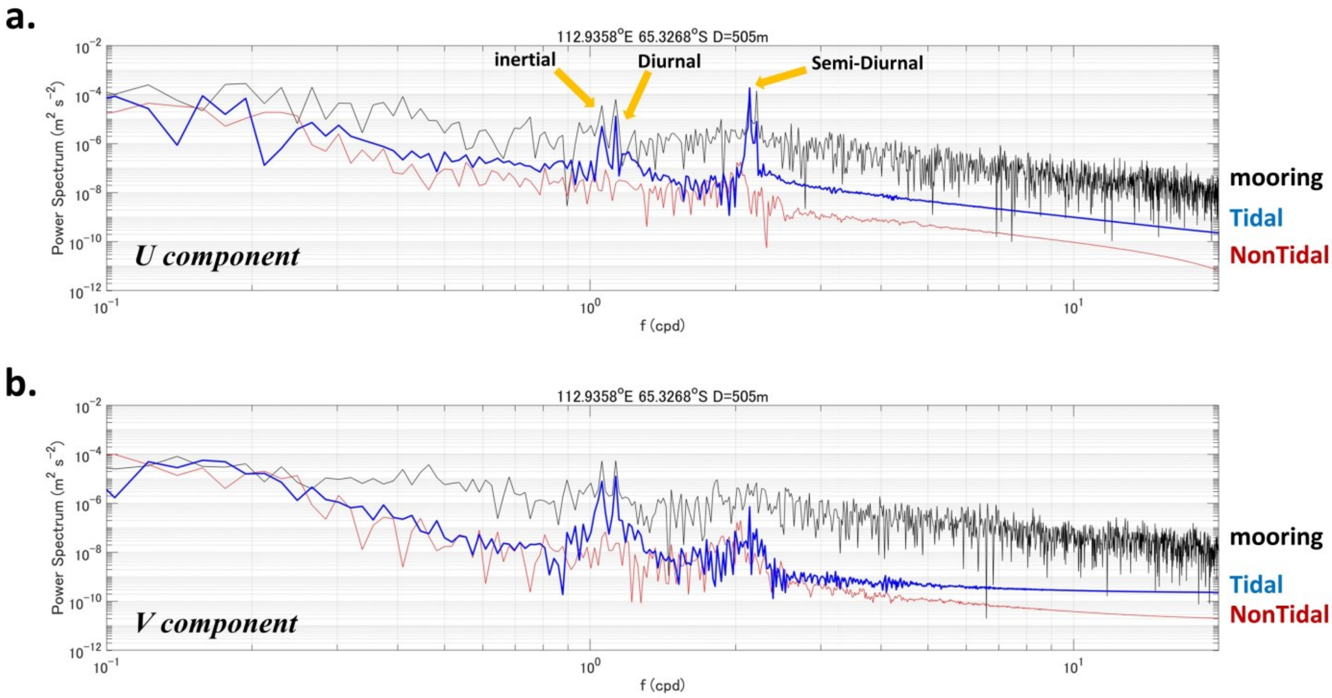

Figure 4.6 Velocity power spectrum of the tidal-TIS, nontidal-TIS cases and the mooring data on the station 1, 505 m depth. **a**. Zonal component velocity (u) power spectrum from January to April 2010. Black, blue and red lines denote the mooring data, the tidal-TIS and the nontidal-TIS cases. The yellow arrows point the inertial, diurnal, and semi-diurnal frequency. **b**. same as panel **a** but for meridional component velocity (v) power spectrum.

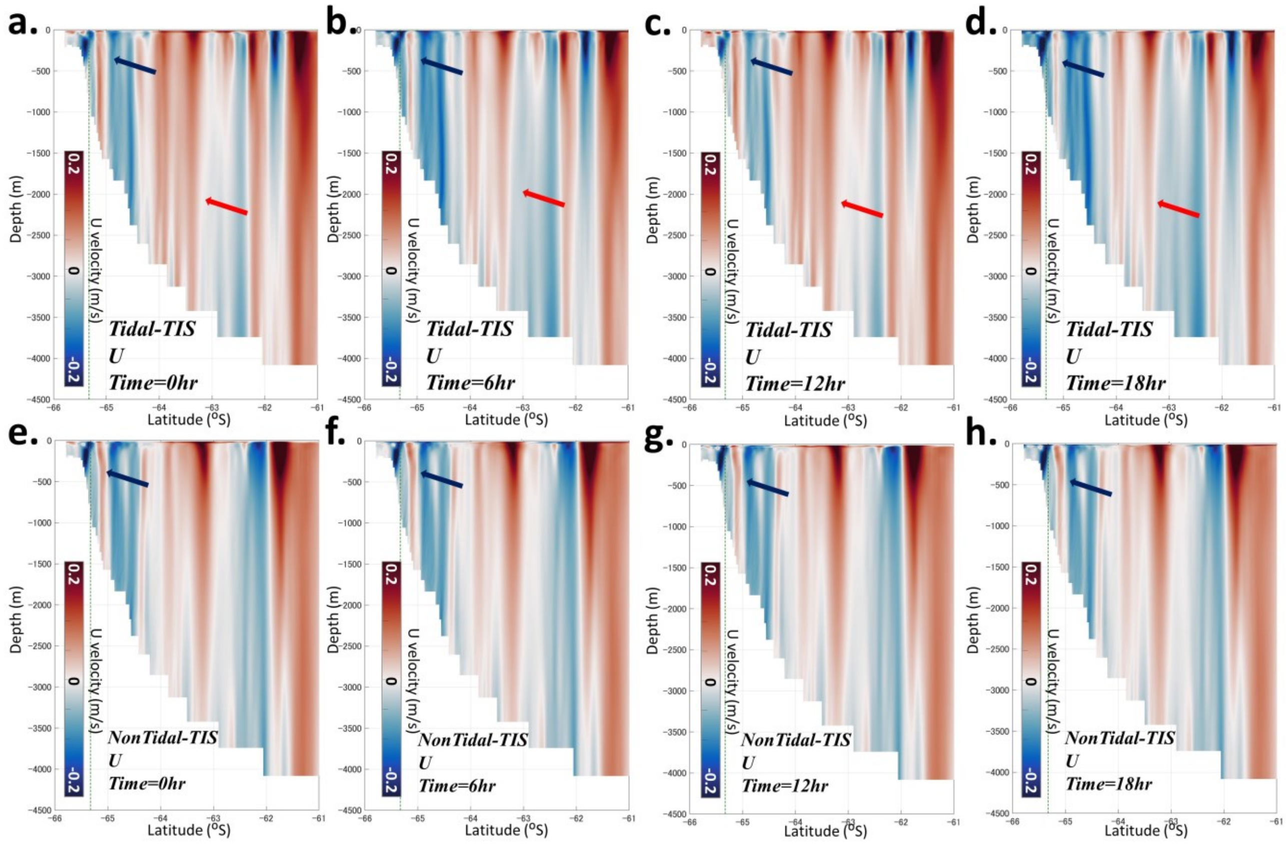

Figure 4.7 Snapshot of model's zonal velocity with 6 hours intervals on section P. a-b. The snapshot of tidal-TIS case's zonal velocity (*u*, shown in shade) with 6 hours intervals. The blue and red arrows point the counter-current and the amplified tidal oscillation above bottom surface, respectively. **e-h**. same as panels **a-b** but for nontidal-TIS case.

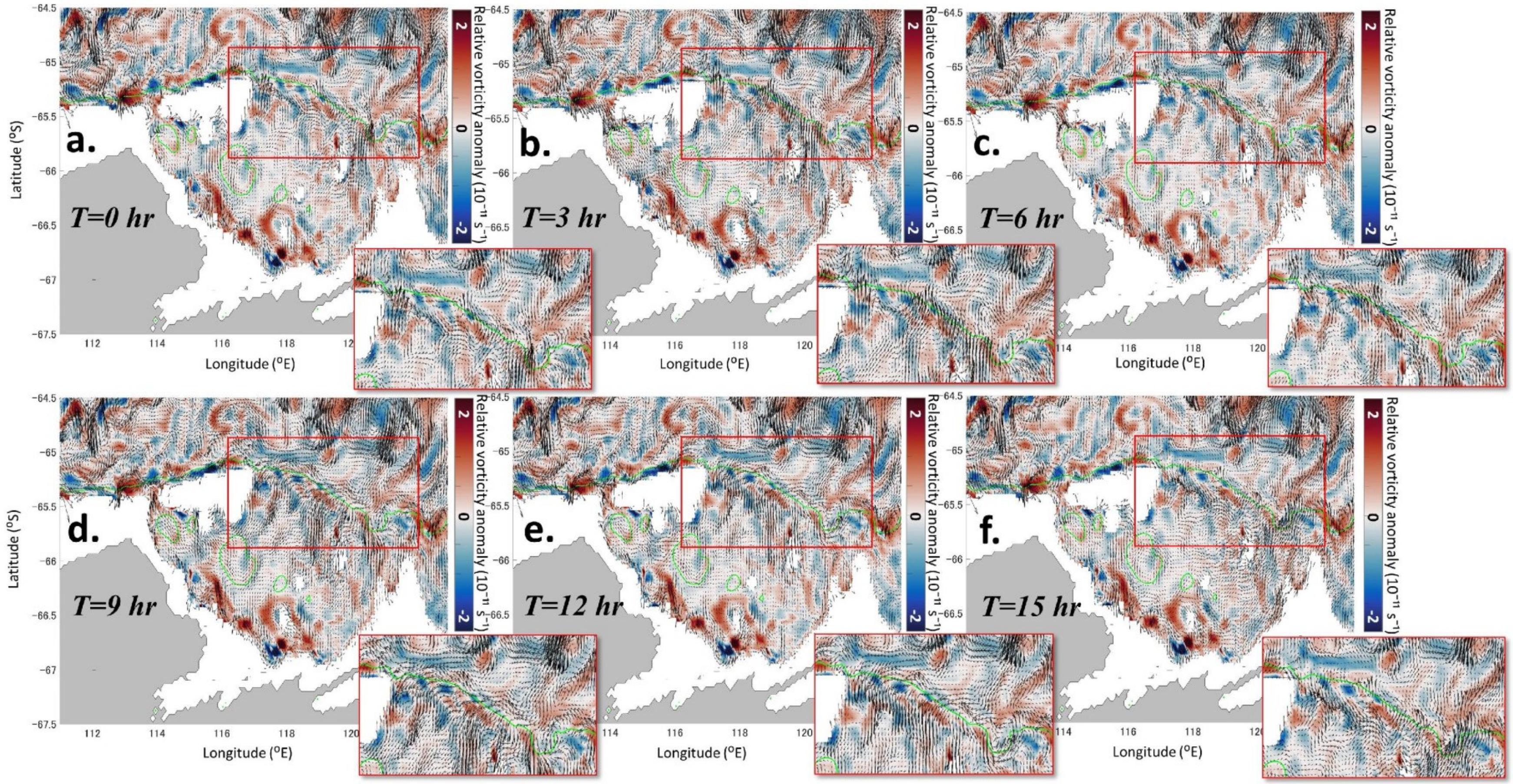

Figure 4.8 Propagation of topographic trapped waves. Snapshot of the plan view of the velocity anomaly (vector) and relative vorticity ($[\zeta] = \boldsymbol{k} \cdot \nabla \times [\boldsymbol{u}]$) anomaly (shade) on the isopycnal layer 1027.7 kg m^{-3} of the tidal-TIS case at 3-hour time steps. Green contours denote 1000 m depth. **a**. 0 hr. **b**. 3 hr. **c**. 6 hr. **d**. 9 hr. **e**. 12 hr. **f**. 15 hr.

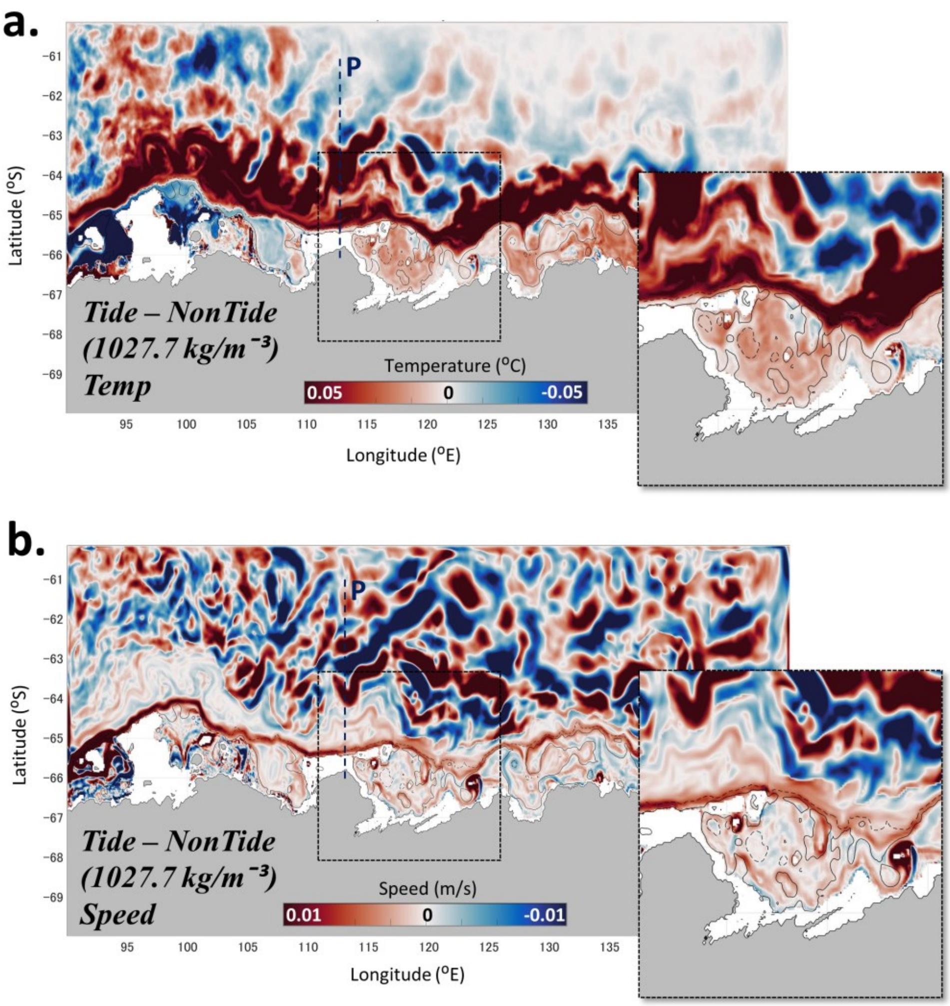

Figure 4.9 Temperature and speed difference between the tidal-TIS and the nontidal-TIS cases on the 1027.7 kg m-3 isopycnal layers. a. The temperature differences between two cases (tidal-TIS minus nontidal-TIS cases) over 2 decades from January 1992 to December 2013 on the 1027.7 kg m^{-3} isopycnal layer. Black solid and dashed contours denote 500 m and 1000 m depth, respectively. **b**. same as panel **a** but for speed.

This page intentionally left blank

Chapter 5

General Conclusion

This study exhibits that the wind-driven boundary currents are substantially modified by tidally-rectified phenomena and further change the large-scale flow pattern. In the North Pacific, the East Kamchatka Current (EKC)'s pathway is determined by a tidally-rectified overturing cell above an underwater bank. The tidally-modified EKC thus enhances the interbasin exchange between the Sea of Okhotsk and the North Pacific by approaching the Middle Island Chain (MIC) on the Kuril Islands. The intra-models comparison shows that the tidal oscillation is the key to reproduce the interbasin exchange by capturing the accurate boundary current dynamics when the model's resolution is increased significantly.

The discussion of possible tidal impacts on the Antarctic Slope Current (ASC) provides us a picture that the tidal influences on the wind-driven boundary currents is not only specified at the North Pacific, but also possible detected in other climate sensitive high-latitude regions. The tides oscillate the ASC off the Totten Ice Shelf (TIS), and the ASC is then strengthened and warmed by tidally-induced topographic trapped waves. In addition to the tidally-modified EKC, the tidally-induced topography trapped waves propagating along with the coast have various phenomena based on the topographic features.

Conventionally, the ocean general circulation models (OGCMs) did not obtain the tidal forcing since it is treated as regular noises as we described in the Introduction. However, both two cases in this study show that the tides play a key role in wind-driven boundary current dynamics and resultant in large-scale flow patterns. It suggests that the tidal configuration is essential in OGCMs because those important boundary currents bathed in various tidal activities though different topography features especially when the model's spatial resolution is increased significantly. The representation of tidal phenomena is a key to reproduce the boundary currents accurately in the future high-resolution OGCMs.

This page intentionally left blank

References

Amante, C. and Eakins, B. W. (2009) ‘ETOPO1 1 Arc-Minute Global Relief Model: Procedures, Data Sources and Analysis’, *NOAA Technical Memorandum NESDIS NGDC-24*, (March), p. 19. doi: 10.1594/PANGAEA.769615.

Beckmann, A. and Haidvogel, D. B. (1997) ‘A numerical simulation of flow at Fieberling Guyot’, *Journal of Geophysical Research C: Oceans*, 102(C3), pp. 5595–5613. doi: 10.1029/96JC03414.

Beckmann, A. and Mohn, C. (2002) ‘The upper ocean circulation at Great Meteor Seamount. Part II: Retention potential of the seamount-induced circulation’, *Ocean Dynamics*, 52(4), pp. 194–204. doi: 10.1007/s10236-002-0018-3.

Bower, A. S., Rossby, H. T. and Lillibridge, J. L. (1985) ‘The Gulf Stream—Barrier or Blender?’, *Journal of Physical Oceanography*, 15(1), pp. 24–32. doi: 10.1175/1520-0485(1985)015<0024:TGSOB>2.0.CO;2.

Brink, K. H. (1990) ‘On the generation of seamount-trapped waves’, *Deep Sea Research Part A, Oceanographic Research Papers*, 37(10), pp. 1569–1582. doi: 10.1016/0198-0149(90)90062-Z.

Chapman, D. C. (1989) ‘Enhanced subinertial diurnal tides over isolated topographic features’, *Deep Sea Research Part A, Oceanographic Research Papers*, 36(6), pp. 815–824. doi: 10.1016/0198-0149(89)90030-7.

Codiga, D. L. and Eriksen, C. C. (1997) ‘Observations of low-frequency circulation and amplified subinertial tidal currents at Cobb Seamount’, *Journal of Geophysical Research: Oceans*, 102(C10), pp. 22993–23007. doi: 10.1029/97JC01451.

Dai, A. and Trenberth, K. E. (2002) ‘Estimates of freshwater discharge from continents: Latitudinal and seasonal variations’, *Journal of Hydrometeorology*, 3(6), pp. 660–687. doi: 10.1175/1525-7541(2002)003<0660:EOFDFC>2.0.CO;2.

Dee, D. P. *et al.* (2011) ‘The ERA-Interim reanalysis: Configuration and performance of the data assimilation system’, *Quarterly Journal of the Royal Meteorological Society*, 137(656), pp. 553–597. doi: 10.1002/qj.828.

Eriksen, C. C. (1991) 'Observations of amplified flows atop a large seamount', *Journal of Geophysical Research*, 96(C8), p. 15227. doi: 10.1029/91jc01176.

Flexas, M. M. *et al.* (2015) 'Role of tides on the formation of the Antarctic Slope Front at the Weddell-Scotia Confluence', *Journal of Geophysical Research: Oceans*, 120(5), pp. 3658–3680. doi: 10.1002/2014JC010372.

Fretwell, P. *et al.* (2013) 'Bedmap2: Improved ice bed, surface and thickness datasets for Antarctica', *Cryosphere*, 7(1), pp. 375–393. doi: 10.5194/tc-7-375-2013.

Gargett, A. E. and Holloway, G. (1984) 'Dissipation and Diffusion By Internal Wave Breaking.', *Journal of Marine Research*, 42(1), pp. 15–27. doi: 10.1357/002224084788506158.

Greene, C. A. *et al.* (2017) 'Wind causes Totten Ice Shelf melt and acceleration', *Science Advances*, 3(11), pp. 1–8. doi: 10.1126/sciadv.1701681.

Gwyther, D. E. *et al.* (2014) 'Simulated melt rates for the Totten and Dalton ice shelves', *Ocean Science*, 10(3), pp. 267–279. doi: 10.5194/os-10-267-2014.

Haidvogel, D. B. *et al.* (1993) 'Numerical simulation of flow around a tall isolated seamount. Part II: resonant generation of trapped waves', *Journal of Physical Oceanography*, pp. 2373–2391. doi: 10.1175/1520-0485(1993)023<2373:NSOFAA>2.0.CO;2.

Hasumi, H. (2006) 'CCSR Ocean Component Model (COCO) Version 4.0', *CCSR report No. 25*, p. 103.

Hibiya, T. and Nagasawa, M. (2004) 'Latitudinal dependence of diapycnal diffusivity in the thermocline estimated using a finescale parameterization', *Geophysical Research Letters*, 31(1), pp. 4–7. doi: 10.1029/2003GL017998.

Hibiya, T., Nagasawa, M. and Niwa, Y. (2006) 'Global mapping of diapycnal diffusivity in the deep ocean based on the results of expendable current profiler (XCP) surveys', *Geophysical Research Letters*, 33(3), pp. 2–5. doi: 10.1029/2005GL025218.

Historical GEBCO data sets. Available at: https://www.gebco.net/data_and_products/historical_data_sets/#gebco_one (Accessed: 5 September 2020).

Jayne, S. R. and Laurent, L. C. S. (2001) 'Tidal Dissipation over Rough', 28(5), pp. 811–814.

Katsumata, K. *et al.* (2004) 'Water exchange and tidal currents through the Bussol' Strait revealed by direct current measurements', *Journal of Geophysical Research C: Oceans*, 109(9), pp. 1–11. doi: 10.1029/2003JC001864.

Katsumata, K. and Yasuda, I. (2010) 'Estimates of non-tidal exchange transport between the sea of Okhotsk and the North Pacific', *Journal of Oceanography*, 66(4), pp. 489–504. doi: 10.1007/s10872-010-0041-9.

Kawasaki, T. and Hasumi, H. (2010) 'Role of localized mixing around the Kuril Straits in the Pacific thermohaline circulation', *Journal of Geophysical Research: Oceans*, 115(11), pp. 1–13. doi: 10.1029/2010JC006130.

Kida, S. (2011) 'The impact of open oceanic processes on the Antarctic Bottom Water outflows', *Journal of Physical Oceanography*, 41(10), pp. 1941–1957. doi: 10.1175/2011JPO4571.1.

Kida, S. and Qiu, B. (2013) 'An exchange flow between the okhotsk sea and the North Pacific driven by the East Kamchatka Current', *Journal of Geophysical Research: Oceans*, 118(12), pp. 6747–6758. doi: 10.1002/2013JC009464.

Kowalik, Z. and Polyakov, I. (1998) 'Tides in the Sea of Okhotsk', *Journal of Physical Oceanography*, 28(7), pp. 1389–1409. doi: 10.1175/1520-0485(1998)028<1389:TITSOO>2.0.CO;2.

Lam, F. P. A., Maas, L. R. M. and Gerkema, T. (2004) 'Spatial structure of tidal and residual currents as observed over the shelf break in the Bay of Biscay', *Deep-Sea Research Part I: Oceanographic Research Papers*, 51(8), pp. 1075–1096. doi: 10.1016/j.dsr.2004.03.008.

Laurent, L. C. S., Simmons, H. L. and Jayne, S. R. (2002) 'Estimating tidally driven mixing in the deep ocean', 29(23), pp. 19–22. doi: 10.1029/2002GL015633.

Lavelle, J. W., Lozovatsky, I. D. and Smith IV, D. C. (2004) 'Tidally induced turbulent mixing at Irving Seamount - Modeling and measurements', *Geophysical Research Letters*, 31(10), pp. 2–5. doi: 10.1029/2004GL019706.

Lavelle, J. W. and Mohn, C. (2010) 'Motion, commotion, and biophysical connections at deep ocean seamounts', *Oceanography*, 23(1), pp. 90–103. doi: 10.5670/oceanog.2010.64.

Lembke-Jene, L. *et al.* (2017) 'Deglacial variability in Okhotsk Sea Intermediate Water ventilation and biogeochemistry: Implications for North Pacific nutrient supply and productivity', *Quaternary Science Reviews*, 160, pp. 116–137. doi: 10.1016/j.quascirev.2017.01.016.

Levitus, S. *et al.* (2010) 'World ocean atlas 2009'. Edited by O. C. L. National Oceanographic Data Center (U.S.) and N. E. S. United States Data, and Information Service,. (NOAA atlas NESDIS ; 68). Available at: https://repository.library.noaa.gov/view/noaa/1259.

Losch, M. (2008) 'Modeling ice shelf cavities in a z coordinate ocean general circulation model', *Journal of Geophysical Research: Oceans*, 113(8), pp. 1–

15. doi: 10.1029/2007JC004368.

Losch, M. *et al.* (2010) ‘On the formulation of sea-ice models. Part 1: Effects of different solver implementations and parameterizations’, *Ocean Modelling*, 33(1–2), pp. 129–144. doi: 10.1016/j.ocemod.2009.12.008.

Marmer, H. A. (1922) ‘The Problems of the Tide’, *Source: The Scientific Monthly*, 14(3), pp. 209–222.

Martin, A. *et al.* (2017) ‘Circulation and water mass transports on the East Antarctic shelf in the Mertz Glacier region’, *Deep-Sea Research Part I: Oceanographic Research Papers*, 126(May 2016), pp. 1–20. doi: 10.1016/j.dsr.2017.05.007.

Maslowski, W. *et al.* (2014) ‘The Large Scale Ocean Circulation and Physical Processes Controlling Pacific-Arctic Interactions’, in *The Pacific Arctic Region*. Dordrecht: Springer Netherlands, pp. 101–132. doi: 10.1007/978-94-017-8863-2_5.

Matsuda, J. *et al.* (2015) ‘Overturning circulation that ventilates the intermediate layer of the Sea of Okhotsk and the North Pacific: The role of salinity advection’, *Journal of Geophysical Research: Oceans*, 120(3), pp. 1462–1489. doi: 10.1002/2014JC009995.

Mensah, V. and Ohoshima, K. I. (2021) ‘Weakened overturning and tide control the properties of Oyashio Intermediate Water, a key water mass in the North Pacific’, *Scientific Reports*, 11(1), doi: 10.1038/s41598-021-93901-6.

Mertz, G. and Wright, D. G. (1992) ‘Interpretations of the JEBAR Term’, *Journal of Physical Oceanography*, pp. 301–305. doi: 10.1175/1520-0485(1992)022<0301:iotjt>2.0.co;2.

Metzger, E. J. and Hurlburt, H. E. (2001) ‘The importance of high horizontal resolution and accurate coastline geometry in modeling South China Sea Inflow’, *Geophysical Research Letters*, 28(6), pp. 1059–1062. doi: 10.1029/2000GL012396.

MIRC JTOPO30 (no date). Available at: http://www.mirc.jha.jp/products/finished/JTOPO30/ (Accessed: 9 September 2020).

Mohajerani, Y., Velicogna, I. and Rignot, E. (2018) ‘Mass Loss of Totten and Moscow University Glaciers, East Antarctica, Using Regionally Optimized GRACE Mascons’, *Geophysical Research Letters*, 45(14), pp. 7010–7018. doi: 10.1029/2018GL078173.

Mohn, C. *et al.* (2013) ‘Tidal and residual currents over abrupt deep-sea topography based on shipboard ADCP data and tidal model solutions for three popular bathymetry grids', *Ocean Dynamics*, 63(2–3), pp. 195–208. doi: 10.1007/s10236-013-0597-1.

Nakamura, T. *et al.* (2000) 'Tidal exchange through the Kuril Straits', *Journal of Physical Oceanography*, 30(7), pp. 1622–1644. doi: 10.1175/1520-0485(2000)030<1622:TETTKS>2.0.CO;2.

Nakamura, T. *et al.* (2006) 'Effects of tidal mixing at the Kuril Straits on North Pacific ventilation: Adjustment of the intermediate layer revealed from numerical experiments', *Journal of Geophysical Research: Oceans*, 111(4), pp. 1–18. doi: 10.1029/2005JC003142.

Nakamura, T. *et al.* (2014) 'Effects of temporal variation in tide-induced vertical mixing in the Kuril Straits on the thermohaline circulation originating in the Okhotsk Sea', *Progress in Oceanography*, 126, pp. 135–145. doi: 10.1016/j.pocean.2014.05.007.

Nakamura, T. and Awaji, T. (2001) 'A growth mechanism for topographic internal waves generated by an oscillatory flow', *Journal of Physical Oceanography*, 31(8 PART 2), pp. 2511–2524. doi: 10.1175/1520-0485(2001)031<2511:agmfti>2.0.co;2.

Nakamura, T. and Awaji, T. (2004) 'Tidally induced diapycnal mixing in the Kuril Straits and its role in water transformation and transport: A three-dimensional nonhydrostatic model experiment', *Journal of Geophysical Research C: Oceans*, 109(9), pp. 1–22. doi: 10.1029/2003JC001850.

Nakayama, Y. *et al.* (2019) 'Pathways of ocean heat towards Pine Island and Thwaites grounding lines', *Scientific Reports*, 9(1), pp. 1–9. doi: 10.1038/s41598-019-53190-6.

Nakayama, Y. *et al.* (2021) 'Antarctic Slope Current modulates warm ocean intrusions towards Totten Glacier'., revising (July 2021)

Nishioka, J., Mitsudera, H., *et al.* (2014) 'Biogeochemical and physical processes in the Sea of Okhotsk and the linkage to the Pacific Ocean', *Progress in Oceanography*, 126, pp. 1–7. doi: 10.1016/j.pocean.2014.04.027.

Nishioka, J., Nakatsuka, T., *et al.* (2014) 'Quantitative evaluation of iron transport processes in the Sea of Okhotsk', *Progress in Oceanography*, 126, pp. 180–193. doi: 10.1016/j.pocean.2014.04.011.

Noh, Y. and Jin Kim, H. (1999) 'Simulations of temperature and turbulence structure of the oceanic boundary layer with the improved near-surface process', *Journal of Geophysical Research: Oceans*, 104(C7), pp. 15621–15634. doi: 10.1029/1999JC900068.

Ohshima, K. I. *et al.* (2010) ‘Seasonal variation in the in- and outflow of the Okhotsk Sea with the North Pacific’, *Deep-Sea Research Part II: Topical Studies in Oceanography*, 57(13–14), pp. 1247–1256. doi: 10.1016/j.dsr2.2009.12.012.

Ono, J. *et al.* (2006) ‘Amplification of diurnal tides over Kashevarov Bank in the Sea of Okhotsk and its impact on water mixing and sea ice’, *Deep-Sea Research Part I: Oceanographic Research Papers*, 53(3), pp. 409–424. doi: 10.1016/j.dsr.2005.11.002.

Onogi, K. *et al.* (2007) ‘The JRA-25 reanalysis’, *Journal of the Meteorological Society of Japan*, 85(3), pp. 369–432. doi: 10.2151/jmsj.85.369.

Padman, L. *et al.* (2002) ‘A new tide model for the Antarctic ice shelves and seas’, *Annals of Glaciology*, 34, pp. 247–254. doi: 10.3189/172756402781817752.

Padman, L., Siegfried, M. R. and Fricker, H. A. (2018) ‘Ocean Tide Influences on the Antarctic and Greenland Ice Sheets’, *Reviews of Geophysics*, 56(1), pp. 142–184. doi: 10.1002/2016RG000546.

Peña-Molino, B., McCartney, M. S. and Rintoul, S. R. (2016) ‘Direct observations of the Antarctic Slope Current transport at 113°E’, *Journal of Geophysical Research: Oceans*, 121(10), pp. 7390–7407. doi: 10.1002/2015JC011594.

Prants, S. *et al.* (2018) ‘Alaskan Stream flow in the eastern subarctic Pacific and the eastern Bering Sea and its impact on biological productivity’, *Biogeosciences Discussions*, (February), pp. 1–22. doi: 10.5194/bg-2017-477.

Pritchard, H. D. *et al.* (2012) ‘Antarctic ice-sheet loss driven by basal melting of ice shelves’, *Nature*, 484(7395), pp. 502–505. doi: 10.1038/nature10968.

Qiu, B. (1995) ‘Why Is the Spreading of the North Pacific Intermediate Water Confined on Density Surfaces around σ θ = 26.8?’, *Journal of Physical Oceanography*, 25(1), pp. 168–180. doi: 10.1175/1520-0485(1995)025<0168:WITSOT>2.0.CO;2.

Rintoul, S. R. *et al.* (2016) ‘Ocean heat drives rapid basal melt of the totten ice shelf’, *Science Advances*, 2(12), pp. 1–6. doi: 10.1126/sciadv.1601610.

Robertson, R. and Dong, C. (2019) ‘An evaluation of the performance of vertical mixing parameterizations for tidal mixing in the Regional Ocean Modeling System (ROMS)’, *Geoscience Letters*, 6(1), pp. 1–18. doi: 10.1186/s40562-019-0146-y.

Robertson, R., Dong, J. and Hartlipp, P. (2017) ‘Diurnal Critical Latitude and the Latitude Dependence of Internal Tides, Internal Waves, and Mixing Based on Barcoo Seamount’, *Journal of Geophysical Research: Oceans*, 122(10), pp. 7838–7866. doi: 10.1002/2016JC012591.

Robinson, I. S. (1981) 'Tidal vorticity and residual circulation', *Deep Sea Research Part A, Oceanographic Research Papers*, 28(3), pp. 195–212. doi: 10.1016/0198-0149(81)90062-5.

Rogachev, K. and Shlyk, N. (2018a) 'Strong tidal currents over two shallow banks in the western subarctic Pacific', *Ocean Dynamics*, 68(9), pp. 1093–1107. doi: 10.1007/s10236-018-1182-4.

Rogachev, K. and Shlyk, N. (2018b) 'Strong tidal currents over two shallow banks in the western subarctic Pacific', *Ocean Dynamics*, 68(9), pp. 1093–1107. doi: 10.1007/s10236-018-1182-4.

Röske, F. (2005) 'Global oceanic heat and fresh water forcing datasets based on ERA-40 and ERA-15 Reports on Earth System Science', *Max-Planck Institute for Meteorology Report*.

Röske, F. (2006) 'A global heat and freshwater forcing dataset for ocean models', *Ocean Modelling*, 11(3–4), pp. 235–297. doi: 10.1016/j.ocemod.2004.12.005.

Sansón, L. Z. (2010) 'Solutions of barotropic trapped waves around seamounts', *Journal of Fluid Mechanics*, 661(October 2010), pp. 32–44. doi: 10.1017/S0022112010003034.

Sasaki, H. *et al.* (2014) 'Impact of oceanic-scale interactions on the seasonal modulation of ocean dynamics by the atmosphere', *Nature Communications*, 5. doi: 10.1038/ncomms6636.

Sasaki, H. and Klein, P. (2012) 'SSH Wavenumber Spectra in the North Pacific from a high-resolution: Realistic simulation', *Journal of Physical Oceanography*, 42(7), pp. 1233–1241. doi: 10.1175/JPO-D-11-0180.1.

Schwiderski, E. W. (1980) 'On charting global ocean tides', *Reviews of Geophysics*, 18(1), pp. 243–268. doi: 10.1029/RG018i001p00243.

Sheremet, V. A. (2001) 'Hysteresis of a western boundary current leaping across a gap', *Journal of Physical Oceanography*, 31(5), pp. 1247–1259. doi: 10.1175/1520-0485(2001)031<1247:HOAWBC>2.0.CO;2.

Shu, H. W. *et al.* (2021) 'Tidally modified western boundary current drives interbasin exchange between the Sea of Okhotsk and the North Pacific', *Scientific Reports*, 11(1), pp. 1–16. doi: 10.1038/s41598-021-91412-y.

Silvano, A. *et al.* (2019) 'Seasonality of Warm Water Intrusions Onto the Continental Shelf Near the Totten Glacier', *Journal of Geophysical Research: Oceans*, 124(6), pp. 4272–4289. doi: 10.1029/2018JC014634.

Stewart, A. L., Klocker, A. and Menemenlis, D. (2018) 'Circum-Antarctic Shoreward Heat Transport Derived From an Eddy- and Tide-Resolving Simulation', *Geophysical Research Letters*, 45(2), pp. 834–845. doi: 10.1002/2017GL075677.

Stewart, A. L., Klocker, A. and Menemenlis, D. (2019) 'Acceleration and overturning of the antarctic slope current by winds, eddies, and tides', *Journal of Physical Oceanography*, 49(8), pp. 2043–2074. doi: 10.1175/JPO-D-18-0221.1.

Talley, L. D. (1993) 'Distribution and Formation of North Pacific Intermediate Water', *Journal of Physical Oceanography*, 23(3), pp. 517–537. doi: 10.1175/1520-0485(1993)023<0517:DAFONP>2.0.CO;2.

Tanaka, Y. *et al.* (2010) 'Numerical study of K1 internal tides in the Kuril straits', *Journal of Geophysical Research: Oceans*, 115(9), pp. 1–13. doi: 10.1029/2009JC005903.

Tanaka, Y. *et al.* (2014) 'Internal tides and turbulent mixing observed in the Bussol Strait', *Progress in Oceanography*, 126, pp. 98–108. doi: 10.1016/j.pocean.2014.04.009.

Tanaka, Y., Hibiya, T. and Niwa, Y. (2007) 'Estimates of tidal energy dissipation and diapycnal diffusivity in the Kuril Straits using TOPEX/POSEIDON altimeter data', *Journal of Geophysical Research: Oceans*, 112(10), pp. 1–9. doi: 10.1029/2007JC004172.

Tanaka, Y., Hibiya, T. and Niwa, Y. (2010) 'Assessment of the effects of tidal mixing in the Kuril straits on the formation of the North Pacific intermediate water', *Journal of Physical Oceanography*, 40(12), pp. 2569–2574. doi: 10.1175/2010JPO4506.1.

Thompson, A. F. *et al.* (2018) 'The Antarctic Slope Current in a Changing Climate', *Reviews of Geophysics*, 56(4), pp. 741–770. doi: 10.1029/2018RG000624.

Thompson, A. F. and Heywood, K. J. (2008) 'Frontal structure and transport in the northwestern Weddell Sea', *Deep-Sea Research Part I: Oceanographic Research Papers*, 55(10), pp. 1229–1251. doi: 10.1016/j.dsr.2008.06.001.

Watanabe, Y., Yasuda, I. and Tsurushima, N. (2014) 'Long-Term Changes of Greenhouse Gases in the Ocean and Their Feedback Effects on the Climate', *Western Pacific Air-Sea Interaction Study*, pp. 123–150. doi: 10.5047/w-pass.a02.003.

White, M. and Mohn, C. (2004) 'Seamounts : a review of physical processes and their influence on the seamount ecosystem', p. 40.

Whitworth, T. *et al.* (2013) 'Water Masses and Mixing Near the Antarctic Slope Front', in, pp. 1–27. doi: 10.1029/AR075p0001.

Wunsch, C. and Ferrari, R. (2004) 'Vertical mixing, energy, and the general circulation of the oceans', *Annual Review of Fluid Mechanics*, 36(1), pp. 281–314. doi: 10.1146/annurev.fluid.36.050802.122121.

Wunsch, C. and Heimbach, P. (2013) 'Chapter 21 - Dynamically and Kinematically Consistent Global Ocean Circulation and Ice State Estimates', in Siedler, G. et al. (eds) *Ocean Circulation and Climate*. Academic Press (International Geophysics), pp. 553–579. doi: https://doi.org/10.1016/B978-0-12-391851-2.00021-0.

Yagi, M. *et al.* (2014) 'Re-evaluation of turbulent mixing vertical structure in the Bussol' Strait and its impact on water masses in the Okhotsk Sea and the North Pacific', *Progress in Oceanography*, 126, pp. 121–134. doi: 10.1016/j.pocean.2014.04.023.

Yamashita, Y. *et al.* (2021) 'Widespread distribution of allochthonous fluorescent dissolved organic matter in the intermediate water of the North Pacific', *Progress in Oceanography*, 191(December 2020), p. 102510. doi: 10.1016/j.pocean.2020.102510.

Yasuda, I. (1997) 'The origin of the North Pacific Intermediate Water', *Journal of Geophysical Research C: Oceans*, 102(1), pp. 893–909. doi: 10.1029/96jc02938.

Yasuda, I. (2009) 'The 18.6-year period moon-tidal cycle in Pacific Decadal Oscillation reconstructed from tree-rings in western North America', *Geophysical Research Letters*, 36(5), pp. 18–21. doi: 10.1029/2008GL036880.

Yasuda, I., Okuda, K. and Shimizu, Y. (1996) 'Distribution and modification of North Pacific Intermediate Water in the Kuroshio-Oyashio interfrontal zone', *Journal of Physical Oceanography*, pp. 448–465. doi: 10.1175/1520-0485(1996)026<0448:DAMONP>2.0.CO;2.

Yeager, S. (2015) 'Topographic coupling of the atlantic overturning and gyre circulations', *Journal of Physical Oceanography*, 45(5), pp. 1258–1284. doi: 10.1175/JPO-D-14-0100.1.

Zhang, H., Menemenlis, D. and Fenty, I. (2018) 'ECCO LLC270 Ocean-Ice State Estimate', 510, p. 7. doi: 1721.1/119821.

This page intentionally left blank

Acknowledgements

The author shares the honor with Prof. Humio Mitsudera. Prof. H. Mitsudera brought the author into the world of ocean dynamics and gave the author a whole new aspect to observe the nature and numerical models. The models are for testing/revealing the relationship of different natural phenomena we might not be able to tell. The moments with Prof. H. Mitsudera together, including the excitement and frustrations, are permanently engraved in the author's mind.

The author also appreciates the constructive comments and suggestions from the committee, Prof. Shinichiro Kida, Prof. Kay I. Ohshima, Prof. Atsushi Kubokawa, Prof. Tomohiro Nakamura, and Prof. Yoshihiro Nakayama. At the beginning of the Ph.D. journey, Prof. S. Kida opened the author's eye to tell a story in science. During the Polar Seminar, Prof. K.I. Ohshima provided the author with systemic consideration of climate and bio-productivity. For revealing those untold phenomena, Prof. A. Kubokawa showed the author the contributions of sophisticated mathematics in every question. Since the author was unfamiliar with tidal study, Prof. T. Nakamura accomplished/built the author's knowledge of tides and their related rectification. In the end, Prof. Y. Nakayama expanded the author's field into climate models/climate variabilities and pointed a profound question to the author: How can we draw a clear picture connecting the high-frequency tides and decadal ocean phenomena through climate models? The author wishes to detect the problems and faces the true meaning of data by following the committee's lesson in his future academic career.

The co-authors for Chapter 3, Prof. H. Mitsudera, Dr. Kaihe Yamazaki, Prof. T. Nakamura, Prof. Takao Kawasaki, Prof. Takuya Nakanowatari, Dr. Hatsumi Nishikawa, and Prof. Hideharu Sasaki, are appreciated by the author. Prof. H. Mitsudera conceived this study and drafted the manuscript with the author together. The PV framework came from the excited discussion between Prof. H. Mitsudera, Dr. K. Yamazaki and the author. Prof. T. Nakamura and Prof. T. Nakanowatari joint the author with Prof. H. Mitsdera and

Dr. K. Yamazaki to discuss and interpreted the results. Prof. T. Kawasaki helped the author with the vertical mixing experiments. Dr. H. Nishikawa provided the original COCO model configurations and span up the model. For enhancing the generality of this study, Prof. H. Sasaki provided the OFES model output and wrote the method of OFES model. The study cannot be accomplished without any of them.

The author is also sincerely grateful to work with co-authors, Prof. Y. Nakayama, Prof. H. Mitsudera, Dr. K. Yamazaki, Prof. Vigan Mensah, Prof. Shigeru Aoki, Prof. T. Nakamura, and Dr. Hong Zhang, for the ongoing discussion of Antarctic Slope Current. The study is kept going on and the final answer is expected.

In addition, the author thanks Prof. Yohei Onuki, Prof. Katsuro Katsumata, Prof. Ichiro Yasuda, Prof. Yutaka Yoshikawa, Prof. Ryo Furue, Prof. V. Mensah, Prof. Maarten Buijsman, and Dr. Kenneth Hughes for their constructive comments and valuable contributions to this study. The author acknowledges Dr. Francisco Xavier Mora from Wordvice Editing Service for manuscript editing, Dr. Eric Wang for English writing style suggestion, and Dr. Huai Ching Huang for figure clearness guide.

Finally, the author personally thanks his parents, D.Y. Joe and L.J. Lu, and sister in Taiwan for understanding the author's decision. Colleagues from Owl Publishing House in Taiwan, Editor-in-Chief Ellen Hsieh, Deputy Editor-in-Cheif Jui Fang Chang, trained the structural writing to the author. Dr. Philip Yi-Chun Lo and Dr. Sung-Ching Pan care the author sincerely, especially during the pandemic. Atty. Shi-Hung Ouyang and Ms. Kotono Shinohara share a lot of loading of international administration works from the author. The author shows sincere gratitude to Prof. V. Mensah and Dr. K. Yamazaki for their years leading and ocean dynamics discussions. In the end, the author wants to deliver his most profound thanks to Dr. E. Wang and Dr. H.C. Huang for endless supports/care all the road.

This work was found by a Grant-in-Aid for Scientific Research, Ministry of Education, Culture, Sports, Science and Technology, Japan (KAKENHI No. JP16H01585, JP17H01156, JP18H04909), as well as by the Special Grant Program for International Students, Graduate School of Environmental Science, Hokkaido University, Japan, together with the Research Assistant System by Institute of Low-Temperature Science, Hokkaido University, Japan.

Appendix 1: Circular theorem

The vertical averaged the momentum equation as a function of depth z from $z = -H$ to $z = 0$, where $-H$ is a depth of bottom, can be expressed as follows:

$$\frac{\partial}{\partial t}\int_{-H}^{0} \boldsymbol{u}\, dz + \int_{-H}^{0} (f+\zeta)(\boldsymbol{k}\times\boldsymbol{u})\, dz = -\int_{-H}^{0} \nabla\left(\frac{p}{\rho_0}+\frac{|\boldsymbol{u}|^2}{2}\right) dz + \frac{\boldsymbol{\tau_s}}{\rho_0} - \frac{\boldsymbol{\tau_b}}{\rho_0} + \int_{-H}^{0} \boldsymbol{\mathcal{F}} dz, \tag{A1.1}$$

where $\boldsymbol{u}$ denotes a horizontal velocity vector, ∇ is the horizontal gradient operator, f and ζ denote the planetary and relative vorticity, respectively, ρ_0 is a typical density, and p represents pressure. $\boldsymbol{\tau_s}$ and $\boldsymbol{\tau_b}$ denote wind stress and bottom stress, respectively, and $\boldsymbol{\mathcal{F}}$ denotes horizontal viscosity. Afterward, taking a circulation integral along a closed constant-depth contour $H = H_0$, circulation can be expressed as follows:

$$\frac{\partial}{\partial t}\oint\int_{-H_0}^{0} \boldsymbol{u}\cdot\boldsymbol{t}dzdl + \oint\int_{-H_0}^{0} (f+\zeta)\boldsymbol{u}\cdot\boldsymbol{n}dzdl = \oint\frac{\boldsymbol{\tau_s}}{\rho_0}\cdot\boldsymbol{t}dl - \oint\frac{\boldsymbol{\tau_b}}{\rho_0}\cdot\boldsymbol{t}dl + \oint\int_{-\boldsymbol{H_0}}^{\boldsymbol{0}} \boldsymbol{\mathcal{F}}\cdot\boldsymbol{t}dzdl, \tag{A1.2}$$

where l is an along-isobath coordinate, and $\boldsymbol{t}$ and $\boldsymbol{n}$ denote unit vectors along- and cross-isobath coordinates, respectively. Kida and Qiu (2013) derived a streamfunction value on the wall of a single island over a flat bottom by evaluating

$$\oint\int_{-H_0}^{0} \boldsymbol{\mathcal{F}}\cdot\boldsymbol{t}dzdl = 0, \tag{A1.3}$$

assuming a steady-state with spatially constant wind stress $\boldsymbol{\tau_s}$ in a deep ocean where bottom stress $\boldsymbol{\tau_b}$ is negligible. Note that the vorticity flux term (i.e., the second term in the left-hand-side) is identically zero along the island wall in their simple model.

In reality, the vorticity flux term across isobaths (e.g., 1500 m) is not zero, as the MIC is not a single island on a flat bottom but a chain of islands over a submarine ridge. Vorticity flux convergence may therefore occur and drive an anti-cyclonic circulation encompassing the MIC that blocks the interbasin exchange. This may potentially explain the spurious results of the recent high-resolution ocean general circulation models.

Appendix 2: Initial state for COCO model

The COCO model was spun up from the temperature and salinity data of World Ocean Atlas 2009 (WOA09). The original WOA09 data was transferred as curvilinear coordinate grid, fitting the topography.

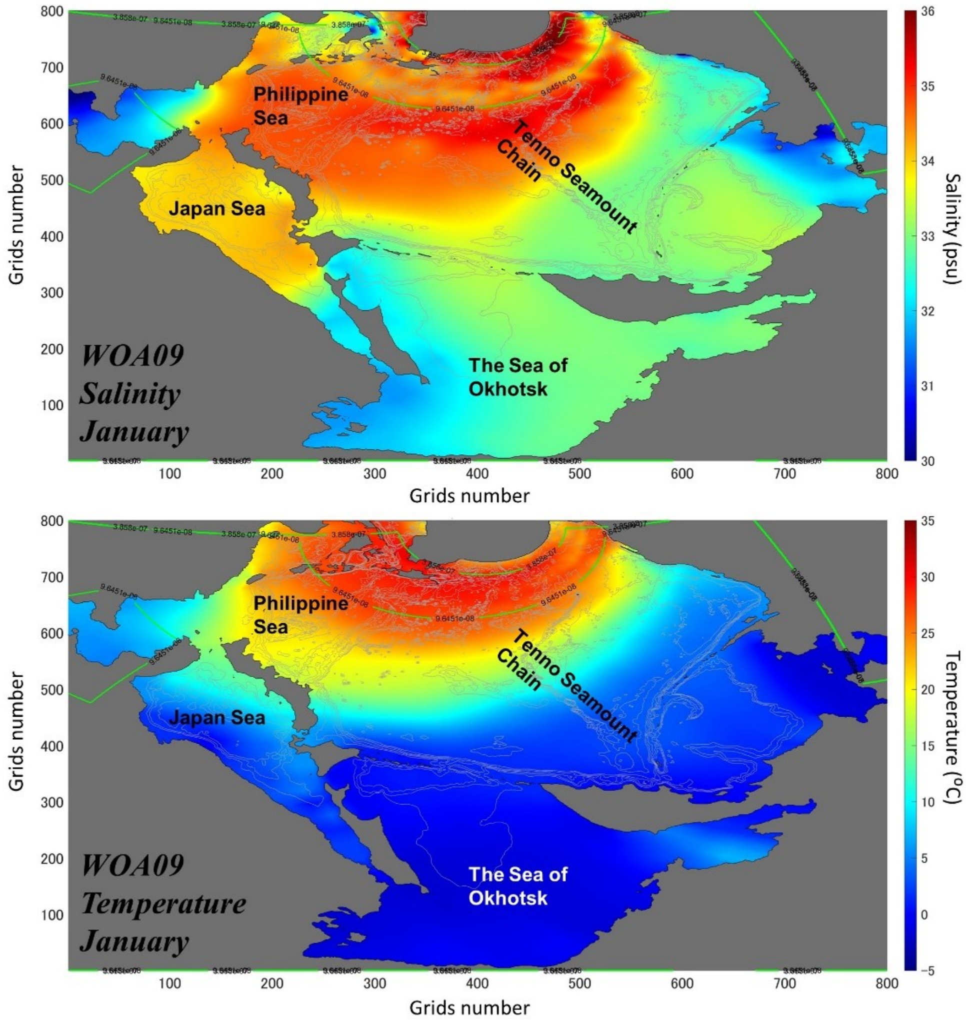

Upper and lower panels are the salinity and temperature of WOA09 January, respectively. The green contours represent the area for restoring during the model integration.

This page intentionally left blank

Appendix 3: Seasonality

The figure below show the streamfunction of the tidal case.

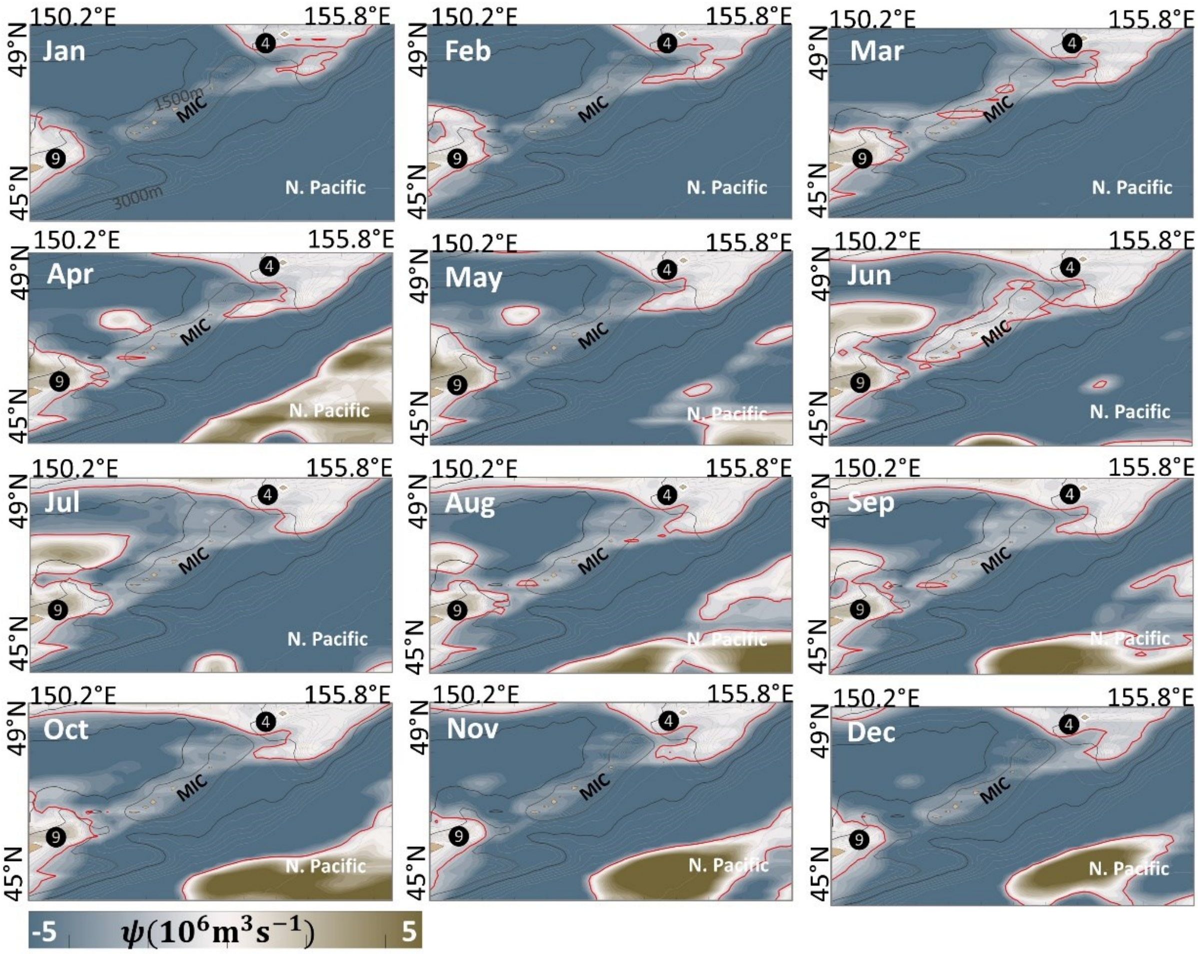

The shade denotes the streamfunction. The red contour denotes the streamfunction contour $\psi = -1.5 \times 10^6$ m^3 s^{-1}. The grey contours denote the topography, where the contour interval is 150 m till 1500 m and continuously with 500 m intervals till 6000 m. The thick grey contours denote the 1500 m and 3000 m depth, respectively. Monthly analyses are ordered from top to bottom and left to right. Although bifurcation points are formed every month, only the envelope of the streamfunction contour $\psi = -1.5 \times 10^6$ m^3 s^{-1} involves most of the MIC in June representing the characteristic flow pattern, as illustrated in Fig. 3.1**b**.

However, the steamfunction of the non-tidal case shown as below has no typical circulation pattern as Fig. 3.1b expected.

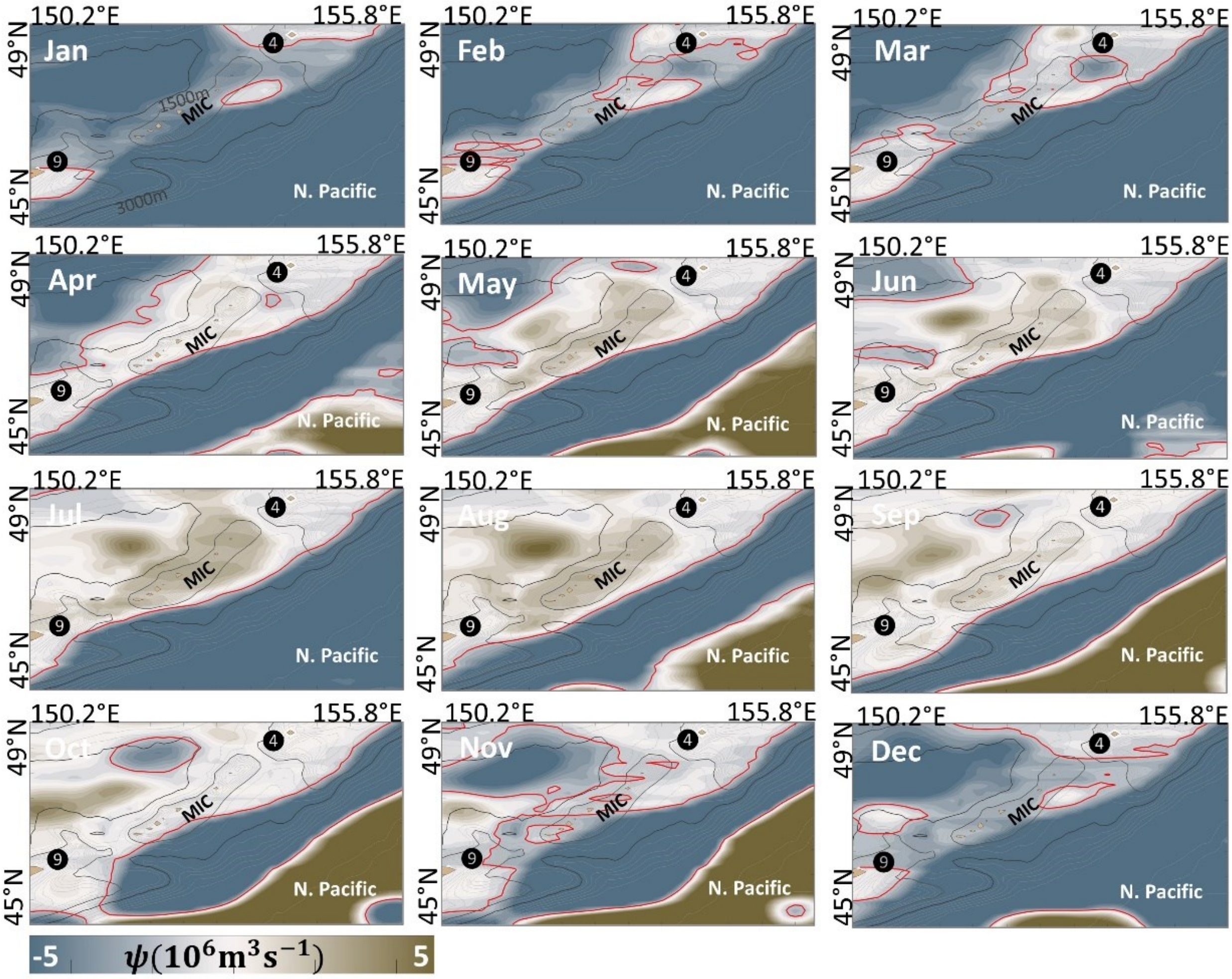

The shading in the illustrations also represents the streamfunction. The red contour denotes the streamfunction contour $\psi = -1.5 \times 10^6$ m^3 s^{-1}. In the non-tidal case, from April to October, the streamfunction contours from the EKC blocks the interbasin exchange. The positive circulations above the MIC during the same period suggest that the cross-MIC vorticity fluxes are enormous as we described in the Appendix 1.

The annual cycle of the tidal (navy-blue line) and the non-tidal (grey line) cases' geostrophic transport are shown in the figure below, where the dashed/solid line denotes the northern/southern strait:

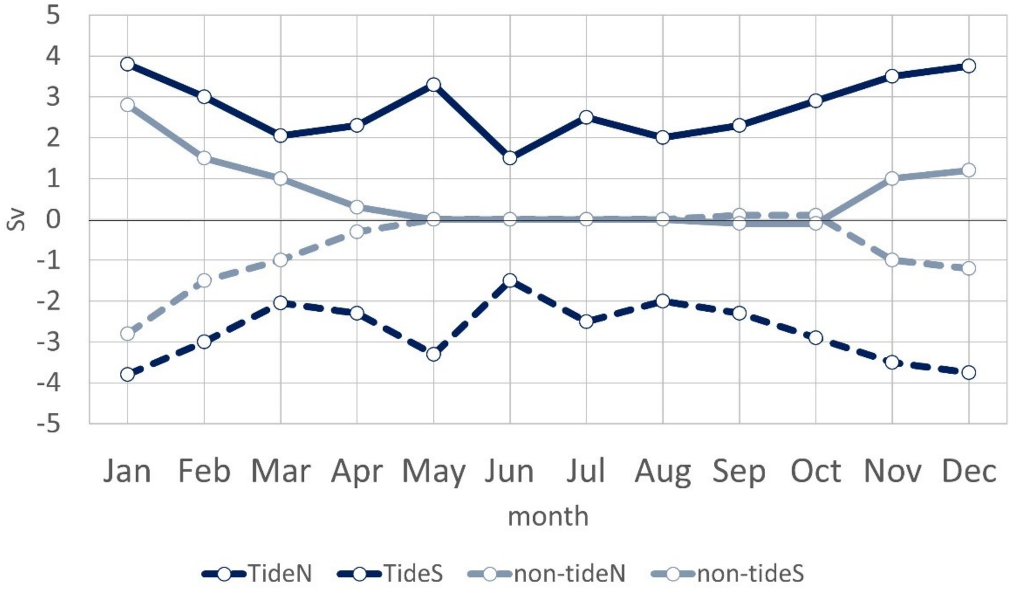

We estimated the geostrophic transport by the streamfunction contours. A net exchange due to the EKC intrusion occurs through the northern and the southern straits if a streamfunction contour ψ_1 crosses these two straits, where ψ_1 is determined by the streamfunction that exhibits a bifurcation point between an EKC's contour and those surrounding the MIC. The transport is estimated by ψ_1, where $\psi = 0$ is given at the coast surrounding the Sea of Okhotsk. In this sense, the geostrophic transport through the northern and the southern straits associated with the intrusion of the EKC is symmetric, as shown in the plot above, and is weak in summer and strong in winter. Note that in the non-tidal case, we depict the transport from May to August to be zero because the EKC's streamfuction does not pass through the northern strait and the interbasin exchange is blocked; no bifurcation point forms for evaluating ψ_1.

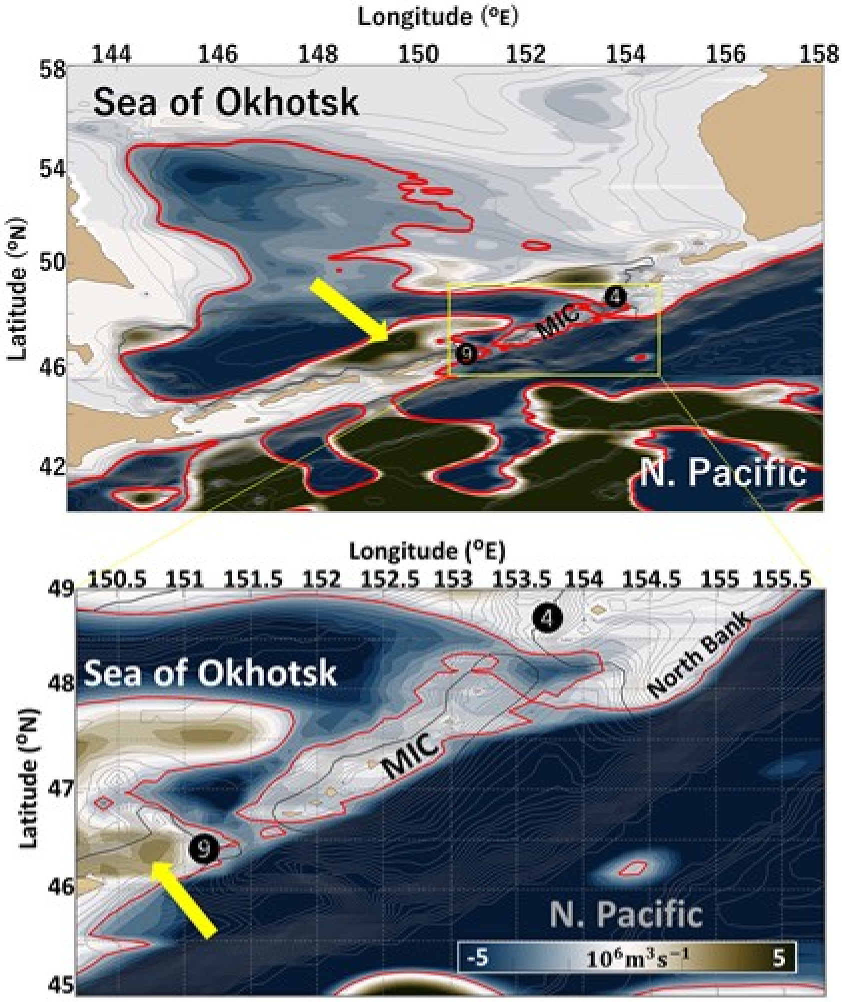

As we described above, the throughflow transport "associated with the EKC intrusion" provides a symmetric volume through two straits. Nevertheless, we believe that it is meaningful to present the transport based on velocity on the cross-strait sections because this estimate is directly comparable to in-situ measurements such as those obtained via lowered acoustic Doppler current profiling, as described by Katsumata *et al*. (2004). As indicated by the yellow arrow, there is further local re-circulation to the south of the southern strait. The cross-section estimates include a part of this southern recirculation. Since the local recirculation is superimposed on the geostrophic transport, the cross-strait transport through the southern strait does not necessarily show a seasonal variation similar to that through the northern strait.

Appendix 4: Potential Vorticity Equation derivation

By cross differentiating depth-averaged momentum equation, we can have vorticity equation that

$$\frac{\partial[\zeta]}{\partial \mathrm{t}}+[u]\frac{\partial[\zeta]}{\partial x}+[v]\frac{\partial[\zeta]}{\partial y}+(f+[\zeta])\left(\frac{\partial[u]}{\partial x}+\frac{\partial[v]}{\partial y}\right)+\beta[v]=\nabla\times([\boldsymbol{F}]), \tag{A4.1}$$

where β is the β effect in β plane and the bracket $[\blacksquare]$ denotes the depth averaged term that $[\blacksquare]=\frac{1}{H}\int_{H}^{0}\blacksquare\, dz$. Since the term $\beta[v]$ is equal to $[v]\frac{\partial \mathrm{f}}{\partial \mathrm{y}}$, equation (A4.1) refers to

$$\frac{d([\zeta]+f)}{dt}+(f+[\zeta])\left(\frac{\partial[u]}{\partial x}+\frac{\partial[v]}{\partial y}\right)=\nabla\times([\boldsymbol{F}]). \tag{A4.2}$$

Substituting the continuity equation that

$$(h+\eta)\left(\frac{\partial[u]}{\partial x}+\frac{\partial[v]}{\partial y}\right)+\frac{d(h+\eta)}{dt}=0, \tag{A4.3}$$

where h is bottom depth and η is sea surface height, into Equation (A4.2), it becomes

$$\frac{\mathrm{d}([\zeta]+\mathrm{f})}{\mathrm{dt}}-\frac{(f+[\zeta])}{(h+\eta)}\frac{d([\zeta]+f)}{dt}=\nabla\times([\boldsymbol{F}]). \tag{A4.4}$$

Reorganizing equation (A4.4) that

$$(h+\eta)\frac{d([\zeta]+f)}{dt}-(f+[\zeta])\frac{d([\zeta]+f)}{dt}=\big(\nabla\times([\boldsymbol{F}])\big)(h+\eta). \tag{A4.5}$$

Since $\frac{\mathrm{d}\frac{\mathrm{A}}{\mathrm{B}}}{\mathrm{dt}}=\frac{\frac{\mathrm{dA}}{\mathrm{dt}}\mathrm{B}-\frac{\mathrm{dB}}{\mathrm{dt}}\mathrm{A}}{\mathrm{B}^2}$, dividing equation (A4.5) by $(h+\eta)^2$, we then get

$$\frac{d\frac{([\zeta]+f)}{(h+\eta)}}{dt}=\frac{(\nabla\times([\boldsymbol{F}]))}{(h+\eta)}, \tag{A4.6}$$

which is the potential vorticity equation that $\frac{d[q]}{dt}=\frac{\nabla\times[\boldsymbol{F}]}{H}$, where $H=h+\eta$.

Further, since the forcing terms $\boldsymbol{F}$ at the right-hand side of equation (A4.6) are,

$$\mathbf{F} = -\frac{1}{\rho_0}\nabla P + \frac{1}{\rho_0}\frac{\partial \boldsymbol{\tau}}{\partial z}, \tag{A4.7}$$

where $P = \int_{-H}^{0} \rho g h \, dz$, the potential vorticity equation is

$$\frac{\partial [q]}{\partial t} + [\boldsymbol{u}] \cdot \nabla [q] \tag{A4.8}$$

$$= -\frac{\nabla \times \left(\frac{g}{\rho_0 H}\int_{-H}^{0} \nabla \rho z \, dz\right)}{H} + \frac{\nabla \times \frac{[\boldsymbol{\tau}]}{\rho_0 H}}{H}$$

$$-\frac{\nabla \times ([(Cd|\boldsymbol{u}|\boldsymbol{u})]/\rho_0 H)}{H}.$$

Supplementary Movie 1: Propagation of the tidal topography trapped wave.

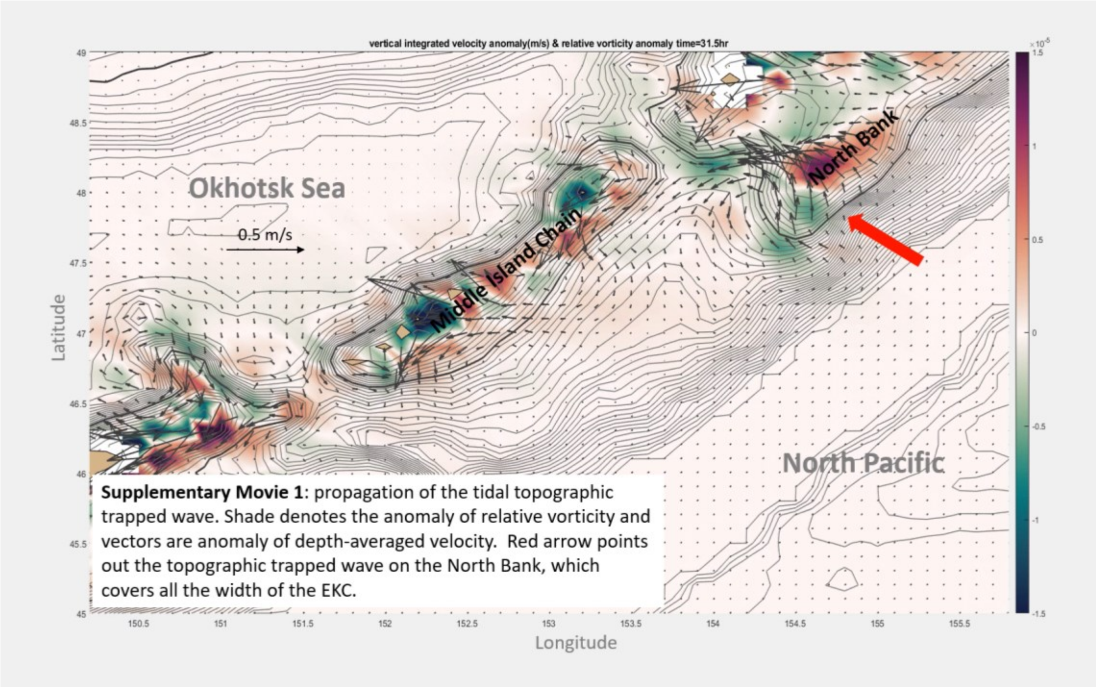

Shade denotes the anomaly of elative vorticity and vectors are anomaly of depth-averaged velocity. Red arrow points out the topography trapped wave on the North Bank, which covers all the width of the EKC.

Please access the video by one of the links below:

QR code

Direct link

https://youtu.be/1iF8TFRG4pY

This page intentionally left blank

Supplementary Movie 2: The transition experiment from non-tidal to tidal state.

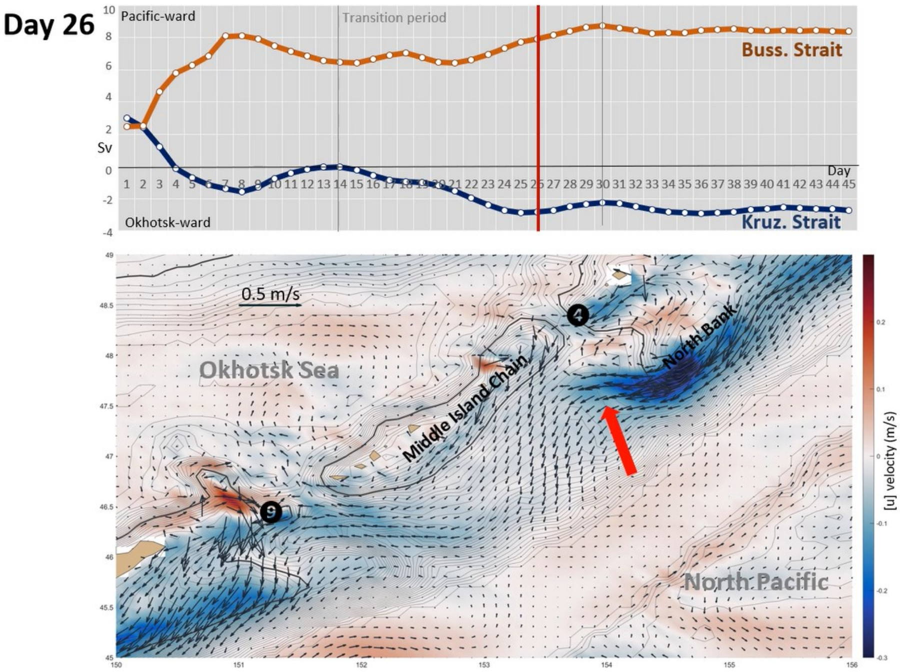

Supplementary Movie 2. The Transition Experiment. Upper panel is the transport through two straits, and the lower panel is the plane view of the depth-averaged velocity. The red arrow denotes the shifting of the pathway of the EKC.

Upper panel is the transport through two straits, and the lower panel is the plane view of the depth-averaged velocity. The red arrow denotes the shifting of the pathway of the EKC.

Please access the video by one of the links below:

QR code

Direct link

https://youtu.be/P5LrPHysJsQ